UNIVERSITY OF CALIFORNIA, SAN DIEGO

Exploratory nose movement: behavioral dynamics and functional brainstem circuits.

A dissertation submitted in partial satisfaction of the
requirements for the degree
Doctor of Philosophy

in

Neurosciences with a Specialization in Computational Neurosciences

by

Anastasia I. Kurnikova

Committee in charge:

Professor David Kleinfeld, Chair
Professor Martyn Goulding
Professor Harvey Karten
Professor Byungkook Lim
Professor Eran Mukamel
Professor Lisa Stowers

2018

The dissertation of Anastasia I. Kurnikova is approved, and it is acceptable in quality and form for publication on microfilm and electronically:

_____

_____

_____

_____

_____

_____

Chair

University of California San Diego

2018

TABLE OF CONTENTS

LIST OF FIGURES

LIST OF TABLES

ACKNOWLEDGEMENTS

I would like to thank my advisor, David Kleinfeld, for supporting me through pursuing this and other projects and for allowing me the time and resources to try, fail, and succeed on my own. Thank you for encouraging me to see the bigger picture in research proposals, and your unwavering commitment to high quality research.

Thanks to Martin Deschênes - my second advisor albeit unofficially - Thank you for teaching me to go through experiment ideas quickly, for showing me what true enthusiasm for science looks like, and for setting me on the path to my final project.

A special thanks to Jeff Moore and Celine Mateo, who trained me when I first got to the lab, as well as the rest of the Kleinfeld lab for your support and readiness to help hroughout my time there. I would also like to acknowledge my classmates neuroscience program: I am honoured to have been a part of such a passionate group of people.

Finally, I'd like to thank my lovely family: Michael, Maria, Judy, and Igor. I couldn't have done it without your love and support, and your immense amount of help this past year.

Chapter 2 includes work that is currently published in: M. Deschênes, J. Takatoh, A. Kurnikova, J.D. Moore, M. Demers, M Elbaz, T. Furuta, F. Wang, D. Kleinfeld, Inhibition, not excitation, drives rhythmic whisking", *Neuron*, 2016. and J. D. Moore, M. Deschênes, A. Kurnikova, D. Kleinfeld. "Activation and measurement of free whisking in the lightly anesthetized rodent", *Nature Protocols*, 2014. Figures included in the dissertation were contributed by the dissertation author. This material is included in Chapter 2 with the generous consent of all coauthors.

Chapter 3, in full, is a reprint of material that is currently published in: A. Kurnikova*, J. D. Moore*, S.-M. Liao, M. Deschênes, D. Kleinfeld., "Coordination of orofacial motor actions into exploratory behavior by rat", *Current Biology*, 2017. The dissertation author was the primary investigator and author of this manuscript. This material is included in Chapter 3 with the generous consent of all coauthors.

The material of Chapter 4 is a manuscript that is currently under preparation for submission: A. Kurnikova, M. Deschênes and D. Kleinfeld, Functional brainstem circuits for control of nose motion. The dissertation author was the primary investigator and author of this material.

Chapter 5 in part contains work published in: M. Deschênes, A. Kurnikova, M. Elbaz and D. Kleinfeld. "Circuits in the ventral medulla that phase lock motoneurons for coordinated sniffing and whisking", *Neural Plasticity*, 2016. This material is included with the generous consent of all coauthors.

VITA

2010	B. S. in Physics *University Honors*, Carnegie Mellon University
2018	Ph. D. in Neurosciences with a Specialization Computational Neurosciences, University of California San Diego

PUBLICATIONS

A. Kurnikova*, J. D. Moore*, S.-M. Liao, M. Deschênes, D. Kleinfeld., "Coordination of orofacial motor actions into exploratory behavior by rat", *Current Biology*, 2017.

M. Deschênes, A. Kurnikova, M. Elbaz and D. Kleinfeld. "Circuits in the ventral medulla that phase lock motoneurons for coordinated sniffing and whisking", *Neural Plasticity*, 2016

M. Deschênes, J. Takatoh, A. Kurnikova, J.D. Moore, M. Demers, M Elbaz, T. Furuta, F. Wang, D. Kleinfeld, Inhibition, not excitation, drives rhythmic whisking", *Neuron*, 2016.

D.B.T. McMahon, B.E. Russ, H. Elanaiem, A. Kurnikova, D.A. Leopold. "Face patch neurons signal spatial content in natural scenes", *J. Neuroscience*, 2015

J. D. Moore, M. Deschênes, A. Kurnikova, D. Kleinfeld. "Activation and measurement of free whisking in the lightly anesthetized rodent", *Nature Protocols*, 2014.

M. Castronovo, A. Lucesoli, P. Parisse, A. Kurnikova, A. Malhotra, M. Grassi, G. Grassi, B. Scaggiante, L. Casalis, G. Scoles. "Two-Dimensional Enzyme Diffusion in Laterally Confined DNA Monolayers" *Nature Communications*, 2011.

ABSTRACT OF THE DISSERTATION

Exploratory nose movement: behavioral dynamics and functional brainstem circuits.

by

Anastasia I. Kurnikova

Doctor of Philosophy in Neurosciences with a Specialization in Computational Neurosciences

University of California San Diego, 2018

Professor David Kleinfeld, Chair

Exploration and navigation involves movement of the body and of sensory organs. Positioning of the eyes, ears, whiskers, nose, head and body determine which sensory inputs are collected and attended to. The neural circuitry that controls sensory organ positioning has been studied to reveal the mechanisms by which movement is initiated and gated. Further examples of circuits and quantifications of these behaviors will help to determine general principles of control of movement of sensory organs.

In this manuscript I examine movement of the nose, a little-described behavior which is prominent in many rodents. I quantify behavioral features of nose movement, and identify a basic circuit in the brainstem that controls it through a combination of anatomical tracing and

functional study. Specifically, I find that nose movement occurs when rodents sniff, is coordinated to breathing, and responds to odor presentation. I identify two putative premotor areas that may control motion of the nose, and show that one of the areas gates nose response to odor presentation. The structure of the nose motion circuit can be compared to circuitry to that of other known orofacial motor actions, such as control of whisker movement and licking. Future work in this system system can help to elucidate common features of orofacial motor control.

Chapter 1

Introduction

Animals and humans interact with the world by collecting sensory information and responding to it appropriately. Gathering information can comprise of passively accepting incoming sensory stimuli. However, most often exploration involves movement of the body and of sensory organs. For example the eyes and head might move to examine a salient part of the visual space. In some animals, the ears orient towards auditory stimuli, or the whiskers move to touch a nearby object. Limbs, eyes, ears, whiskers, head and nose can move to scan the surrounding space without moving the body. Such movements serve to expand the range of space that is sampled, as well as to improve the perception of given parts of a scene. Perceiving the environment using dynamically moving sensory organs is known as active sensing.

In addition to such 'orienting' movements that are used for perceptual selection, some sensory exploration involves 'rhythmic' movements. Whisking in rodents is a prime example of rhythmic movement for active sensation. In order to probe regions of interest, rodents actively sweep their vibrissae in a large back and forth rhythmic motion known as whisking [4, 6, 5]. This repetitive movement is essential to tasks such as discriminating textures [9]. Rhythmic movement is thought to enhance perception even in cases where it is not strictly necessary for sensory identification [76, 84].

In this manuscript, I will present a novel exploratory behavior - motion of the nose in rodents - and describe features of the behavior and its underlying circuit. I show that behaviorally, nose motion has both orienting and rhythmic movement, and responds to inputs from the olfactory system. Further I show that circuits for nose motion control are structured in a similar way other whisker motor control, thus demonstrating a more general aspect of orofacial motor control in rodents.

Movement of the nose is a particularly attractive behavior to study in relation to the breathing cycle, as olfactory processing is particularly affected by its synchronization to breathing []. Further, due to the sensitive nature of olfaction, even small changes in air flow through the nasal passages may affect olfactory processing.

1.1 Olfactory cue localization

Rodents are able to localize olfactory cues in space by comparing inputs between nostrils. In a study by Rajan et al. rats were able to distinguish small differences in laterality of olfactory inputs [81]. Rats were presented with odors on two sides of the snout with a small time delay, and asked to choose the side on which the odor appeared first for a reward. They were able to respond to timing differences of as little as 50 ms. In a follow up study, Parthasarathy et al, showed that they are also able do distinguish odor gradients when presented on two sides of the snout. These results suggest that rats are highly attuned to very small changes in air flow between nostrils.

Do rodents use this inter-nostril comparison to perform olfactory localization tasks? Two studies show that rodents are impaired on olfactory localization tasks when a nostril is blocked, indicating that ccomparison between nostril inputs is behaviorally relevant.

Khan et al showed that rats are also able to track an odor trail, and are impaired on the task when a nostril is blocked [57]. Figure 1.1 shows the results of this study. Rats were trained to run across a conveyor belt to which a meandering odor trail was applied. The rats made full body

and head movements in order to follow the trail with their nose. When a nostril was stitched shut, compared to a control sham nostril stitching, the rats were impaired in their abillity to smoothly pursue the trail. This was measured as increased deviation from the trail, for both a phenethyl alcohol (PEA) and a chocolate odor trail. These results suggest that rats use "stereo" sampling by comparing between nostrils to perform a task.

A similar conclusion was reached by Catania et al., who studied olfactory localization in blind moles that were tasked to find a food source in a semi-circular arena. They found that the moles were able to run straight to the food source under normal conditions. When nostrils were intubated and crossed, or when one nostril was blocked, the moles made errors in identifying the food source once at a proximal range [16]. Thus, this study also found impairment olfactory food localization that is likely attributed to a deficit in comparison between nostrils.

The most extensive work related to odor trail tracking comes from the insect world. Honeybees orient their antennae to an odor source [95], and such movment of the antennae has been found to be important for trail tracking [69]. Thus, when a single antenna is fixe in place, and the other is removed, bees have a much more variable path in pursuing an olfactory trail. Bees also are impaired at trail tracking if the antennae are fixed close together in a way that does not allow inter-nostril comparisons [69]. Other animals also use bilateral nostril comparisons to do trail tracking. These include ants [93, 54], flies [25, 38, 37], larvae [67], and even humans [78]. Bilateral comparisons have also been adopted as a strategy for robot navigation [49].

The results of these studies suggest that air flow differences between nostrils is important for odor tracking and localization in rodents. While no experiments have identified the role of movement of the nose per se, the studies of insect trail tracking suggest that nose movement may aid in achieving a smoother trail tracking performace.

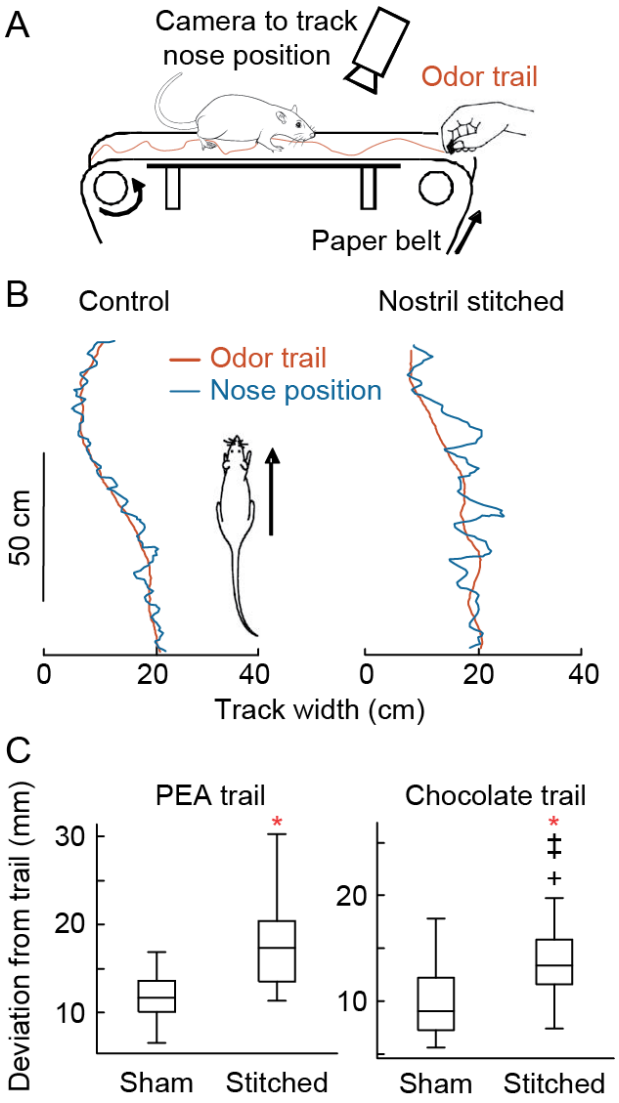

Figure 1.1: Rodents impaired on odor trail task when one nostril is blocked - Adapted from Khan et al 2012. (A) A schematic of the apparatus. A rat runs across a paper to which an odor trail is applied. The nose position is monitored with a camera. (B) An example of a stretch of tracking. The ratâĂŹs nose trajectory (blue) is overlaid on the trail (red) Right is sham control, and left is the tracking with a nostril stitched. (C) Rats show increased deviation from both a phenethyl alcohol (PEA) and a chocolate trail when a nostril is stitched

1.1.1 Responses in AON

Kikuta et al (2010) found that cells in the acccessory olfactory nucleus (pars extcomplex-erna) report differences in air flow between nostrils. Specifically, when anaesthesized rats were presented with an odorant to the ipsilateral nostril, the AONpE cells fired strongly [58]. When the same odorant was presented also to the contralateral nostril, the response diminished with the proportion of odorant presented to the ipsi- vs contralateral nostril. This demonstrates that there are circuits in the rodent brain which serve to compare inputs between nostrils. A similar comparison area exists in the honeybee olfactory areas [95]. Finding the connections between this area, and the neural circuits that guide odor tracking behavior would reveal a fascinating aspect of rodent locomotion.

1.2 Orofacial musculature

1.2.1 The whisking motor plant

The vibrissae are controlled by a set of several muscles - the intrinsic muscles, and the extrinsic muscles - *nasalis*, *maxillolabialis*, *nasolabialis* and *transversus nasi*. The intrinsic muscles are a set of small muscles that wrap in a sling around each follicle. These muscles pull individual vibrissae to move them forward. In contrast, the extrinsic muscles pull the whole pad. *nasalis* moves the pad rostrally, *maxillolabialis* moves the pad caudal and ventral, *nasolabialis* moves the pad caudal and dorsal, while *transversus nasi* pulls the pad upward. Thus, the motor control of the vibrissae has multiple components that may have separate circuits controlling them

1.2.2 The *deflector nasi* muscle

Lateral nose movement is a controlled by the *deflector nasi* muscle [43, 20, 44]. The *deflector nasi* was initially misidentified as a muscle that controls dilation of the naris, and

originally referred to as the *dilator nasi*.

Deschênes et al examined the rat snout musculature in higher detail and found that the muscle is better positioned to deflect the nose rather than to affect the nares. When it is stimulated, the *deflector nasi* pulls the nose laterally and upwards to the deflected side, and does not directly affect the dilation of the nostril. Further, EMG recordings from the *deflector nasi* correlate with nose deflections in an awake, head restrained rat. Instead, naris dilation is controlled by the maxillary division of muscle *nasolabialis profundus*.

Figure 1.2 shows the *deflector nasi* identified in slices through the snout of a 2-week old rat. The muscle has a single attachment point rostrally, and two attachment points on the caudal end.

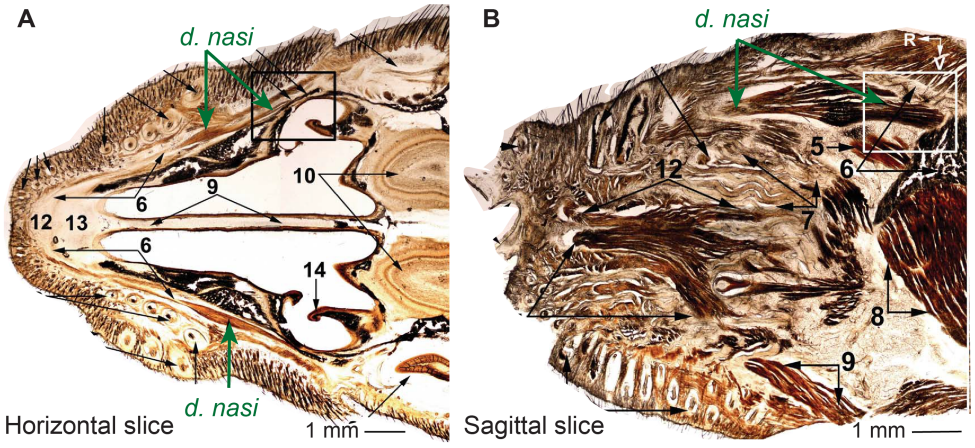

Figure 1.2: The *deflector nasi* muscle. Adapted from Deschênes et al 2014. Slices through the snout of a 2 week old rat, stained with CO. (A) shows a horizontal with the *deflector nasi* muscle highlighted by green arrows on each side of the snout. (B) Shows a sagittal slice, with the muscle higlighted by a green arrow

1.3 Orofacial motor circuit structure

1.3.1 Motor nuclei for facial muscles

Facial motor actions are driven by motoneurons located in the facial motor nucleus. These inputs synapse onto muscles in the face such as the vibrissa motor plant [48], eye blink muscles, or the deflector nasi. The facial nucleus shows a topography of distribution of motoneurons [104, 63, 52, 59, 30, 32, 41]. Thus the ventro-lateral facial nucleus sends inputs to the vibrissa intrinsic muscles, while the dorsolateral portion sends inputs to muscles nasolabialis and deflector nasi. The medial part of the facial nucleus controls eyeblink and ear movement.

1.3.2 Premotor inputs

Past the facial nucleus, inputs throught the brainstem synapse directly onto facial motor neurons. We call these inputs 'pre-motor areas' as they are positioned directly prior to the motoneurons. Input to the facial nucleus originates in the medulla, midbrain, and even some sparse projections from the motor cortex [46, 53, 92, 97, 11]. Some of these pre-motor areas recieve inputs from higher order motor areas (Pre^{2}motor inputs), while some also recieve sensory input. These sensory and motor areas form the first sensorimotor loops, and can drive responses to certain simple stimuli. Other motor inputs are thought to be the basis for more complex motor responses and volitional control [1, 2].

In the case of whisking, a group of cells in the medulla has been shown to generate the whisking rhythmic pattern [74]. This central pattern generator (CPG) can be activated pharmacologically in anaesthesized animals to generate a whisking behavior [74]. Further, ablating the area eliminates the oscillatory component of whisker motion while retaining a change in 'set-point' that is coordinated with the other side [61]. This result suggests that other inputs to the facial motor nucleus are able to modulate slow positioning of the whisker. Furthermore, it implies that rhythmic and orienting movement are under separate control in the brain.

1.3.3 Pre^{2}motor inputs

Control of orofacial movement involves the interaction of multiple descending pathways, and feedback loops through the sensory system. Pathways that originate in the motor cortex are thought to generate volitional movement, and have been studied extensively to understand the nature of this control. It has been hypothesized that the vibrissa region of motor cortex (vM1) controls aspects of movement that vary over longer time scales rather than generating the precise sequence of motor commands involved in whisking. The sensorimotor cortex (S1) also elicit vibrissa movement [3, 91]. Electrophysiological recordings suggest that vM1 reports the slowly varying amplitude and setpoint of whisking [51, 36, 31]. However, functional manipulations demonstrating such a role have not been established. While it has been shown that microstimulation of vM1 elicits single whisker movements or short bouts of rhythmic whisking [45, 70, 10, 4] these studies have been unable to demonstrate a specific role for this area in whisking behavior. In fact, the motor cortex is not necessary for generating vibrissa movement, as rhythmic whisking can be observed after surgical removal of cortex and or cerebellum[85, 34].

Thus, it is critical to view orofacial motor control generation as a function of a multitude of descending motor commands through multiple pre-motor pathways. Ablation of a given pathway may not necessarily disrupt all observed movement. Further, it is critical to understand how pre-motor areas function in order to parse out the contribution of higher order inputs to their modulation.

Pre^{2}motor inputs may also be responsible for coordination of movement from various sensory modalities. Movements across modalities are also thought to be timed to provide temporal coordination of sensory inputs [13]. For example saccadic eye movements, pinna movements, head movements are temporally coordinated with each other in cats [77, 7]. Thus, in response to an auditory stimulus, the cat orients her ears and also her head and eyes to the percieved location. This might enable her to most efficiently gather sensory information about the source. Similarly, lateral movements of the head are coordinated with the assymetry in the positioning of vibrissae

(whiskers) [101]. Head movements likely serve to orient the nose as well [57] Thus, studying the circuits underlying movement of the nose can bridge to an understanding of how other sensory motor actions relate and coordinate with nose movement.

1.3.4 Rhythmic movement coordination with breathing

Synchronization of orofacial movement with sniffing is hypothesized to be a means to unify movement and bind related sensory inputs [61]. Rodents sniff in response to novel odors, reward expectation, and during social interactions [106, 9, 103, 108]. A relation between breathing and movement has been observed for whisking, vertical head bobbing, nose movement [106], and vocalizations [87] but only select cases have been validated with quantitative data [74, 87, 82].

The PreBötzinger complex is the inspiratory breathing center in the brainstem [19]. It sends projections throughout the brainstem [99, 29], leading to the hypothesis that its projections coordinate facial motor actions [61]. The PreBötzinger complex can be identified by several genetic markers, such as Somatostatin [98, 94], and Neurokinin-1 [42, 39], silencing which inhibits breathing.

Whisking has been shown to coordinate to breathing via brainstem circuit in which the PreBötzinger complex provides the inspiratory drive that triggers the onset of a whisk [74]. Thus, the PreBötzinger complex is a pre^{2}motor input to the whisking musculature. Other orofacial behaviors are also hypothesized to involve brainstem circuits to relate the movement to breathing [60]. Such brainstem circuits of orofacial sensory organs are of particular interest in that they may coordinate with breathing and also be modulated by additional inputs, such as sensory cues or arousal state. Studying these interesting effects requires first understanding in detail the conditions under which the behaviors activate and coordinate to the breathing cycle.

1.4 Nose movement

In this manuscript, I test the hypothesis that circuits for nose motion are structures in a similar way to whisking control. Thus, input from the PreBötzinger complex may provide input to one or more premotor area in the medulla, which then drive motion of the nose under different conditions. I identify these putative premotor areas, and show that they are responsible for movement of the nose. I also identify other putative premotor and pre2motor areas that may be involved in driving movement of the nose under different conditions.

Chapter 2 presents new data relating to the function of the whisking oscillator. We extend past work in rats to mice, and additionally demonstrate that motoneurons in the facial motor nucleus activate during rhythmic vibrissa protraction. We also provide evidence that the vibrissa oscillators are not connected bilaterally.

Chapter 3 describes the behavioral aspects of nose motion and synchronization to other orofacial motor actions.

Chapter 4 presents data on the nose motion circuit and two newly identified premotor areas.

Chapter 2

The whisking CPG

2.1 Introduction

Rhythmic whisking has been shown to be controlled by a CPG in the brainstem in rats, and can be activated by an injection of the kainaite agonist Kainic acid in the vicinity of the oscillator[74]. While rats and mice are typically found to have similar neuraul circuits, there is no guarantee that they behave identically. Thus, we aimed to confirm that this CPG can also be activated in a similar manner in mice. In further work we aimed to study the properties of the ativity of the CPG in further detail.

2.2 Activation of the whisking CPG in mice

In the rodent vibrissa system, rhythmic stimulation of the facial motor nerve at the whisking frequency has been used to determine the neuronal encoding of tactile stimuli that rodents are likely to encounter during natural whisking [111, 12, 96]. However, unlike pharmacologically induced fictive movement preparations, electrically induced whisking requires the experimenter to generate the vibrissa kinematics and rhythm arbitrarily on the basis of the stimulation parameters.

Facial nerve stimulation typically recruits all of the vibrissa muscles together, with the largest motor fibers recruited first rather than last-the opposite of what would be expected according to Henneman's size principle [47]and it further produces high accelerations that are atypical of natural whisking. Although the recent use of use of optogenetic activation may relieve the difficulty with recruitment in the sense that small fibers are recruited first [66], it still requires the experimenter to directly control kinematics.

Recent work in has provided a method by which whisking may be induced pharmacologically in rats [74] Here we describe transfer this protocol for pharmacological induction of sustained rhythmic vibrissa movements in an in vivo anesthetized preparation in mice. Local injection of a glutamatergic agonist, kainic acid, is used to activate pre-motor neuronal networks to mimic natural whisking [74]. This approach is similar to well-established methods that use pharamocological activation to elicit real or fictive rhythmic movements [40]. In this procedure, sustained rhythmic contractions of the intrinsic vibrissa muscles are induced by focal injection of kainic acid into the medulla.

The protocol described here involves stereotaxic iontophoric injection of kainic acid in the intermediate reticular formation of the medulla After the injection, the animal is implanted with a stainless steel plate for head restraint and the vibrissa motion is monitored in real time Figure 2.1. The induction of rhythmic vibrissa movements by kainic acid injection typically lasts for 0.5-1 h in mice. Therefore, a variety of scientific questions can be addressed by combining the protocol with various possible experiments.

Mouse surgery

(i) Administer ketamine/xylazine anesthesia via i.p. injection. Inject a cocktail that contains 100 mg/kg ketamine (reagent-to-animal weight) and 10 mg/kg xylazine. Wait 5-10 min for the anesthesia to take effect, and then check the withdrawal reflex by pinching the toe of the animal. Proceed once the reflex is lost.

(ii) Shave the fur on top of the cranium. Disinfect the exposed skin with Betadine. Then place the

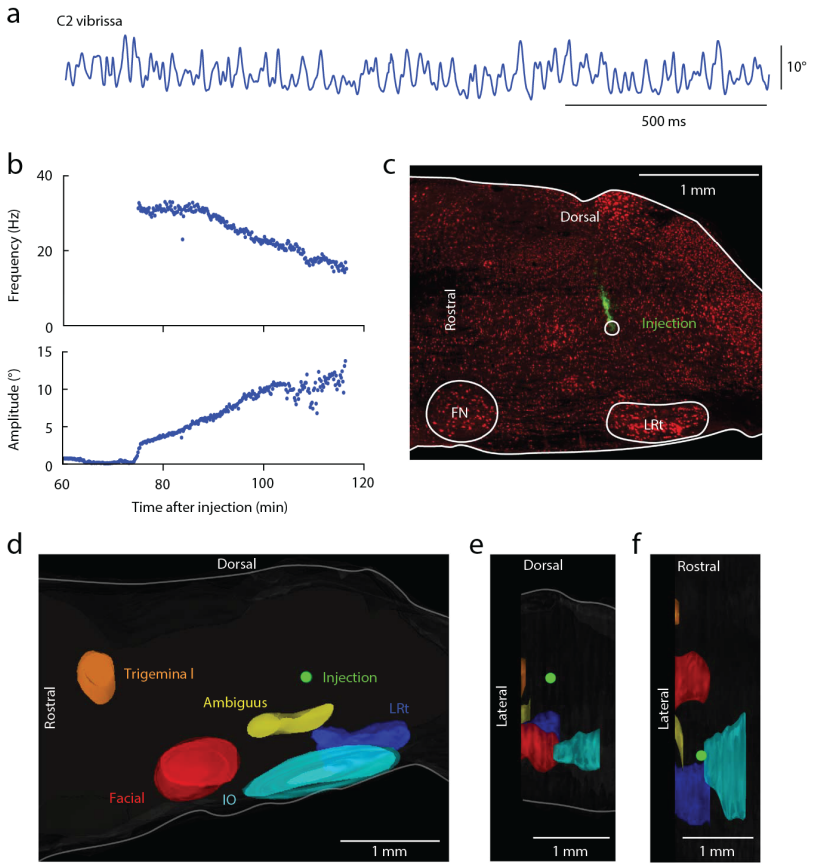

Figure 2.1: Kainic acid injection produces rhythmic vibrissa movements in mouse.(a) Vibrissa position (blue) following kainic acid injection. Similar results for vibrissa position were obtained in a total of 7 out of 12 mice (58%). All mice were C57BL/6 females, 20-30 g, purchased from Jackson Laboratories. (b) Time course of vibrissa movement frequency (top, blue) and amplitude (bottom, blue) after kainic acid injection. The frequency is defined as (1/2 π) x $d\Phi(t)/dt$ averaged over 30-s intervals, where $\Phi(t)$ represents the instantaneous phase from the Hilbert transform of the vibrissa angle in time. The amplitude is defined as 2 x A(t) averaged over the same interval, where A(t) represents the amplitude from the Hilbert transform. The breathing frequency (top, red) is similarly defined. Frequency was defined only for movements that had an amplitude of >5deg/s. (c) Sagittal section containing the injection site, prepared as in Figure 3e. NeuN histology was performed on a total of five mice after labeling the injection site with BDA. Labeling was successful in five of the five attempts, and all five cases showed similar NeuN staining around the labeled site. (d-f) 3D reconstruction of the injection site in c relative to anatomical landmarks. Injection site is shown relative to anatomical landmarks: trigeminal (orange), facial (red) and ambiguus (yellow) motor nuclei, the inferior olive (IO, light blue), and the lateral reticular nucleus (LRt, dark blue). Frontal (e) and horizontal (f) views of the reconstruction in d. Reconstructions were performed by scanning all sections on a Nanozoomer Slide Scanner (Hamamatsu) and tracing the anatomical boundaries using Neurolucida software (Microbrightfield). All animal procedures were approved by the IACUC at UC San Diego

animal in a stereotaxic holding frame, attach the servo-controlled heating blanket and turn it on to 37 degrees.

(iii) Use a scalpel to make an incision in the skin above the cranium, approximately along the midline. Scrape away the periosteum with a spatula.

(iv) Estimate the approximate stereotaxic coordinates of the injection site with a ruler and mark the site and the location of bregma with a permanent pen. For 25 g mice, the coordinates are 6.5 mm caudal and 0.9 mm lateral to the bregma suture.

(v) Score the cranium in a cross-hatch pattern with a scalpel. Leave space around the area where the craniotomy will be performed for the kainic acid injection (performed in Step 1B(vi)). Glue the sutures with cyanoacrylate to provide stability during drilling. Any additional surgery and positioning of the head restraint required for the desired experiment can be performed at this point, before kainic acid injection, to maximize recording time after kainic acid injection.

(vi) By using the micromanipulator, lower the head-restraint piece to its proper location on the cranium. Coat the scored areas of the cranium and glue the head-restraint piece with cyanoacrylate. Wait at least 20 min for the cyanoacrylate to dry completely.

(vii) Use a dental or electric drill to perform a craniotomy, a 2âĂŞ3-mm square that is centered at the coordinates in Step 1B

(iv). Carefully remove the dura mater by using fine forceps. Bathe the open cranium with ACSF.

(viii) Place the pipette filled with the kainic acid solution in the jig that attaches the pipette to the micromanipulator. To label the recording site (optional), the pipette should contain a mixture of kainic acid and BDA. Connect the pipette to the current source via the silver wire. Place the reference/return electrode so that it touches the cranial surface. Use the micromanipulator to move the pipette to the coordinates listed in Step 1B(iv). Lower the pipette until it touches the pial surface. Then slowly lower the pipette into the brain to the appropriate depth of 4.5 mm.

(ix) Use the current source to pass negative current pulses. Pulses should have an amplitude of -350 nA and be 1 s in duration at a repetition period of 2 s for 5 min. If the recording site is being

labeled, pass additional pulses of +300 nA for 10 min to electrophorese the BDA. In all cases, monitor the applied current or voltage at the current source.

2.3 Recordings from facial motoneurons in alert head-restrained rats

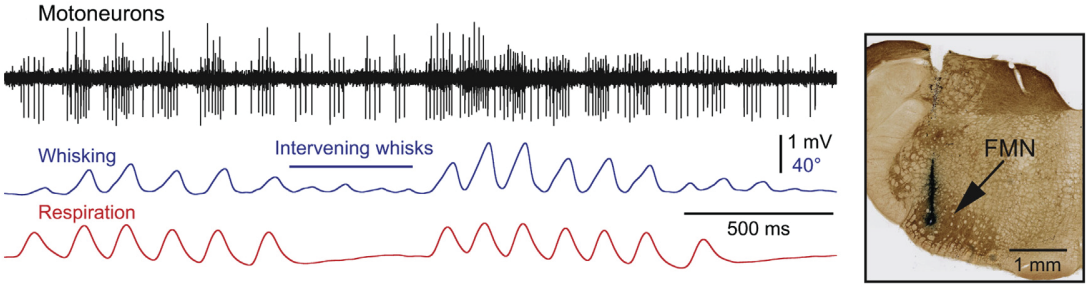

Figure 2.2: Firing of whisking facial motoneurons during whisking in a head-restrained rat. (left) Firing of facial motoneurons during whisking in a head-restrained rat. Both cells discharge during vibrissa protraction, including whisks that are not associated with a breath (intervening whisks). The positive unit is recruited as whisk amplitude increases. (right) Labeling of the recording site by an iontophoretic deposit of Chicago sky blue. FMN, facial motor nucleus.

One may ask whether the firing pattern of facial motoneurons during KA-induced whisking is consistent with that observed during natural whisking. Of central interest, we sought to determine whether self-generated whisking involves rhythmic inhibition of motoneurons that drive the intrinsic vibrissa muscles. We thus recorded from facial motoneurons in alert head-restrained rats. Single-unit recordings from calm but whisking animals revealed two populations of rhythmic cells: motoneurons that fire during protraction of the vibrissae (24 cells in three rats), and motoneurons that fire during respiration or sniffing (15 cells in three rats). The former motoneurons were distinguished from respiration-modulated motoneurons by their rhythmic discharges during intervening whisks, which are whisks that are not associated with a breath [74]. As in the KA model of whisking, no motoneuron fired preferentially during vibrissa retraction,

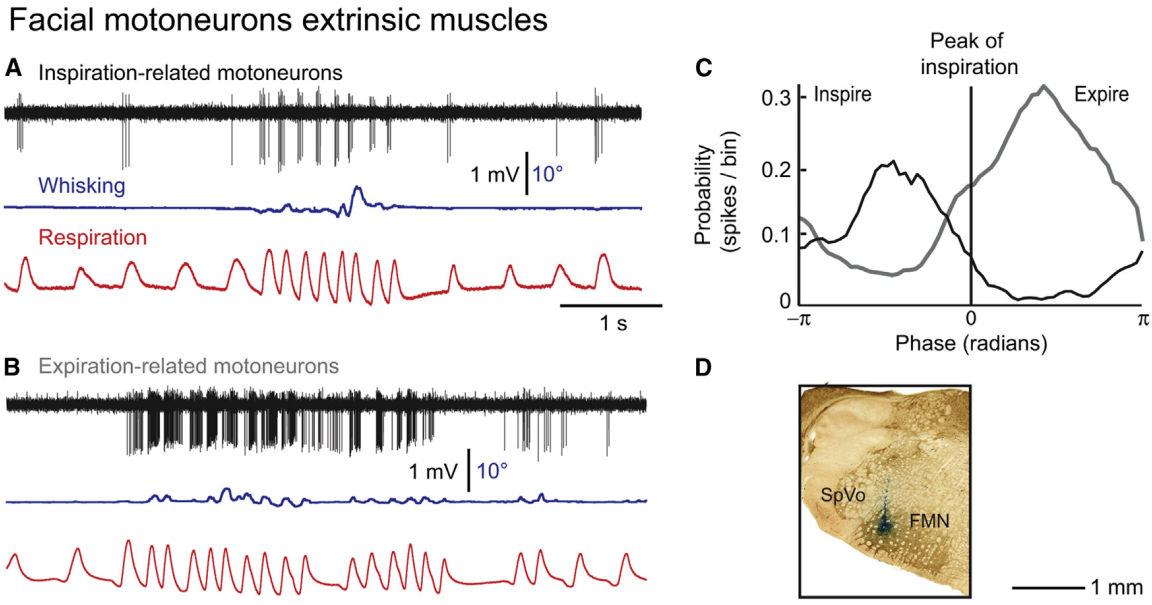

Figure 2.3: Firing of respiratory facial motoneurons during whisking in a head-restrained rat. (D) Firing of facial motoneurons during whisking in a head-restrained rat. Both cells discharge during vibrissa protraction, including whisks that are not associated with a breath (intervening whisks). The positive unit is recruited as whisk amplitude increases. (E) Labeling of the recording site by an iontophoretic deposit of Chicago sky blue. FMN, facial motor nucleus.

and none of the motoneurons displayed both whisking and respiratory modulation

Whisking modulated motoneurons were active during low-amplitude whisks increased their firing rate with the amplitude of vibrissa protraction, and additional motoneurons were recruited as the amplitude of vibrissa movement increased (Figure 2.2). Retraction of the vibrissae was associated with an arrest of discharges.

Among respiration-related motoneurons, some fired in a one-to-one manner with each inspiration during both basal respiration and sniffing (four cells in three rats), while others were mainly recruited during high respiratory drive (11 cells in three rats; Figures 2.3A and 2.3B). In both cases, rhythmic firing was locked to either the inspiratory or the expiratory phase of breathing (Figure 2.3C).

2.4 Bilateral whisking is synchronized by the respiratory CRGs

In the absence of external objects or head turning, natural whisking is bilaterally synchronous [34, 83, 101, 72], which requires a circuitry that coordinates the activity of the left and right whisking CRGs. Yet, bilateral injections of KA result in incommensurate vibrissa motion [75], as measured in anesthetized animals, suggesting a lack of direct coupling between the left and right vIRts (Figure 2.4). We assessed the independence of vIRt oscillators in alert rats by comparing the degree of bilateral coherence between sniff-locked and intervening whisks (Figure 2.4C). If both oscillators are independent from one another, one expects intervening whisks to drift in phase when the respiratory CRG is transiently halted. We therefore selected whisking bouts that occurred after spontaneous sighs, when the expiratory period lasted for at least 500 ms, and compared them with random segments of whisking while sniffing. Spectral analysis reveals a significant diminution of coherence for intervening whisks, together with high variability (Figure 2.4D) and a phase shift (Figure 2.4E), which is consistent with the notion that the two whisking CRGs are independent from one another, and therefore begin to drift in the absence of repeated

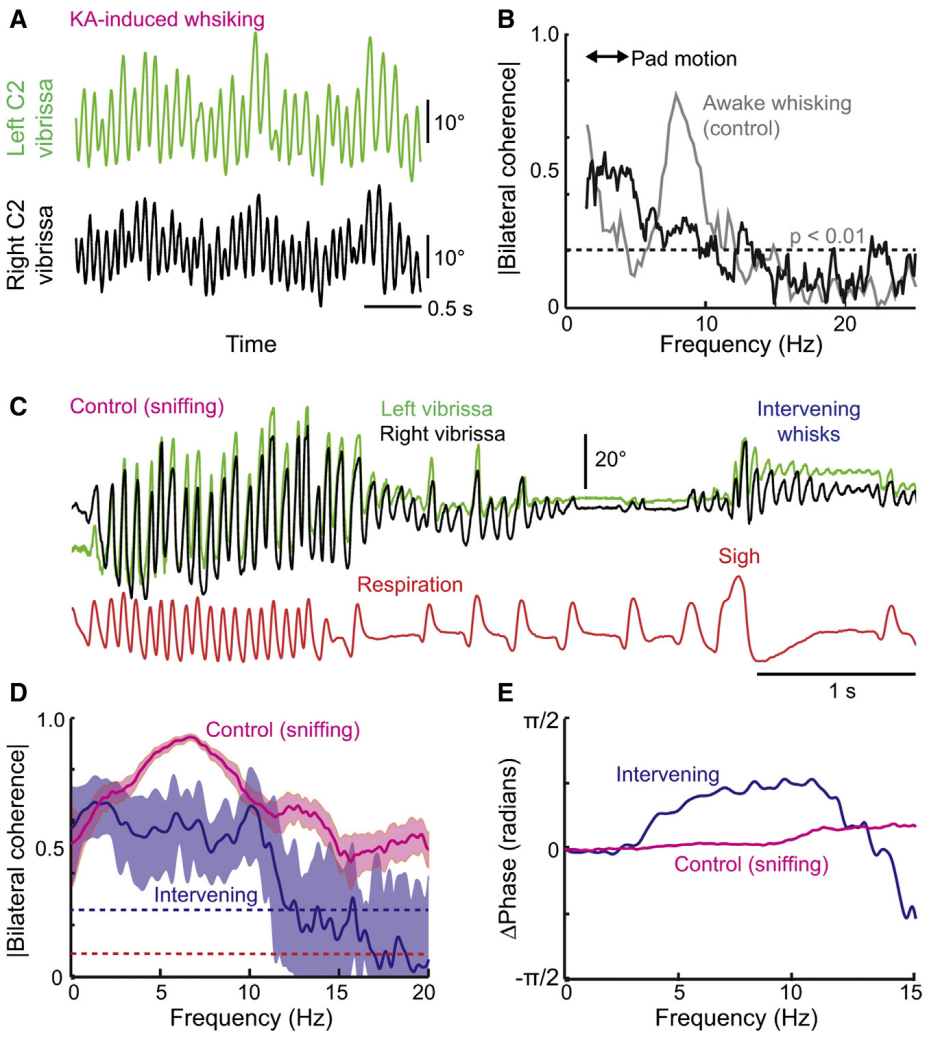

Figure 2.4: The Left and Right Whisking Oscillators Are Independent from One Another (A) Bilateral kainic acid injection produces independent vibrissa movements on the left and right sides of the face. (B) Spectral coherence (black trace) between the movements of each of the vibrissae in (A). The two signals show low coherence in the band of whisking frequencies relative to control data for bilateral active whisking in alert animals (gray trace). (C) Representative traces of whisking and respiration used to compute average bilateral coherence between sniff-related and intervening whisks in three head-restrained rats. (D) Average coherence between left and right intervening whisks is lower than that of sniff-related whisks. Light blue and red areas represent 95% confidence interval. (E) Whisks on the left and right sides of the face display virtually no phase difference during sniff-related whisks (red line), whereas intervening whisks display a clear phase shift (blue line).

resetting events.

2.5 Conclusions

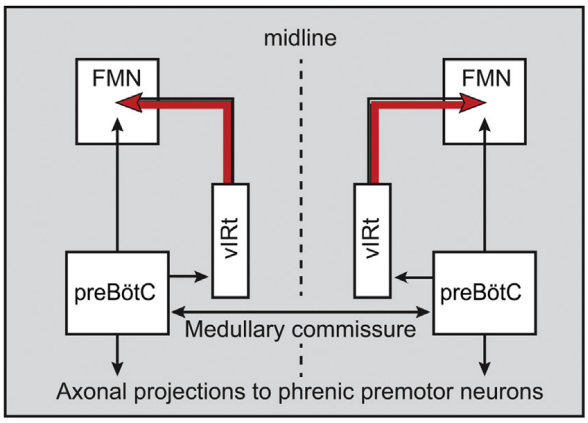

Figure 2.5: Whisking and breathing proposed circuit: The reset of whisking by breathing is mediated by unidirectional connections from preBötC to vIRT, and commissural fibers that connect the left and right preBötCs ensure bilateral synchronization of whisking.

Figure 2.5 presents a summary of the proposed circuit based on the results of analysis of the whisking CPG and facial motor nucleus recordings. We propose that the reset of whisking by breathing is mediated by unidirectional connections from preBötC to vIRT, and commissural fibers that connect the left and right preBötCs ensure bilateral synchronization of whisking. The vIRT oscillators themselves do not connect on the two sides.

2.6 Methods

Electrophysiology in Alert Head-Restrained Rats Rats were habituated to body restraint for 5 days. Then they were implanted with a custom-built head-restraining mount, and a thermocouple (K-type; Omega Engineering) was placed in the nasal cavity to monitor respiration [74]. Surgical procedures were carried out in animals anesthetized with ketamine (75 mg/kg) and xylazine (5 mg/kg). Rats were allowed to recover for 3 days before the onset of behavioral experiments.

During the recording sessions, rats were placed inside a body-restraining cloth sack and rigid tube, and the animals were head restrained. Rats were briefly anesthetized with isoflurane, and a craniotomy was performed over the cerebellum to get access to the facial nucleus. A drop of local anesthetics (bupivacaine) was applied over the dura, and the dura was open by local heating with a fine-tip cauterizer. Anesthesia was stopped, and neuronal activity was recorded in the facial nucleus using quartz micropipettes with a tip diameter of 4-8 mm, filled with 2% (w/v) Chicago sky blue (Sigma) in 0.5 M NaCl.

All vibrissae except C2 or D2 were cut at the base, and movement of the intact vibrissa was monitored on line with a Basler A602f camera operated in line-scan mode. Rats were coaxed to whisk by presenting food or bedding from the home cage [33]. One recording site was marked in each rat with an iontophoretic deposit of Chicago sky blue (5-10mA with 10 s pulses spaced every 20 s for 5 min). Rats were deeply anesthetized at the end of the session and perfused with PBS and then with 4% (w/v) paraformaldehyde in PBS. Brains were post-fixed for 2 hr, cryoprotected in 30% (w/v) sucrose in PBS, and sectioned along the coronal plane at a thickness of 50 mm with a freezing microtome. Sections were stained for cytochrome oxidase. Data were obtained from three rats in which the deposit of Chicago sky blue was found in the lateral part of the facial nucleus.

Data Analysis The relationship between unit activities and the whisking or breathing rhythms was estimated by computing the spectral coherence [73]. Single whisks or breaths were isolated by band-pass filtering the position traces between 1 Hz and 25 Hz with a three-pole Butterworth filter run in forward and backward directions, and applying the Hilbert transform [50]. The Chronux toolbox (http://chronux.org) was used to compute coherence between spike times or intracellular events averaged over 2 s segments with a time-bandwidth product of two. Basal respiration was defined as the instantaneous respiratory frequency below 4 Hz and sniffing as the instantaneous respiratory frequency greater than 4 Hz. We report the magnitude and phase of the coherence at the peak frequency of whisking or breathing. A phase of zero corresponds to

the peak of protraction or inspiration. The degree of bilateral coherence between sniff-locked and intervening whisks was analyzed in three head-restrained rats. We selected intervening whisks occurring after a sigh, when respiration is transiently halted. This analysis was performed with 15, 40, and 38 intervening whisk clips, and 128, 23, and 73 clips of whisking while sniffing, in each of the three rats respectively.

In total, this corresponds to 17.4 s of intervening whisks and 238.4 s of sniffing in rat 1, to 26.5 s of intervening whisks and 50.9 s sniffing in rat 2, and 34.1 s of intervening whisks and 107.3 s of sniffing in rat 3. Analysis of motor unit activity was carried out using spike sorting (Labchart 7.3) and custom-written scripts in MATLAB. We chose sequences that contained both basal respiration and sniffing bouts associated with whisking, and during which motor units discharged in a sustained manner. Circular phase histograms of motor unit discharges were constructed using bin size of 0.34 radians.

2.7 Author contributions

Chapter 2 includes work that is currently published in: M. Deschênes, J. Takatoh, A. Kurnikova, J.D. Moore, M. Demers, M Elbaz, T. Furuta, F. Wang, D. Kleinfeld, Inhibition, not excitation, drives rhythmic whisking", *Neuron*, 2016. and J. D. Moore, M. Deschênes, A. Kurnikova, D. Kleinfeld. "Activation and measurement of free whisking in the lightly anesthetized rodent", *Nature Protocols*, 2014. Figures included in the dissertation were contributed by the dissertation author. This material is included in Chapter 2 with the generous consent of all coauthors.

Chapter 3

Movement of the nose

3.1 Summary

The delineation of sensorimotor circuits that guide exploration begins with an understanding of the pattern of motor outputs [100]. These motor patterns provide a clue to the form of the underlying circuits [68, 62, 24] (but see [14]). We focus on the behaviors that rodents use to explore their peripersonal space through goal-directed positioning of their nose, head, and vibrissae. Rodents sniff in response to novel odors, reward expectation, and as part of social interactions [106, 18, 9, 103, 108, 56, 80]

Sniffing serves olfaction [57, 86], while whisking synchronized to sniffing serves vibrissa-based touch [106, 74, 23]. We quantify the ethology of exploratory nose and head movements in relation to breathing. We find that sniffing is accompanied by prominent lateral and vertical deflections of the nose, which are driven by activation of the deflector nasi muscles [20]. On the timescale of individual breaths, nose motion is rhythmic and has a maximum deflection following the onset of inspiration. On a longer timescale, excursions of the nose persist for several breaths and are accompanied by an asymmetry in vibrissa positioning toward the same side of the face. Such directed deflections can be triggered by a lateralized source of odor. Lastly, bobbing of the

head as the animal cranes and explores is phase-locked to sniffing and to movement of the nose. These data, along with prior results on the resetting of the whisk cycle at the onset of inspiration [74, 23, 82], reveal that the onset of each breath initiates a 'snapshot' of the orofacial sensory environment.

3.2 Results

Rats sniff as they explore, where sniffing is taken as breathing rates greater than 4 Hz. In contrast, basal respiration is relatively slow, conservatively taken as rates of less than 2 Hz. We measure the position of the nose versus time, concurrent with measurements of breathing, in head-restrained animals (Figure 3.1,3.3). As the rat sniffs, we observe two components of nose movement in the lateral and vertical directions. One is a slowly varying 'bias' in nose positioning and the other a smaller rhythmic nose movement that is centered around the slowly varying bias in mean position (Figure 3.2A). We correlate the rhythmic component of nose motion to breathing where we separate bouts of sniffing from basal breathing. We find that the time to reach to maximum excursion, for both lateral and vertical nose positions, occurs slightly after the onset of inspiration (n = 3 rats) (Figure 3.4A). The maximum speed of the movement in the lateral directions occurs during expiration for sniffing and just prior to inspiration during basal respiration (Figure 3.4A). Consistent with this, the coherence of lateral and vertical nose speed to breathing is statistically significant at the sniffing frequencies and has a phase shift close to p radians (Figures 3.6B). Lastly, we note that motion of the nose in the third, rostrocaudal direction is found to correlate with vertical motion and thus not considered for future analysis (Figure 3.6). These findings establish the basic coordination of nose movement with sniffing.

Further insight into the rhythmic motion of the nose is found from a scatterplot of the maximum excursions of the nose in the lateral direction relative to the onset of breathing. The times corresponding to the maximal excursion were plotted in relation to the onset of inspiration,

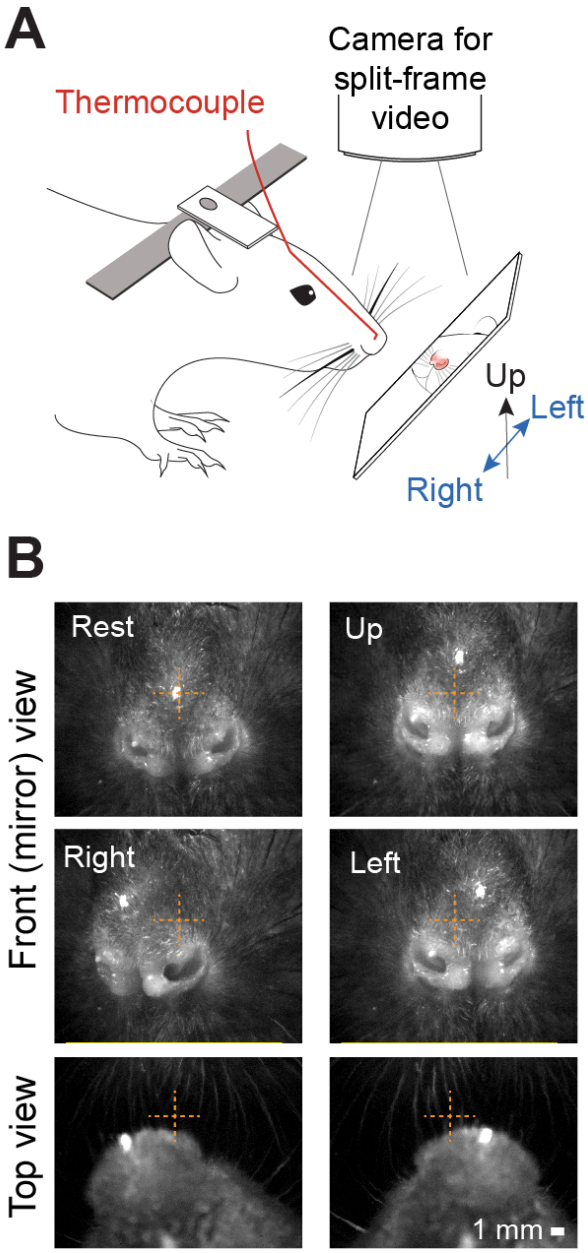

Figure 3.1: Recording setup for nose motion. (A) Schematic of the experimental setup for recording breathing and three-dimensional nose motion in a head restrained rat (top). A thermocouple is implanted in the nasal cavity to monitor breathing. A charge-coupled device (CCD) camera is mounted above rat, and a split frame is used to simultaneously image lateral and rostrocaudal nose motion from the top view, and lateral and vertical motion via a mirror in front of the rat that is set at 45 degrees (B) Two example split frames and two additional front view frames.

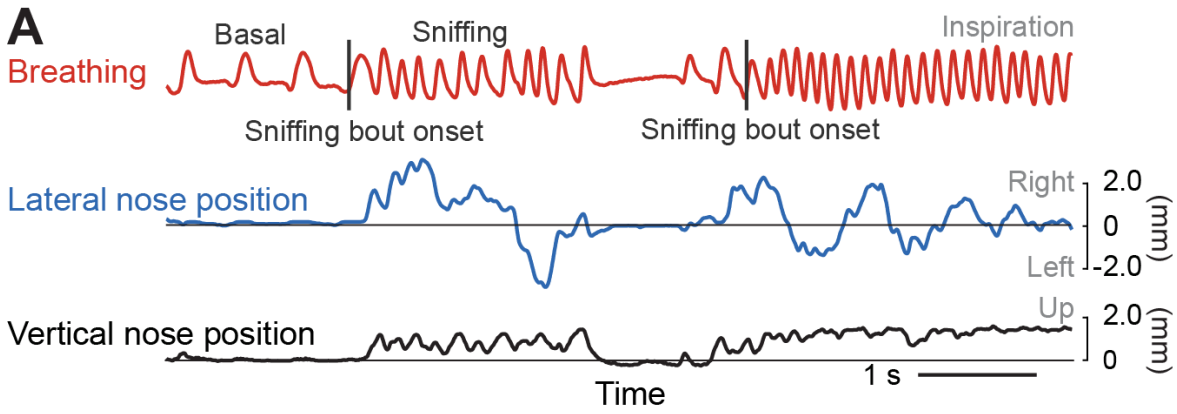

Figure 3.2: Example nose motion time series. (A) Time series of breathing (red) along with lateral (blue) and vertical (black) nose motion. The nose tends to move during sniffing epochs and moves little during basal respiration. Sniffing bout onsets are marked by a tick.

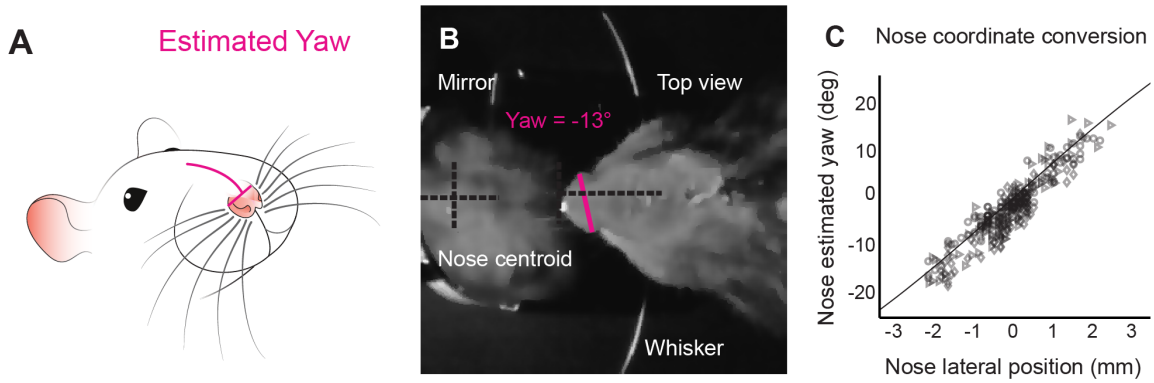

Figure 3.3: Motion of the nose conversion to angle. (A) Diagram of estimated yaw (magenta). (B) Example frame with nose deflected and yaw (magenta) tracked by hand as the angle between nostrils. Angle calculated as angle of the line. In the example Yaw = -13 (C) Example angles from 3 rats (square, circle, triangle) are tracked by hand as shown in yellow in panels B and C. Fit line shown is least squares fit to Yaw = arctan (Position/Distance to Fulcrum) The effective fulcrum calculated from this fit is 7.6 mm caudal to the tip of the nose.

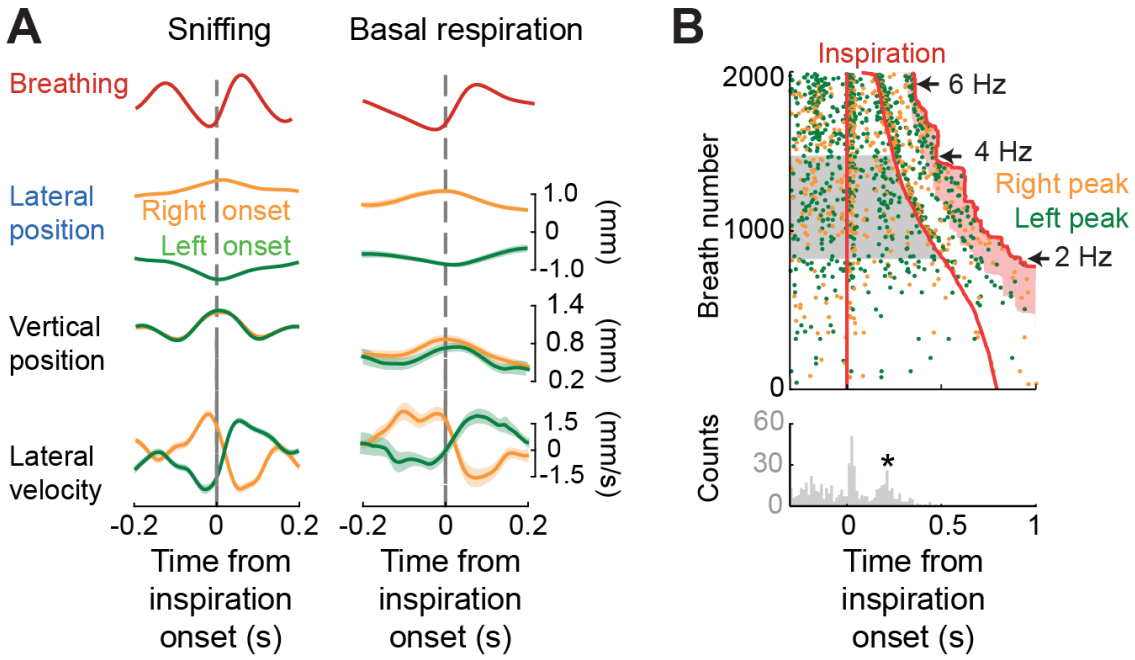

Figure 3.4: Relation of nose motion to breathing. (A) Inspiration triggered average of breathing (red) and nose motion (orange and green) for sniffing, i.e., 4 and 6 Hz breathing rate (left) and basal respiration, i.e., < 2 Hz breathing rate (right). Trials were selected for averaging as right-going (positive amplitude; orange) or left-going (negative amplitude; green) if the value at the time of an inspiration onset was at least 0.5 mm from the center. Right- and left-going trials were averaged separately. Calculation performed with 560 trials (sniffing) and 98 trials (basal) of data across three rats; all error bars are SEM. (B) Raster plot of nose lateral position peaks, thresholded with a 0.5 mm minimum displacement, in relation to the breath rise. Trials are sorted by breath duration and the direction of the lateral movement; right motion is orange and left motion is green. The histogram shows the time for the lateral motion to peak for intermediate breathing frequencies (2.0 - 4.0 Hz, highlighted in gray); only data prior to the second breath is included. The second peak in nose displacement (+) occurs 0.34 s after the onset of inspiration. Data are from a single animal.

with trials sorted by breathing rate (n = 3 rats) (Figure 3.4B). We observe that the peak excursion occurs at a fixed time after the initial and second inspiration, as seen in the correlation (Figure 3.4A). In an interval where breathing is slower, i.e., 2 to 4 Hz (gray band in Figure 3.4B), we see that the position of the nose obtains an additional peak excursion at a fixed interval after the first breath but before the next breath (+ in Figure 3.4B). The presence of this additional peak is highly suggestive of an underlying oscillator for rhythmic nose movement that can function independently of the breathing rhythm. Analogous to the case for whisking [74], this hypothetical oscillator is reset by breathing.

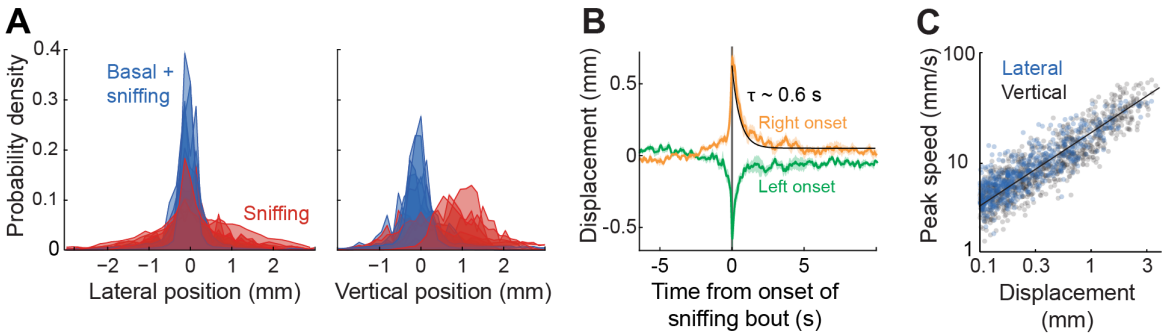

Figure 3.5: Quantification of nose motion. (A) Histograms of the lateral and vertical nose positions for six rats. Blue histograms include values for both basal respiration and sniffing, while red histograms include only sniffing epochs. (B) Average lateral position of the nose relative to the onset of a sniffing bout (B). Trials were sorted into right onset (orange) and left onset (green) by the average value within 100 ms of the sniffing bout onset. An exponential fit was calculated on the average of all traces, starting at time t = 0; black line. (C) Scatterplot of the speed of lateral displacements versus the length of the displacement. Each length is defined by a starting and ending with a change in the sign of the velocity. Log-log plot; the line is a fit to the logarithm of the data with slope 0.63 ± 0.03, where the uncertainty is the 0.95 confidence interval.

We now turn to the slowly varying bias in lateral and vertical displacements of the nose that accompany sniffing but rarely occur during basal respiration (Figure 3.5A). Lateral nose displacements occur in both directions in the range of approximately $\pm$ 2 mm, while vertical displacements occur in the range of 0 to 2 mm (Figure 3.5A). The typical duration of bias in the direction of lateral nose motion is found by averaging right- and left- initiated movements that are

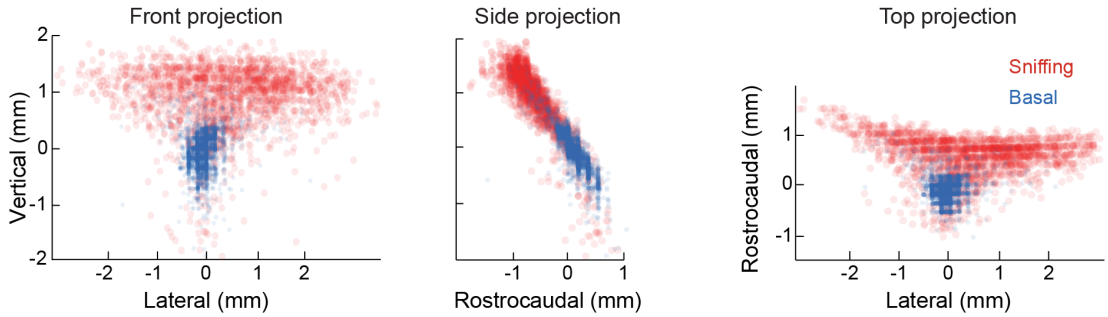

Figure 3.6: 3D projections of histogram of nose positions. Front, Top and Side projections shown. Red dots show nose positions during sniffing (> 3 Hz respiration). Blue dots show nose positions during basal (< 3 Hz) respiration. The small rostrocaudal deflection correlates to the vertical motion, with 94 $\pm$ 2 % of the variance of the three dimensional motion described by the two dominant principal components.

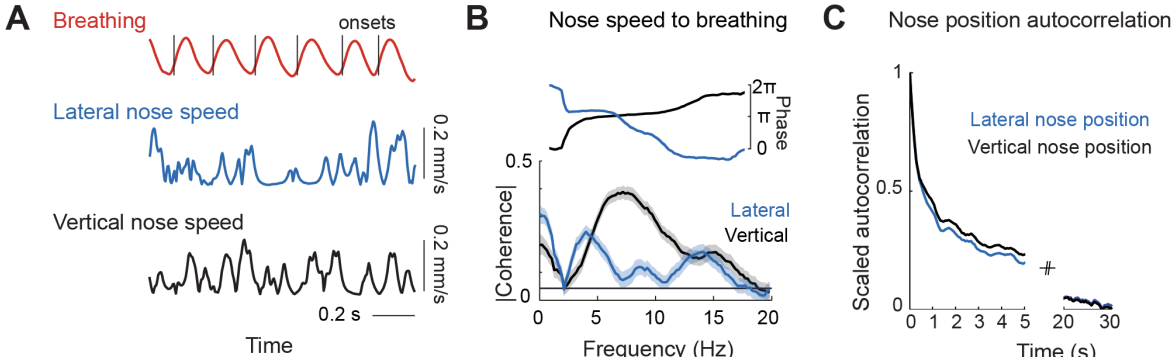

Figure 3.7: Coherence of nose motion to breathing. (A) Example 3 s clip of sniffing used to calculate coherence of nose velocities to breathing. Breathing is shown in red, with breath rises identified with black lines. Blue and black traces show the absolute value of the lateral and vertical velocities of nose motion. (B) Coherence to breathing and phase of the lateral (blue) and vertical (black) velocities of nose movement during sniffing. The calculation was done on 3 s segments during which sniffing frequency was between 4 Hz and 8 Hz for a majority of the segment. Calculation performed with data from 3 animals. (C)Scaled autocorrelation of lateral (blue) vertical (black) nose position. Autocorrelation for both drops to 1/2 max at around 0.6 s, and reaches zero by 30 s.

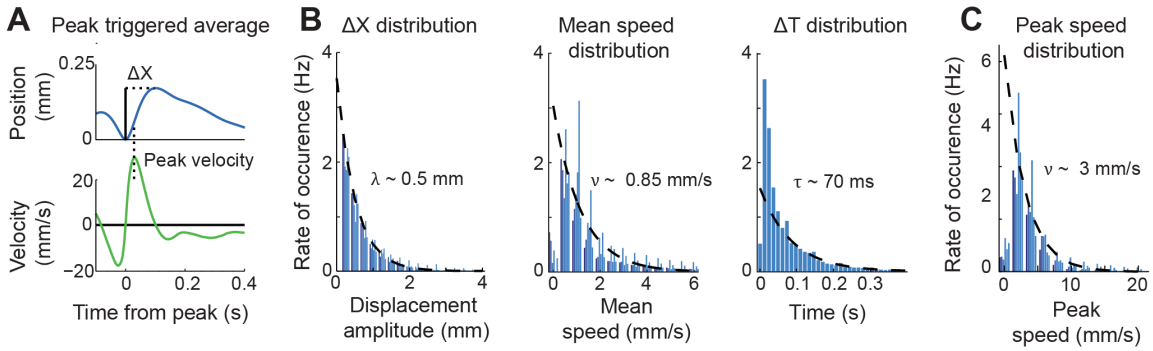

Figure 3.8: Parameters of nose motion. (A) Average position (blue) and velocity (green) traces from each peak position in lateral nose motion. Velocity was calculated as the derivative of the spline fit to the position trace. Maximum displacement and peak velocity are indicated by dotted lines. (B) Histograms of displacements between peaks in lateral motion and mean velocities between peaks for 6 rats (shades of blue), and histogram of times between peaks pooled across 6 rats. Black dotted line is an exponential fit to the histograms excluding values at less than 0.1 mm (displacement), 0.5 mm/s (velocity), and 30 ms (time). Displacement fit is Rate = 3.5 exp(-Δx/0.5 mm), indicating a characteristic displacement of λ = 0.5 mm. Velocity fit is Rate = 3.0 exp(-Δ v/0.9 mm/s), indicating a characteristic mean speed of ν = 0.9 mm/s Time fit is Rate = 1.5 exp(-Δ/70ms), indicating a characteristic speed of τ = 70 ms (C) Histogram of peak velocities between peaks. Black dotted line is an exponential fit to the histograms excluding values near at less than 2 mm/s. Fit is Rate = 8.3 exp(-Δv/3.0 mm/s), indicating a characteristic speed of ν = 3 mm/s

aligned to the onset of each sniffing bout; onsets are identified as an abrupt increase in breathing rate by at least 1.5 Hz (Figure 3.5B). We find that both right and left excursions of the nose have a persistence time of 0.7 s, or about three sniff cycles, for 0.7 of the movements and a persistence time of 7 s for 0.3 of the movements (n = 6 rats) (Figure 3.7B). Over 0.6 to 0.7 s, the nose tends to move 0.5 to 0.6 mm with a characteristic average speed of 0.9 mm/s (Figures 3.5B and 3.6C and 3.7C), although the characteristic maximum speed is much greater, i.e., 3 mm/s (Figures 3.7B and 3.7C). A point of interest is that the relation between the displacement and instantaneous speed of the nose is well described by a power law (Figure 3.7C). This takes the form:

$$speed \propto displacement^{0.63 \pm 0.03}$$

The exponent is close to 2/3, suggestive of motion control that minimizes jerk, the derivative of acceleration, along the movement trajectory of the nose [109].

What is the nature of the motor plant that drives motion of the nose? Past work showed that artificial activation of the deflector nasi (d. nasi) muscles elicits lateral and vertical movement of the nose [20]. To understand the role of these muscles as the rat explores, we performed simultaneous recordings of the electromyogram (EMG) of d. nasi on both sides of the face concurrent with videography of the head-restrained rat (3.9A). Typically both muscles are active. In the extreme, unilateral EMG activity of *d. nasi* leads to a combined ipsilateral and vertical deflection (+ in Figure 3.9B), while bilateral activity pulls the nose upward (+ in Figure 3.9B).

More generally, our results suggest a model in which each *d. nasi* deflects the nose ipsilaterally and upward and the resulting nose position is a vector sum of the activation of the *d. nasi* on each side (Figure 3.10). Additional details of the muscular control are revealed by a correlation analysis across data from all animals (n = 3) (Figure 3.11). First, we performed a cross correlation of the ipsi- and contralateral *d. nasi* EMG envelopes. We observe a single peak at equal time, which indicated that the two muscles tend to be co-activated. Second, the peak of the cross-correlation between the envelope of the *d. nasi* EMG to lateral nose motion occurred

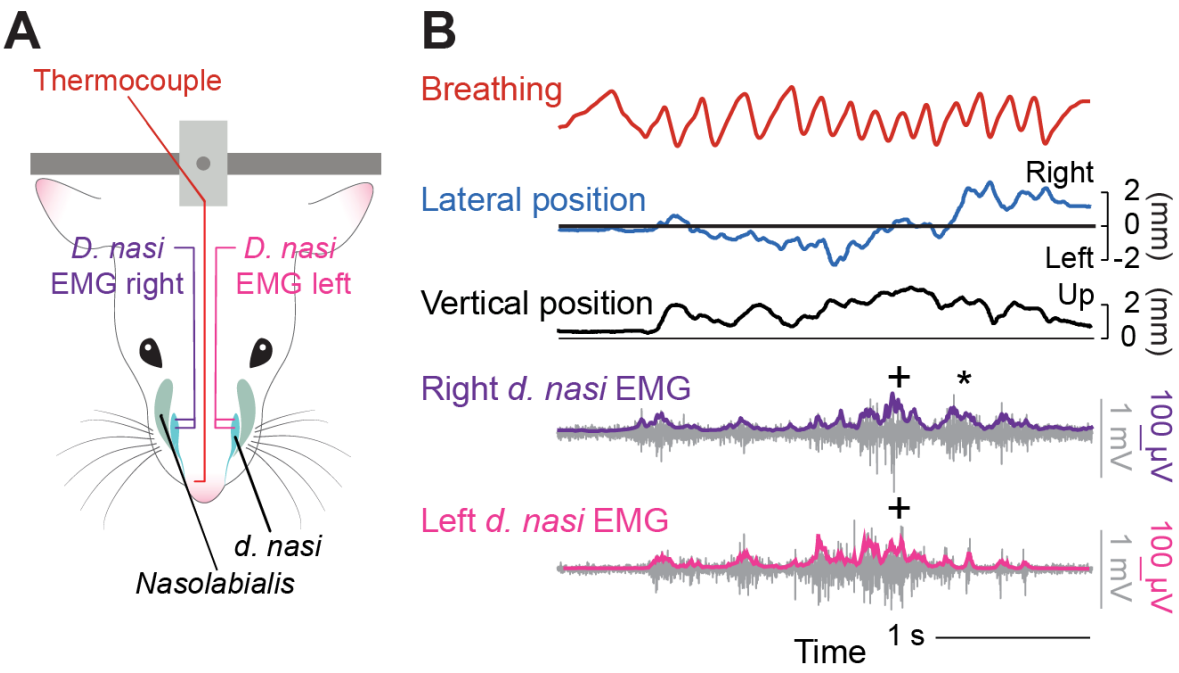

Figure 3.9: EMG from nose. (A) Schematic of the muscles in the snout. Two arrangements of EMG signals were measured. EMG wires were placed either bilaterally in the d. nasi, muscles or unilaterally in the nasolabialis,d. nasi, and vibrissa intrinsic muscles. The position of the nose is recorded through a CCD cam- era (B) Time series of lateral (blue) and vertical (black) nose position along with bilateral d. nasi EMG recordings. The EMG envelopes, right (purple) and left (magenta), are overlaid on the raw signal (gray).

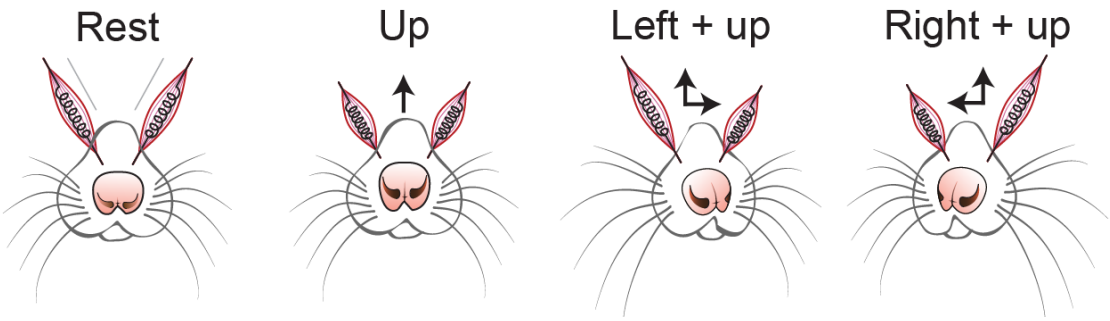

Figure 3.10: Diagram of nose movement with activation of the d. nasi muscles.

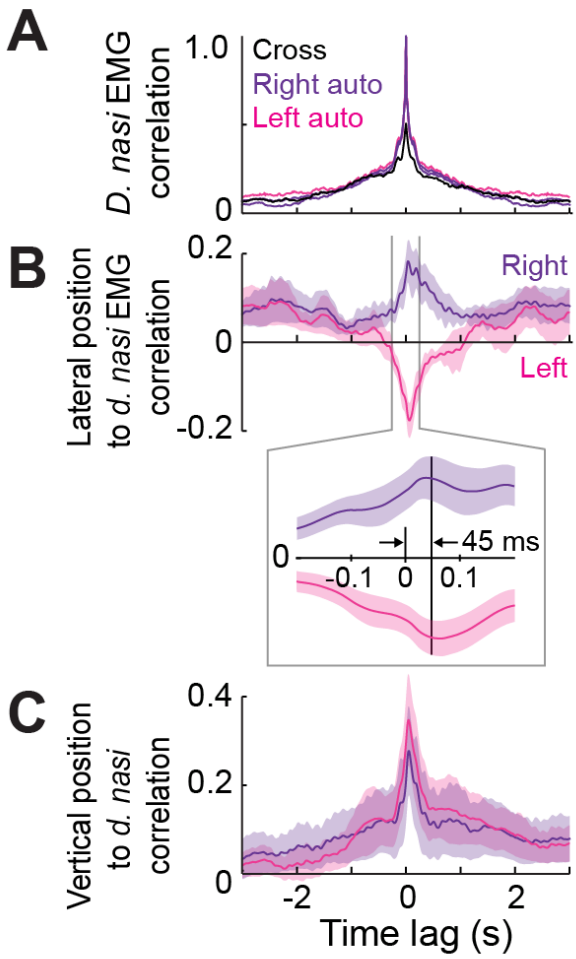

Figure 3.11: Relation of EMG from Nose to Lateral Nose Motion. (A) Normalized autocorrelation and cross-correlations of the bilateral d. nasi EMG envelopes. (B) Cross-correlations of right d. nasi EMG envelope with deflections of the nose to the right (purple) and left d. nasi EMG envelope with deflections to the left (magenta). The insert is an expansion near zero lag. (C) Cross-correlations of right and left d. nasi EMG envelopes with vertical displacement of the nose. Data pooled across 4,000 s of data across three rats.

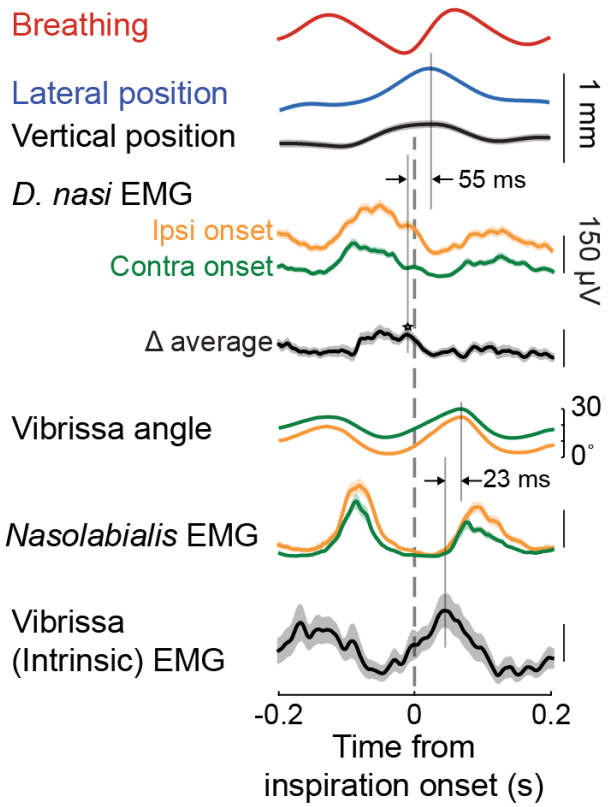

Figure 3.12: Relation of EMG from Nose, Mystacial Pad, and Vibrissa Muscles to Lateral Nose Motion. Triggered average of lateral (blue) and vertical (black) nose position, vibrissa position, and the EMG envelope in facial muscles with respect to the onset of inspiration during 4 to 6 Hz sniffing. The EMG data from *d. nasi* were sorted by ipsilateral (orange) and contralateral (green) onset of movement prior to rectification. Data pooled from 530 epochs across six rats.

with a mean lag of 45 $\pm$ 5 ms (mean $\pm$ SEM) (insert in Figure 3.11B), with a similar result for the vertical motion. This value reflects the viscoelastic time-constant of the nasal cartilage.

The timing between nose motion and whisking was explicitly revealed by recording the EMG in the *d. nasi* muscles simultaneously with the EMG from two muscles in the vibrissa motor plant. The intrinsic muscles are predominantly responsible for protraction during sniffing [50], while the nasolabialis muscle retracts the mystacial pad and is one of two muscle groups that contributes to active retraction during sniffing [50, 4]. The EMGs were sorted according to ipsilateral versus contralateral deflection of the nose with respect to the side of recording, and we computed the average response of each muscle with respect to the onset of inspiration (Figure 3.12). The envelope of the *d. nasi* EMG is observed to reach a peak value prior to the onset of inspiration (Figure 3.12). The activation of the *d. nasi* muscle is stronger during ipsilateral versus contralateral movement such that the difference of the sorted signals reaches a peak 55 ms prior to that of the nose position; this time difference is consistent with the directly measured delay between muscle activity and movement of 45 $\pm$ 5 ms (Figure 3.12). Our measurement of the two sets of muscles that comprise the motor plant for whisking support past data. First, the envelope of the EMG for the intrinsic muscles tracks inspiration [74] and precedes the peak in protraction by 23 ms [50]. Second, the envelope of the EMG for nasolabialis reaches a peak value prior to inspiration [23]. In new data, the peak displacement of the nose occurs 40 ms prior to the maximum protraction of the vibrissa (Figure 3.12). The bias in vibrissa and nose position occurs to the same side, i.e., during a sniff cycle the vibrissae ipsilateral to the nose deflection tend to be slightly retracted, by 5° (Figure 3.12). Lastly, activation of the *d. nasi* and the intrinsic muscles occurs essentially in anti-phase (Figure 3.12).

Motion of the nose is likely to play a critical role in the localization of sources of odorants [106, 16, 22]. We thus quantified nose motion in response to the controlled delivery of fumes from bedding of the home cage (Figures 3.15A and 3.15A) alternately to the left or right nostril (Figures 3.13A and 3.16). As a baseline response, we find that the rat begins to sniff and the nose

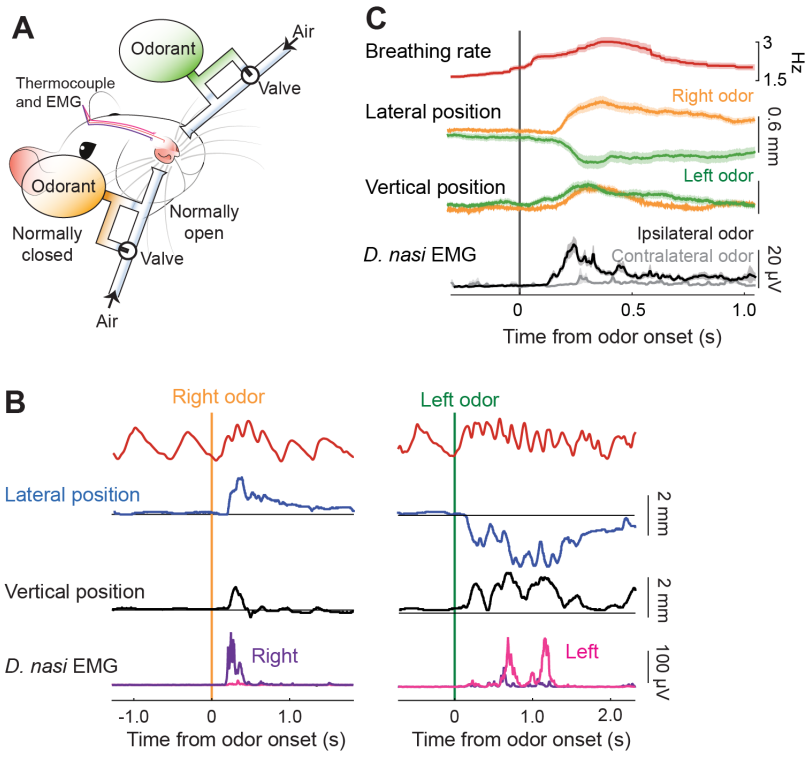

Figure 3.13: Lateral deflection of the nose towards an odor. (A) Schematic of the bilateral olfactometer setup. The rat is head-restrained, wired with electrodes for measuring the EMGs from the right and left d. nasi, and is fitted with a thermocouple to monitor breathing. Bedding odor can be presented alternately on the right (orange) or left (green) side by activating one of two three-way solenoid valves that maintain constant air flow with or without an odorant. (B) Example time series of the change in lateral (blue) and vertical (black) position, together with the right and left EMG and breathing signal, is response to bedding odor. Each of the two sets of traces is from a single trial. (C) The average response of the envelope of the EMGs from the d. nasi, displayed relative to contra- versus ipsilateral presentation of odorant. We further show the average change in lateral and vertical nose position to laterally presented bedding odor, with trials pooled by right (orange) and left (green) odor presentation. The breathing is shown as the averaged, instantaneous rate. Data pooled over 120 presentations across three rats.

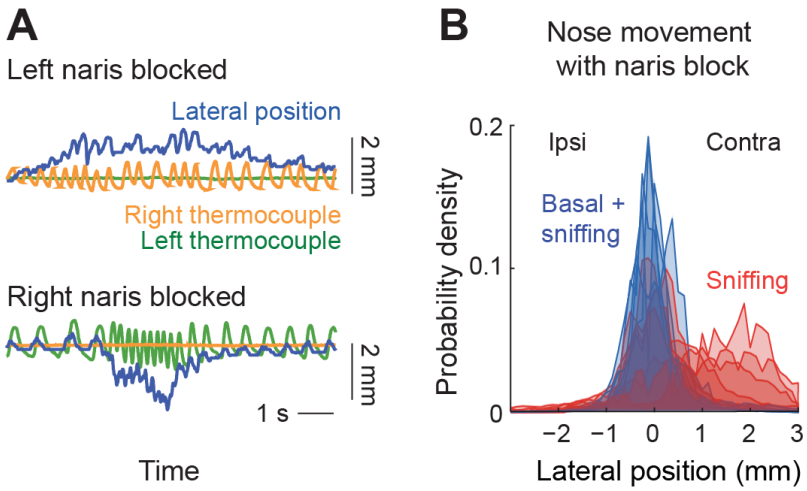

Figure 3.14: Lateral deflection of the nose biased with naris block. (A) Example time series of lateral nose position with one naris blocked. For these measurements, the rat had two thermocouples implanted, one is each nasal cavity. The right (orange) or left (green) thermocouple signal was observed to go to zero when the corresponding naris was blocked while the other thermocouple faithfully reported breathing (B) Probability density function of lateral nose position distribution with one nostril blocked during all recording time (blue) and during sniffing only (red). Data pooled over 1,040 s of recordings across 6 rats.

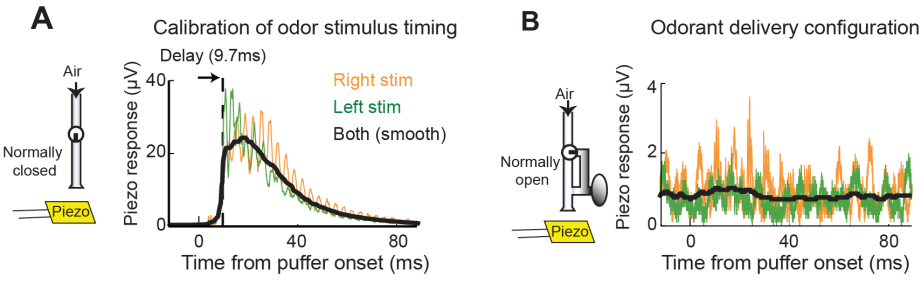

Figure 3.15: Configuration of odor stimulator. (A) Configuration of odor stimulator for timing test. Solenoid is con figured such that at the time of stimulus presentation an air puff is delivered. A piezo-electric film placed at the distance of the nose is used to record average air flow after stimulus. Trace of piezo response to right (orange) and left (green) stimulus. (B) Configuration of stimulator for odor test. Solenoid is configured such that at the time of stimulus presentation no air puff is delivered, and the air flow path changes such that the odorant is presented. With the same piezo-electric measurement as in panel C here is no apparent change in air flow at the time of stimulus presentation.

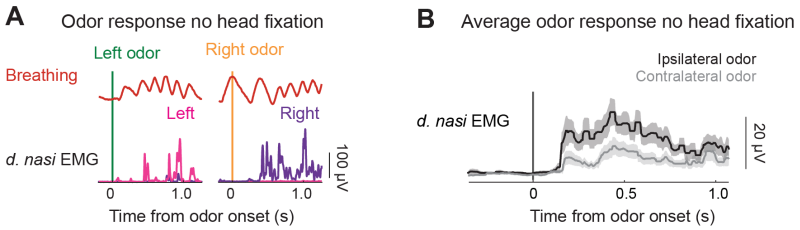

Figure 3.16: Non-head fixed response of nose to odor presentation. (A) Example trace of d. nasi. EMG envelope response to bedding odor presented laterally with the rat body restrained, but no head fixation. Right (purple) and left (magenta) *d. nasi* EMG envelopes and breathing signal are shown for a left (green) and right (orange) odor presentation. Each of the two sets of traces is from a single trial. (B) Average response of the *d. nasi* EMG envelopes in the absence of head fixation, displayed relative to contra- (grey) versus ipsilateral (black) presentation of odorant. Data pooled over 29 presentations across 3 rats.

lifts and deflects to the side of the presented odor (Figure 3.13B). The average response of the *d. nasi* muscles to an odor presented ipsilaterally or contralaterally shows that the ipsilateral muscle is strongly activated while the contralateral muscle is only weakly activated (Figures 3.13B and 3.13C). To confirm that the *d. nasi* muscles still activate in response to odor in the absence of head fixation, we repeated the measurement in body restrained rats. We found the same pattern of muscle activation, i.e., the ipsilateral muscle activated more strongly in response to lateralized odor presentation (Figures 3.16A and 3.16B). Finally, we consider the effect of blocking a nostril on the deflection of the nose. We first confirmed that blocking the nose on one side completely abolishes the breathing signal on that side (Figure 3.14A). Next, we recorded spontaneous nose motion. Consistent with curiosity driven motor actions, found that large deflections of the nose occurred primarily contralateral to the block and rarely to the blocked nostril (n = 5) (Figures 3.14B).

Beyond the slow change in the position of the nose (Figures 1F and 3C), slow changes in the amplitude and midpoint of whisking are well characterized [50, 4, 15]. We therefore consider the relationship between the lateral nose position and the shift in the midpoint of whisking. We used head-restrained rats and tracked the angle of the C2 vibrissa on each side of the face (Figure 3.17A), along with measurements of nose position and breathing (Figure 3.1). We find that

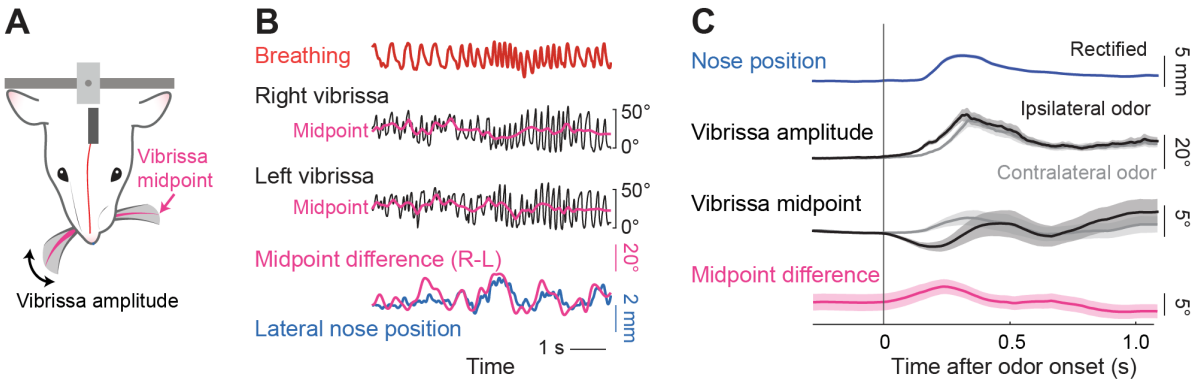

Figure 3.17: Vibrissa asymmetry relation to lateral deflection of the nose and odor presentation. (A) Schematic of the view of a CCD camera for tracking the vibrissae. In addition, breathing was measured with a thermocouple and the nose position was tracked in a single, front plane. (B) Time-series of breathing (red) and the position of the left (green) and right (black) C2 vibrissa. The midpoint of whisking was computed as the average between the upper and lower envelope of the cycle-by-cycle angle of the vibrissa. The difference between vibrissa midpoints (magenta) is scaled to overlap maximally with the lateral nose position (blue). (C) The olfactometer (A) was added to establish the response of the vibrissae to a bedding odorant. We show the time series of the whisking amplitude and midpoint along with the average nose position, rectified so that right and left deflections overlap. Trials were selected by criterion that lateral deflection of the nose in response to the odor exceeded 1 mm from rest. Data pooled from 177 trials across three rats.

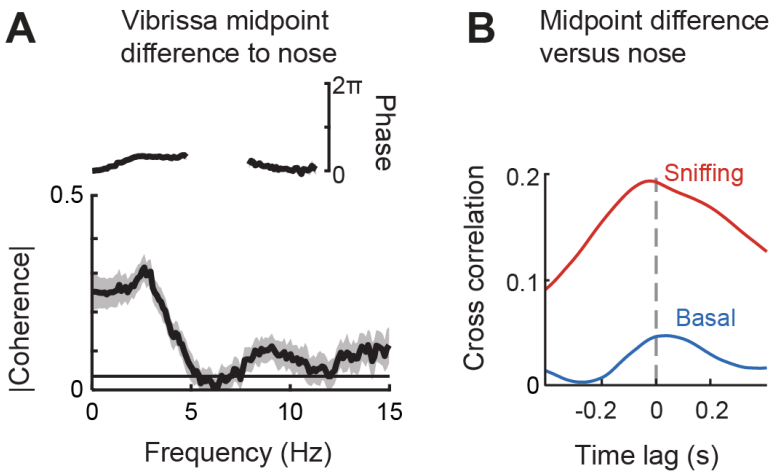

Figure 3.18: Relationship of vibrissa midpoint asymmetry to nose motion. (A) Coherence of vibrissa midpoint asymmetry to nose is significant at low frequencies, with a phase near 0. Error is 95 % confidence intervals. (B) Correlation of vibrissa midpoint difference to lateral nose position during sniffind epochs (red) and during all time (blue). Peak at 7 ms for sniffing trials (vibrissa asymmetry leading), and lower correlation during basal respiration. Cross correlations computed on 5 s segments during which breathing rate was over 3 Hz (sniffing) or under 2 Hz (basal). Data pooled across 3 rats

the asymmetry in midpoint of the vibrissa motion between the two sides of the face is highly coherent with the bias in lateral movement of the nose (Figures 3.17B and 3.18A), such that right-to-left shifts in the midpoint slightly lead deflection of the nose (Figure 3.18B). We next used the odor presentation paradigm (Figure 3.1A) to determine whether the vibrissae respond to a laterally presented odor. We observe an increase in the amplitude of whisking concurrent with odor presentations and that, consistent with the deflection of the nose toward an odorant, the vibrissae bank in the direction of the odorant (Figure 3.17C). This is similar to the case observed for banking of the vibrissae as a rodent changes head direction [101, 72]. Finally, we note that relation of the asymmetry in whisking to nose motion is weak for the case of basal respiration (Figure 3.18B) as opposed to sniffing.

We extended our behavioral measurements to establish the composite relation among movements of the head, nose, and vibrissae, all with respect to the sniff cycle. We begin with unrestrained rats whose heads were outfitted with a gyrometer and EMG electrodes implanted

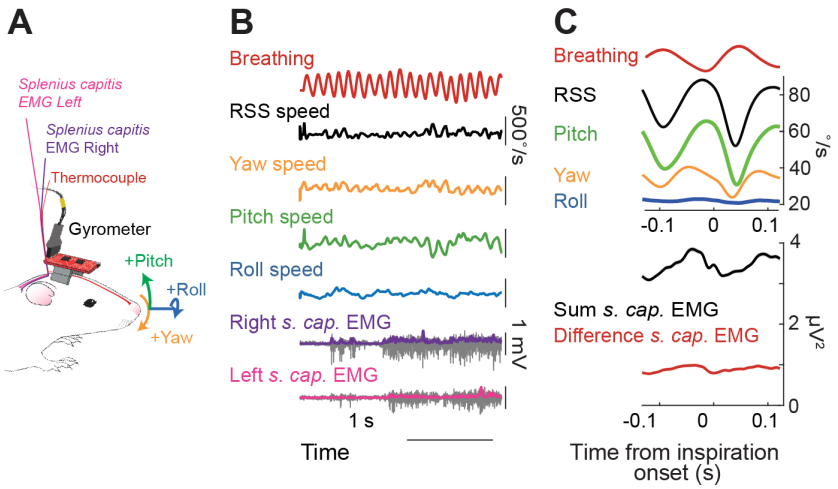

Figure 3.19: Head bobbing in relation to breathing. (A) Schematic of the setup for measurements of head angular motion relative to the breathing cycle. A three-axis gyrometer is mounted on the head to record pitch, roll, and yaw of head movement, and a thermocouple was implanted in the nasal cavity to measure breathing. All signals were routed through a commutator. (B) Time series of breathing (red), yaw velocity (orange), pitch velocity (green), and roll velocity (blue) of the head, along with EMG data from the right and left *splenius capitis* muscles during a sniffing bout. Angular speed (black). Both raw EMG data (gray) and the envelope (magenta and purple) are shown; the scale for the envelope is 125 mV. (C) Triggered average of breathing (red), individual angular velocities, angular speed (black), and the summed and difference EMG signals, with respect to the onset of inspiration. Data pooled over three animals with 20,500 sniff cycles. The error band is a 0.95 confidence interval.

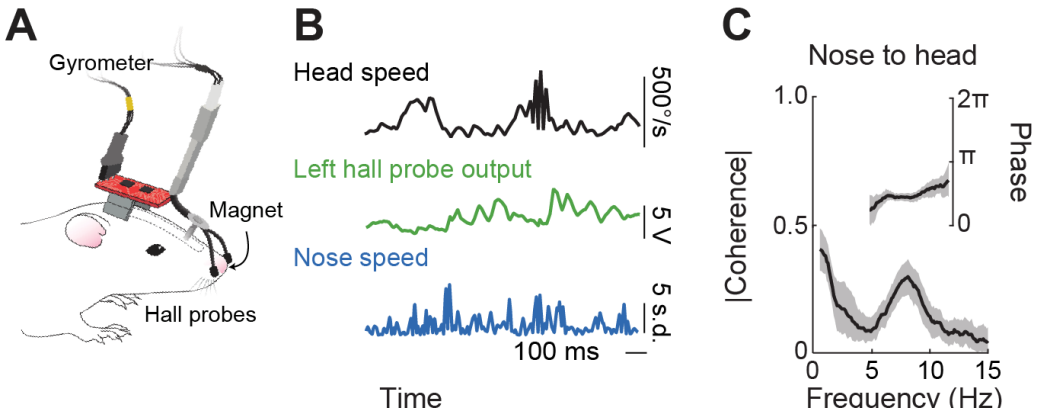

Figure 3.20: Head bobbing in relation to nose movement. (A) Schematic of the setup for measurements of head position relative to the nose position. A three-axis gyrometer is mounted on the head to record pitch, roll, and yaw of head movement, as in (A). Nose velocity was measured by a pair of Hall-effect probes mounted around the nose and a small magnet implanted in the nasal cartilage. (B) Time series of head speed (black), left Hall probe output (green) and normalized nose speed computed from the Hall probe signals (blue). (C) Spectral coherence of head speed and nose speed. Data pooled from 28 epochs, lasting 830 s, over 3 animals. The error band is a 0.95 confi- dence interval.

bilaterally in the *splenius capitis* muscles (Figure 3.19A), as well as a thermocouple as in the case of head-restrained rats (Figures 3.1A and 3.9A and 3.13A). The animals were placed on a small platform so that their body tended to remain still while they craned over the edges of the platform and performed successive head bobs (Figure 3.19A). Fumes from the home cage and other odors were presented to induce bouts of sniffing. We observe that the angular velocity of the head is dominated by rotations about the yaw and pitch axes, with only a small component of roll (Figures 3.19B and 3.22A). The cross-correlation between head speed and breathing demonstrates that head bobbing is coordinated with sniffing, with rhythmic movement of the head slowest at the midpoint of inspiration (Figure 3.19C). The peak head position occurs during inspiration and the full excursion of the rhythmic motion is estimated to be 0.4 mm (Figure 3.22B), close in value to the rhythmic excursion of the nose (Figure 3.19C). The cross-correlation between breathing and activation of the splenius capitis activation demonstrates that head bobbing is driven by rhythmic contraction of neck muscles (Figures 3.19C and 3.24A and 3.24C), as opposed to motion of the torso secondary to breathing. At the level of motion along each axis, only yaw and pitch are

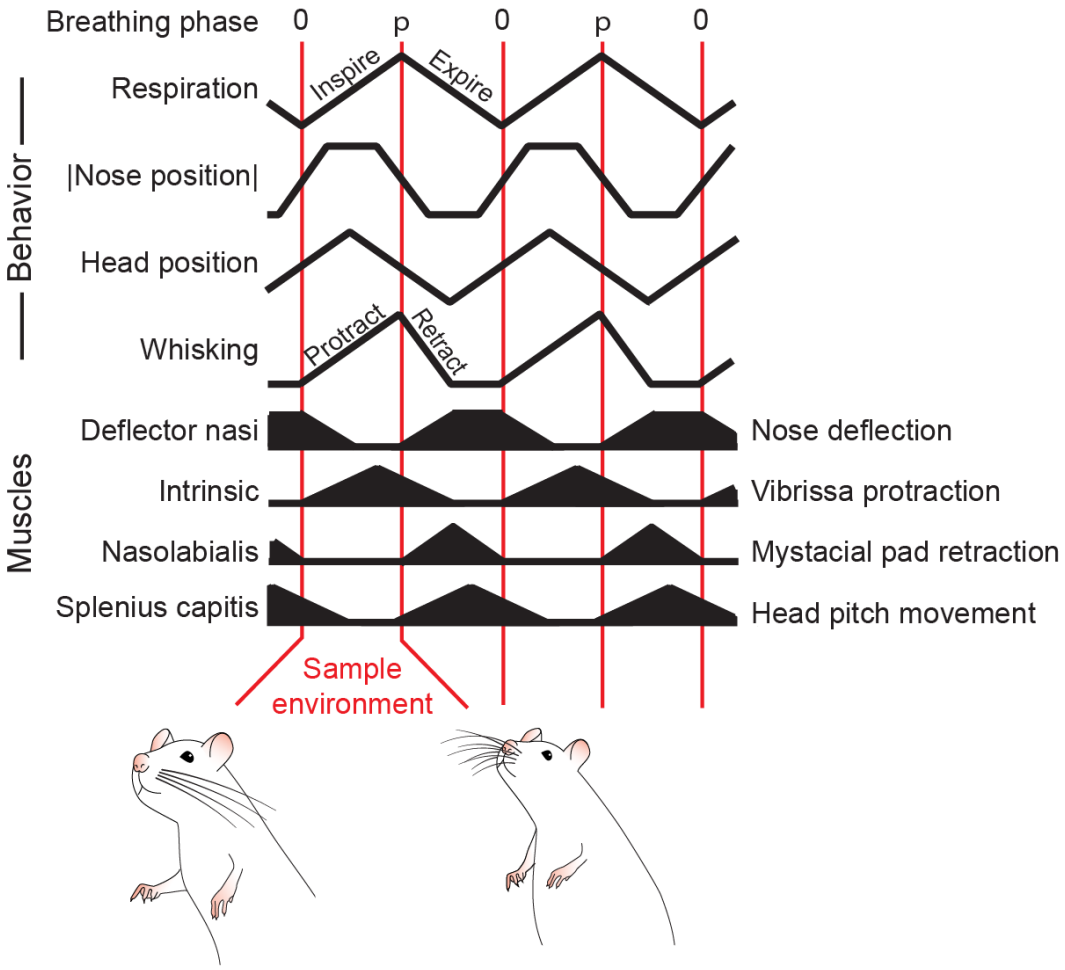

Figure 3.21: Summary of orofacial movements and muscle activity with respect to phase in the sniff cycle.

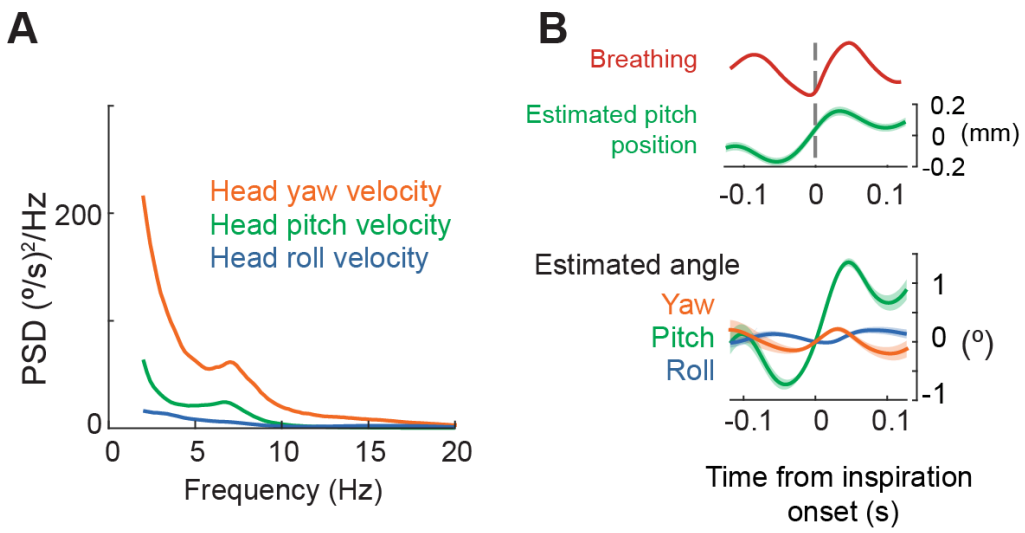

Figure 3.22: PSD of head movement parameters and head movement relation to breathing. (A) Power spectral density of head velocity during sniffing. Yaw (orange) pitch (green) and roll (blue) are calculated from accelerometer measurements. Calculation performed on same data as in part (A) (B) Inspiration triggered average of breathing (red) and estimated pitch position (green) for sniffing, i.e., > 4Hz breathing rate.

phase-locked to breathing at the sniffing frequency while motion along all three axes is locked to basal breathing (Figure 3.22B). As with nose movement, we conjecture that the coordination of head movement with sniffing, with head speed at a minimum value during inspiration, minimizes the disruption of a potential plume of odorants during sampling.

The observation that both exploratory movements of the head (Figure 3.19C) and nose (Figure 3.2) are coherent with breathing imply, but do not establish, that they are also coherent with each other. To independently verify that head and nose motion are in fact correlated, we outfitted rats with an indwelling magnetic sensor of nose movement as well as a gyrometer (Figures 3.20A and 3.23). The output of the probes change with shifts in magnetic field and thus reports nose position concurrent with measurements of head position (Figure 3.20B). We observe a significant peak in the spectral coherence between head and nose speed in the 6 to 9 Hz range of sniffing frequencies (Figure 3.20C), with a phase lag near p/2 radians, or a time lag of 30 ms at the peak frequency of 8 Hz. We conclude that nose movements are phase-locked to head

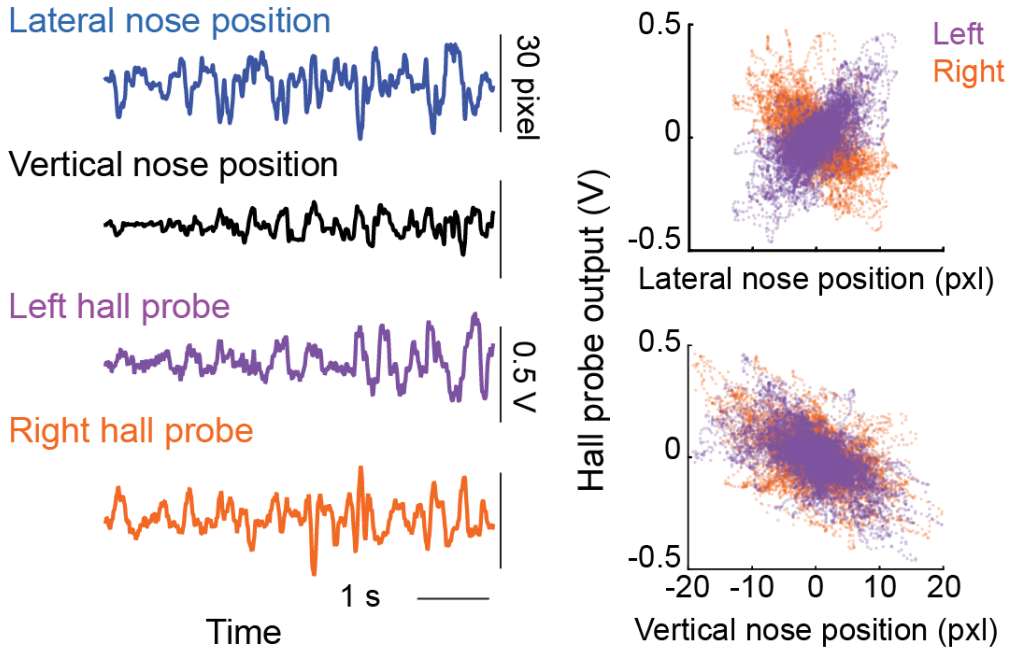

Figure 3.23: Splenius Capitis activity relation to breathing. (A) Coherence between Splenius Capitis EMG envelope and inspiration onset during epochs of sniffing. Left EMG (magenta) and Right EMG (purple) are shown. Calculation performed with data from 1 animal. (B) Raster plot of peaks in Left Splenius Capitis EMG envelope with respect to inspiration onset. Trials are sorted by breath duration. Data are from a single animal. (C) Coherence between head speed and inspiration onset during epochs of sniffing. Calculations represent angular speed (black), yaw speed (orange) pitch speed (green) and roll speed (blue). Phase is head speed relative to inspiration onset times. The calculation was done on 3 s segments during which the sniffing frequency was between 4 Hz and 8 Hz for a majority of the segment. Calculation performed with data from 3 animals.

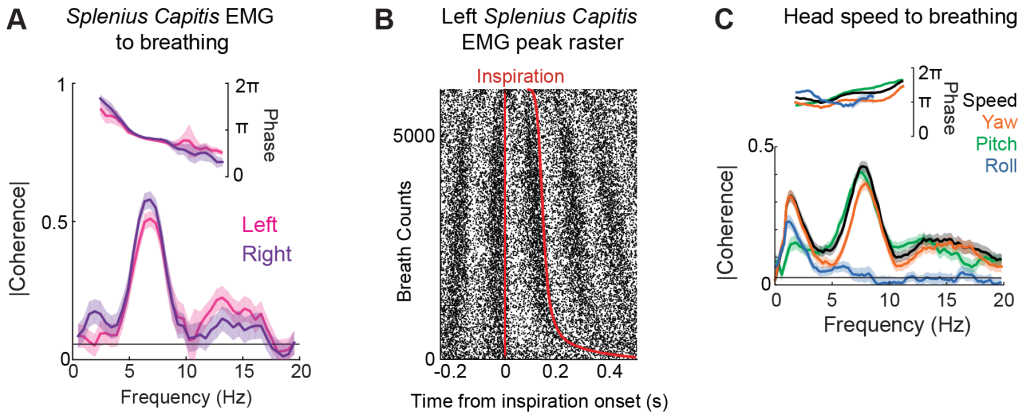

Figure 3.24: Hall-effect probe calibration. Calibration between Hall-effect probe outputs and nose position from videography data in the head-restrained condition, example traces show lateral nose position (blue), vertical nose position (black), left hall probe output (purple), right hall probe output (orange).Correlation scatterplot of hall probe outputs to lateral and vertical nose position. Left (purple) hall probe is correlated with lateral position, while right (orange) is anti-correlated. Both outputs are anti-correlated with vertical position.

movements during sniffing and that motion of the nose precedes that of the head.

The relative coordination among sniffing, nose motion, head bobbing, and whisking is summarized in a phase diagram (Figure 3.21). The maximum vertical deflection of the nose and the maximum lateral deflection of the nose, to either side, occur during inspiration (Figure 3.4), defined as the phase interval 0 to p radians. The tilt of the head, found by integrating the angular velocity in the direction of pitch (Figure 3.19C), also reaches a peak during inspiration. Lastly, the protraction phase of whisking coincides with inspiration (Figure 3.11). In toto, inspiration coordinates the orofacial motion that is used to sample a region of the peripersonal space that surrounds the ratâĂŹs head.

3.3 Discussion

Our work establishes a scenario in which orofacial motor actions are choreographed relative to the sniff cycle, such that the onset of inspiration is coincident with a 'snapshot' exploratory sampling (Figure 3.21). In particular, we found rhythmic motion of the nose (Figures

3.4 and 3.11), as well as rhythmic motion of the head (Figure 3.19), i.e., bobbing, as the rodent cranes, are coordinated with sniffing through their respective muscular drive.

The maximum upward deflection of the nose and head, as well as the protraction of the vibrissae, occur concurrent with inspiration (Figure 3.21). Thus inspiration corresponds to a period of multisensory sampling of the environment. Head bobbing and nose movement result in re-orientation of the head and nose during the expiratory phase of sniffing, so that the rodent can sample a new region of peripersonal space during the subsequent inspiratory phase. These data build on past findings on the coordination of whisking with sniffing [74, 23, 82] and expand beyond qualitative observations on bodily motion associated with sniffing [106]. Further, we show that a slow bias in the movement of the nose occurs during sniffing and that the nose orients toward odors (Figure 3.13). The *d. nasi* muscles contract synergistically to pull the nose laterally and upward and coordinate with breathing to cause the nose position to peak during inspiration (Figure 3.9). Our results, together with past data on the resetting of the whisking rhythm by breathing [74, 23, 82], imply that respiratory circuits in the brainstem [89, 35, 28] act as a master oscillator to phase-lock rhythmic orofacial motor actions. What might be the utility of coordinating the fast, rhythmic motion of the different sensory apparatuses as animals explore their nearby environment? It is an open issue whether the coordination of these motor actions maximizes sensory input [61, 60], such as by sweeping odorants toward the nose.

Any source of sensory input that contributes to both touch and olfaction, which are elements of social interactions [65] as well as exploration (Figure 3.21), will lead to multisensory input that is likely to be phase-locked to breathing. The temporal regularity of the signals can improve the fidelity of coding of the stimuli. The same argument holds for deflection of the vibrissae by wind and olfaction [110]. The issue of temporally synchronized signals issue might be potentially addressed by recordings from multisensory areas [60] using a rodent in a virtual environment [90]. The present work is focused on coordination of sensory input from proximal sources. How does this compare with coordination of input from distant sources, as detected by

visual and acoustic disturbances? Saccadic eye movements and pinna movements, for example, are temporally coordinated with each other and serve to orient to a stimulus of either modality [13, 7, 77]. During coordinated eye-head movements in primates, the eye leads the head by 25 to 40 ms [7], similar to the latency between nose and head movements in rodents. The need to reorient the head relative to the lighter and thus faster moving vibrissae, nose, and eyes thus appears to lead to similar phase-shifts for sensing of near as well as distant spatial scales.

What role might orientation of the nose play in olfactory perception? It has been environment shown that rats are able to quickly distinguish small differences in the lateral position of olfactory inputs [81] and are impaired on tracking and odor localization tasks when a nostril is blocked [57, 16]. This evidence suggests that even small air flow differences between nostrils, as might be generated by nose movement [21], could aid in odor tracking and source localization. While we have recently described the premotor circuitry or whisking and breathing [74, 23], the corresponding circuitry that supports the orientation and net deflection of other orofacial sensory organs during exploration remains to be delineated. For the present case of the nose, this circuitry presumably involves ascending input via the accessory olfactory nucleus [58]

3.4 Methods

3.4.1 Subjects

Our data were collected from 25 Long Evans adult female rats, 250 to 350 g in mass. All experimental procedures on our animals were accordance with Guide for the Care and Use of Laboratory Animals and have been approved by Institutional Animal Care and Use Committee at University of California, San Diego.

3.4.2 Surgery

All surgeries were performed under ketamine (90 mg/kg rat mass) and xylazine (10mg/kg rat mass) anesthesia. Injections were made intraperitoneally with supplemental injections of ketamine (20mg/kg rat mass) given as needed. Buprenorephine, an analgesic agent, was administered after the surgery (20 μl). Video monitoring of nose and vibrissa position. Six Long Evans rats were implanted with a head post [6] and a K-type thermocouple (5TC-TT-K-36-36, Omega Engineering) in the nasal cavity [102]. Of these, one rat was implanted with two thermocouples, one in each nasal cavity. Rats were habituated to the head fixation rig after recovery as judged by normal grooming and whisking and a complete lack of struggling.

A high speed video camera (Basler A602f) was used to record nose and vibrissa motion at a rate of 216fps, and spatial resolution of at least 170μm. A 45 degree mirror installed below the rat enabled tracking in all planes of motion. The tip of the nose and the C2 vibrissa on each side were marked using fabric paint (Tulip dimensional fabric paint, 65101) for tracking. To illuminate the rat for video, an 850nm LED illuminator was used (Yr.seasons 48-LED Illuminator Light CCTV). Tracking was performed with custom software in Matlab either in real time, for just lateral and vertical movement of the nose, or post hoc from 60s video segments for nose movement in three dimensions plus vibrissa tracking.

First, we describe the distribution of nose positions in a head-restrained rat.

Figure 3.1 shows a diagram of the setup for monitoring head-restrained nose motion and respiration. Tracking of the vibrissae was performed as in past work [23, 74]. The midpoint of whisking was calculated as the average of the rostral and caudal extrema in the position of the vibrissae. We measure and report nose position in length, i.e., millimeters. However, since air flow around the nostrils in rats is directed laterally [107], lateral movement of the nose could also be interpreted as a change in angle between the nostrils. Thus we show a conversion to estimated angle for lateral motion (Figure 3.3C), with angle determined by manually marking the line between the nostrils in video frames. We fit a tangent function to the data to estimate the

effective fulcrum, which we find to be 7.8 $\pm$ 0.4 mm caudal to the tip of the nose.

3.4.3 EMG recording

Thirteen rats were implanted with pairs of microwires in specific musculature and a thermocouple in the nasal cavity. The targeted muscles were the left and right d.nasi in five rats; the leftd. nasionly in one rat; the left and right *d. nasi* and the nasolabialis muscle in two rats; the left d.nasi and the left nasolabialis in two rats; and the left and right splenius capitis in three rats.

Additionally, in three of the rats with microwires in d. nasi, microwires were also inserted acutely to target the intrinsic muscles of the pad immediately prior to a recording session. For chronically implanted EMG recordings, 50 μm diameter perfluoroalkoxy insulated tungsten wire (AM systems 795500) was stripped 2-3mm to form recording electrodes, and a 125μm diameter PFA insulated tungsten wire (AM systems 796500) was stripped 4-5mm for the reference electrode. Each wire was hooked and threaded through a 30 gauge needle. For measurements from d.nasi, a n incision was made along the snout and the muscles exposed through a careful dissection of the overlying skin and fascia. Two or three recording electrodes were implanted in each muscle, and the reference electrode was placed along the snout. For measurements from splenius capitis, an incision was made along the midline in the back of the neck and the muscles exposed through a careful dissection of the overlying skin and fascia. Two recording electrodes were implanted in each muscle, and the reference electrode was placed below the scalp. In all cases, the wires were soldered to a custom board that was placed alongside the head plate and covered in Orthodontic Acrylic Resin (Ortho-Jet liquid and crystal powder, Lang Dental Manufacturing) to form a chronic implant. The EMG signals were acquired using a custom built amplifier [33]. For the final measurement, the difference between the two spatially separated signals was formed, band pass filtered at between 300Hz and 10kHz with a zero-phase Butterworthfilter, rectified, and finally low pass filtered at 50Hz with a zero-phase Butterworth filter to extract the envelope of the muscle activity. For acute recording of mystacial EMGs,

electrodes were prepared as for the chronic measurements. Rats were anesthetized with 3% (v/v) isoflurane in 5% (v/v) oxygen, and recording electrodes were placed in the center of the C row by inserting the needle with the hooked electrode caudally to the pad and threading it to the desired location. The needles were then removed and the rats allowed to wake. The implant procedure took approximately two minutes. These EMG signals were acquired using a DAM 80 (World Precision Instruments) differential amplifier with the reference as ground.

3.4.4 Olfactory stimulation

We quantified nose motion in response to the controlled delivery of fumes from bedding of the home cage [33, 79](Figure 3.16) alternately to the left or right nostril (Figures 3.13,3.14). The deflection of the nose, along with the activation of the d.nasi muscles, was recorded in sessions that lasted no more than 30 minutes to minimize the effects of adaptation of behavior to the odorant.

A custom solenoid stimulator that flows air continuously to the nostrils, such that the air pressure does not change at the time of odor presentation, was constructed (Figure 3.13A). Figure 3.15 shows the calibration for the timing of the stimulator, reconfigured to deliver a puff of air, and a calibration for pressure change using a piezoelectric input, to show that air pressure does not change when odor is delivered. Odors are presented alternately to the left or right side at an interval between 25 and 250s.

To block a nostril, we fill the naris with a minimal amount of silicone polymer. As confirmation that the nostril is blocked completely by this method, we compare breathing signals on the left and right side in a rat in which thermocouples are implanted in contralateral versus ipsilateral airways. We find that blocking one side completely abolished the breathing signal on that side (Figure 3.18). In our subsequent analysis of trials, we exclude epochs where the rat is not following a normal breathing pattern, but rather chattering.

3.4.5 Gyrometer measurements.

Three rats were implanted with a thermocouple and a mount for micro-electro-mechanical systems (MEMS) gyrometer sensors at least 2 days prior to behavioral testing. Immediately prior to behavioral testing the rats were manually restrained and connected to the MEMS gyrometer sensors, i.e., yaw (LISY300ALST; Microelectronics) and pitch and roll (IDG-500; Invensens),and a miniature thermocouple pre-amplifier.

Leads for both instruments were passed through a commutator [33], amplified and low-pass filtered at 40Hz. Rats were placed on a small, raised platform upon which where they were allowed to move and explore freely. They were periodically coaxed to sniff and whisk by presenting olfactory stimuli including the rat's home cage, bedding of another rat, or other odors [33, 51]. The position of the rats was recorded simultaneously via an overhead webcam. Magnetic sensor measurements. At least 2 days prior to behavioral monitoring, the rats were surgically implanted with a head restraint plate, a mount for a MEMS gyrometer, and two 4-40 screws atop the nasal bone as a mount for a custom-made, dual Hall-effect probe (no.A1389; Allegro Microsystems). Additionally, a small magnet, 2 to 5mg in mass, was inserted into the nasal cartilage via an incision in the skin overlying the nasal bone. Prior to each behavioral session the rats were head restrained, the inertial sensor was mounted, and the Hall-effect probe was secured in place by affixing to the 4-40 screws with sandwiching nuts. While still head-restrained, the rats were coaxed to sniff, and nose position was monitored via high speed videography and via the magnetic sensors to verify placement of the magnet and that the output of the magnetic sensors reported nose position (Figure 3.24).

3.4.6 Data Analysis

All routines were written in Matlab (The Mathworks) or Python. For spectra and coherence we used the Chronux routines [8]. We confined our correlation and coherence analysis to sniffing

and basal breathing bouts of 3s or more. We define the onset of an inspiration to be the rise time at which the amplitude of the signal reached 0.1-tmes the peak amplitude 3.24. We identified positive and negative directions of lateral nose motion when the amplitude of the motion exceeded 0.5mm beyond the central position. For both lateral and vertical nose position, trials were split into left versus right motions and up versus down motion, respectively, to allow for averaging

3.5 Author contributions

Chapter 3, in full, is a reprint of material that is currently published in: A. Kurnikova*, J. D. Moore*, S.-M. Liao, M. DeschÃłnes, D. Kleinfeld., ”Coordination of orofacial motor actions into exploratory behavior by rat”, *Current Biology*, 2017. The dissertation author was the primary investigator and author of this manuscript. This material is included in Chapter 3 with the generous consent of all coauthors.

Chapter 4

Circuitry of nose movement

4.1 Abstract

Rodents shift their nose from side to side when they actively explore. This motor action might be used to sample and lateralize odors efficiently in the space. Lateral motion of the nose is correlated to breathing, and occurs both spontaneously during sniffing and in response to an odorant presentation. We study the premotor control of nose motion in order to further our understanding of generation of orofacial exploratory behaviors in coordination with the respiratory drive. We use replication competent rabies virus to transsynaptically label inputs to the *deflector nasi* muscle in order to identify putative premotor inputs that control motion of the nose. We find two core clusters secondary labeled cells: one in the reticular formation caudal to the facial motor nucleus (nose retrofacial area) and another in the caudal part of the IRt/Gi border (nose IRt), near the vibrissa oscillator. In addition, we find putative premotor labeling throughout the brainstem reticular formations, trigeminal nuclei, pontine reticular formations, midbrain reticular formation, red nucleus and superior colliculus. Functionally, we find that ablation of cells in the nose retrofacial area, but not the nose caudal IRt impairs the response of the nose to presented odors. Optogenetically activating the glutamatergic cells in both the nose

retrofacial and nose IRt drives deflection of the nose. Altogether, we have identified a novel circuit for driving nose motion in rodents. This work lays the groundwork for investigating olfactory to brainstem pathway for nose motion control and breathing-related control of nose motion.

4.2 Significance statement

We have studied a novel circuit for control of nose motion, and confirmed the functional role of two brainstem premotor areas in eliciting nose movement. This work identifies a circuit structure common to other orofacial motor actions and their control relative to the breathing signal.

4.3 Introduction

Movement of the nose is a surprisingly multi-faceted behavior that is controlled by a single muscle - the *deflector nasi* [20, 64]. The nose moves both rhythmically with breathing, and produces slow deflections such as orienting towards an odor [64, 26]. The slow, orienting, movements of the nose might play a role in olfactory localization, as lateral deflections affect air flow between sides of the nasal cavity [21]. Synchronization of movement on a breath-by-breath cycle is seen in many types orofacial movement and may play a role in binding multimodal sensory inputs. Nose movement can be evoked by micro-stimulation in the motor cortex [10, 71]. Lesions in the AON - an area of the olfactory bulb that compares odor inputs between two sides [58] have been found to disrupt nose orienting towards an odor [26]. However, the downstream (brainstem) motor circuit responsible for these behaviors, and its candidate anatomical connections to the motor and olfactory systems have not been identified.

Past work on orofacial and respiratory circuits in the medulla has pointed to the hypothesis that orofacial movement is linked to breathing via a signal from the PreBötzinger complex to

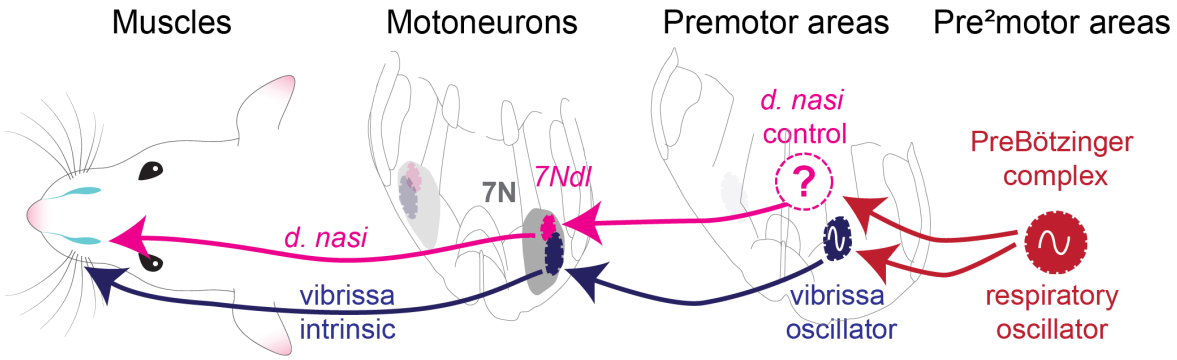

Figure 4.1: Diagram of hypothesized circuit for control of nose motions via the *deflector nasi* (magenta), and known circuit for vibrissa motor control (blue). Motoneurons in the facial motor nucleus send projections to the muscles and receive inputs from premotor areas. Premotor areas receive inputs from the prebotzinger complex to drive synchronization to breathing. We aim to identify putative premotor areas for the *deflector nasi*.

a pre-motor area [99, 61, 19]. Thus a circuit motif might involve a premotor area that drives motor neurons in the facial motor nucleus, and receives input from the PreBötzinger complex that drives the synchronization of movement to breathing (Figure4.1). Olfactory processing is highly affected by its synchronization to breathing [88, 86], yet its large-distance connections to the brainstem areas are not well understood. Thus nose movement, a behavior linked to both olfactory processing and respiratory control is a particularly interesting case study in how long range circuits might be structured. Here we use retrograde tracing using rabies virus to identify two pre-motor areas that control movement of the nose - an area caudal to the facial motor nucleus that we call the 'retrofacial area', and an area near the vibrissa IRt oscillator that we call the 'nose IRt'. We confirm functional relevance of the identified areas by showing that stimulation evokes nose movement, while ablation affects movement to the lesioned side.

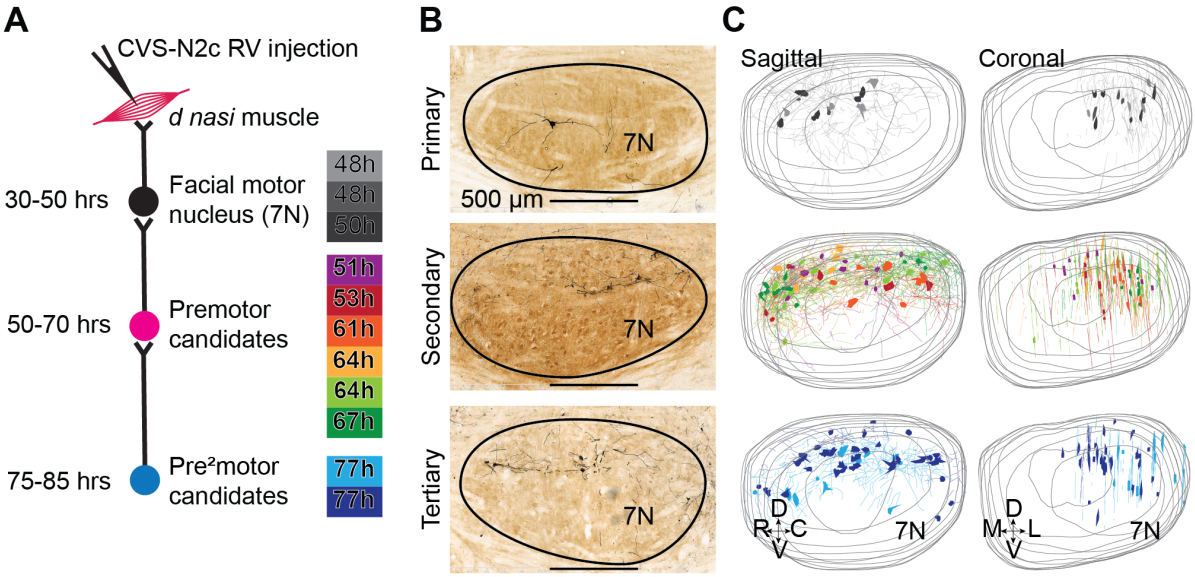

Figure 4.2: Retrograde tracing from the *deflector nasi* (A) Diagram of the experimental procedure. The *deflector nasi* was injected with N2c replication competent rabies virus, and rats were perfused at primary, secondary or tertiary timepoints. (B) Examples of labeling in the facial motor nucleus (7N) at primary, secondary and tertiary timepoints. Motoneurons remain intact at all timepoints. (C) Reconstructions of labeled motoneurons and motoneuron dendrites in the facial motor nucleus. Cell bodies and dendritic fields were found in the dorsolateral part of 7N. Colors correspond to individual timepoints. Top shows primary labelled timepoints (greyscale). Middle shows secondary labeled timepoints (red-green). Bottom shows tertiary labeled timepoints (blues).

4.4 Results

4.4.1 Tracing with rabies virus

We identified putative premotor and pre^{2}motor areas for nose motion by retrograde tracing using replication competent rabies virus from the *deflector nasi* muscle (Figure 4.2A). At all timepoints, cells in the facial motor nucleus appeared intact (Figure 4.2B). In addition, motor neurons and their dendritic fields were found in the dorso-lateral portion of the facial motor nucleus (7Ndl) (Fig 4.2C) which is consistent with previously reported location of motoneurons for the *deflector nasi* [23]. Thus we are confident that all observed labeling is from the injected muscle, with no contamination from virus spillover.

4.4.2 Key premotor areas for the *deflector nasi*

To identify the locations of the most prominent premotor labeling across rats, we reconstructed all brains and created a reference atlas [17] (Figure 4.4, Figure 4.5). We then aligned all brains to the common reference atlas and determined locations of highest labeled cell density in each brain. Figure 4.3A shows an example of labeled cells in an area just caudal to the facial motor nucleus (RF), while figure Figure 4.3C shows an example of labelling in a more caudal region (nIRT), near the location of the vibrissa IRt [74]. Reconstructions of all animals show consistent labeling in each of these two regions across all rats at the secondary timepoint. A subset of four of six rats have high density labeling in the retrofacial region, as revealed by overlapping reconstructed cells and 10% density contours (Figure 4.3B, Figure4.6A-C) A different subset of four of six rats have high density labeling in the nIRT region (Figure 4.3D, Figure 4.6D-F). In summary we find a stretch of labeling in the medulla on the border of IRt and Gi that has high density labeling amongst at least four of six labeled rats. We calculate a gaussian mixture model fit to the high density labeled area across all rats, and determine that minimum in the Bayesian information criterion and Aikake information criterion occur at two components (Figure 4.8A).

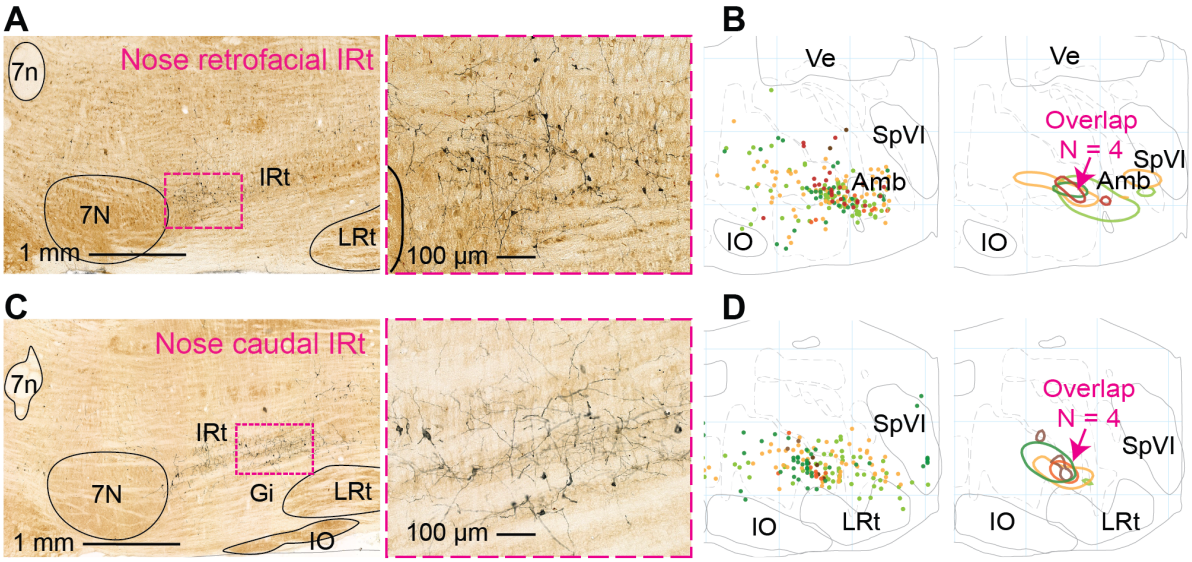

Figure 4.3: Key premotor areas identified by retrograde tracing from the *deflector nasi* (A) Example of premotor labeling in the retrofacial area at a 64 hrs timepoint in a sagittal section approximately 1.7 mm lateral of midline. Labeled cells are revealed in dark product, while structures are identified in a CO stain. (B) Reconstructions of premotor labeling in the retrofacial (RF) area in six rats at secondary-labeled timepoints. Left panel shows reconstructions of labeled cells in a 200 um thick coronal slice at 10.7 mm caudal of bregma. Right panel shows 10% maximum density contours in the same coronal slice. Secondary timepoints shown are: 51 hrs (Purple), 53 hrs (red), 61 hrs (orange), 64 hrs (yellow), 64 hrs (light green), 67 hrs (green). Four of six contours - 53 hrs, 64 hrs, 64 hrs, 67 hrs - overlap in the retrofacial area (RF). (C) Example of premotor labeling in the nIRt area at a 64 hrs timepoint approximately 1.5 mm lateral of midline. Labeled cells are revealed in dark product, while structures are identified in a CO stain. (D) Reconstructions of premotor labeling in the caudal IRt/Gi area in six rats at secondary-labeled timepoints. Left panel shows reconstructions of labeled cells in a 200 um thick coronal slice at 11.5 mm caudal of bregma. Right panel shows 10% maximum density contours in the same coronal slice. Secondary timepoints shown are: 51 hrs (Purple), 53 hrs (red), 61 hrs (orange), 64 hrs (yellow), 64 hrs (light green), 67 hrs (green). Four of six contours overlap - 51 hrs, 61 hrs, 64 hrs, 67 hrs - in the caudal IRt/Gi area (nIRt).

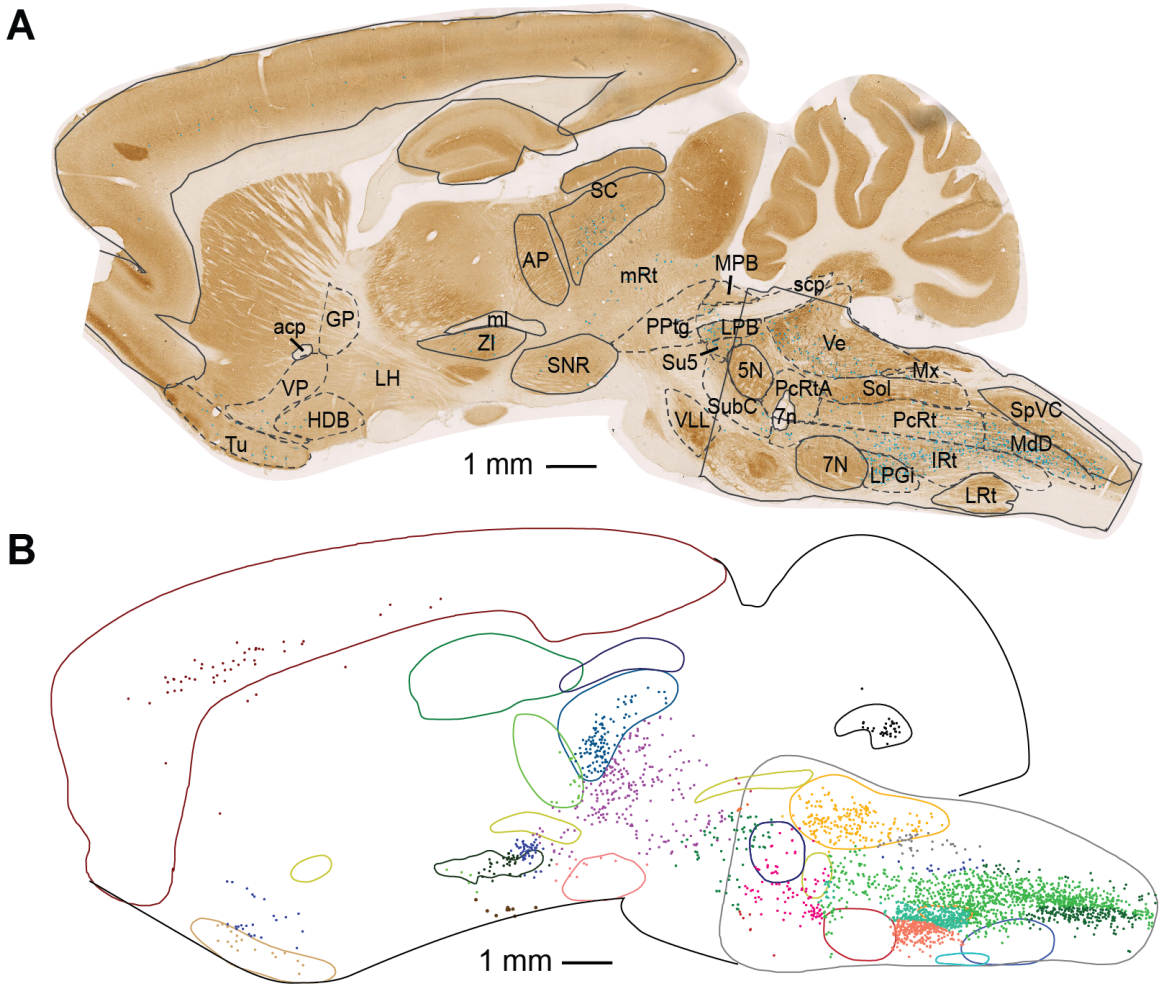

Figure 4.4: Example tracing for cell count (A) Example section with annotated areas and cells. Areas annotated based on CO stain (solid lines) and estimated based on known landmarks (dotted lines) (B) Example cell assignation to labeled areas for cell count.

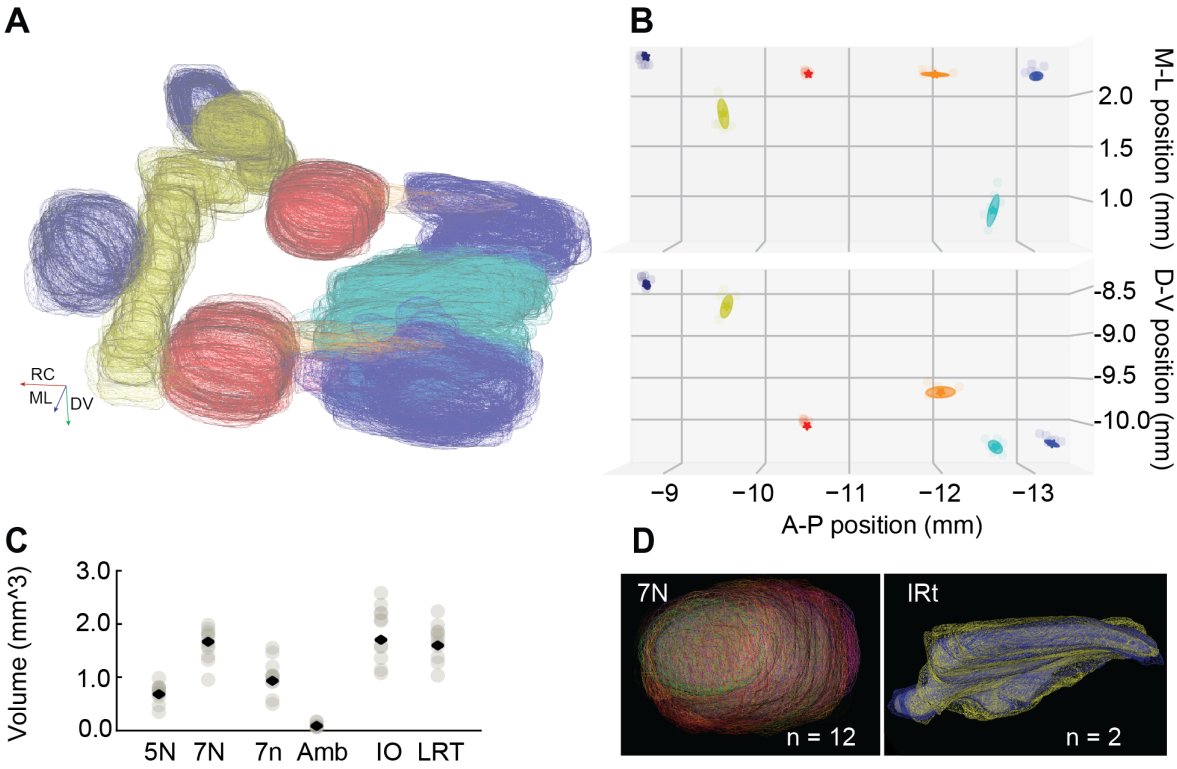

Figure 4.5: Construction of rat atlas for cell count (A) Example alignment of all structures used for alignment in six annotated volumes. (B) Structure centroids and covariance ellipsoids used in creating the rat averaged atlas. Top view (top) and sagittal view (bottom) are displayed. (C) Individual structure volumes (grey) and averaged structure volume (black) for the alignment structured. (D) Example of alignment by structure, used to create atlas volumes. Facial motor nucleus (7N) n = 12 instances for averaging and IRt -n = 2 instances - are shown

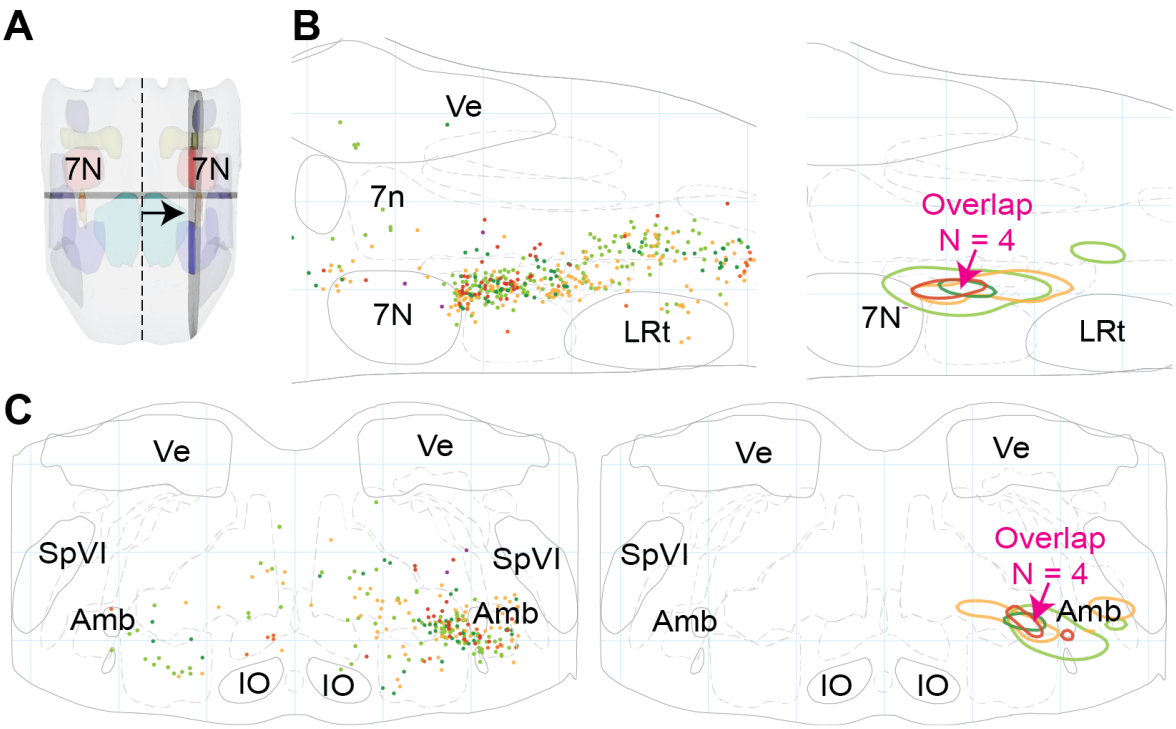

Figure 4.6: Premotor labeling in the retrofacial area (A) A top view of a 3D diagram shows the locations of selected slices through the reconstruction for the retrofacial area. (B) 200 um thick sagittal slices through reconstructions of premotor labeling in the retrofacial area in six rats at secondary-labeled timepoints. Reconstructions of labeled cells (left) and 10% maximum density contours (right) are shown. (C) 200 um thick coronal slices through reconstructions of premotor labeling in the retrofacial area in six rats at secondary-labeled timepoints. Reconstructions of labeled cells (left) and 10% maximum density contours (right) are shown.

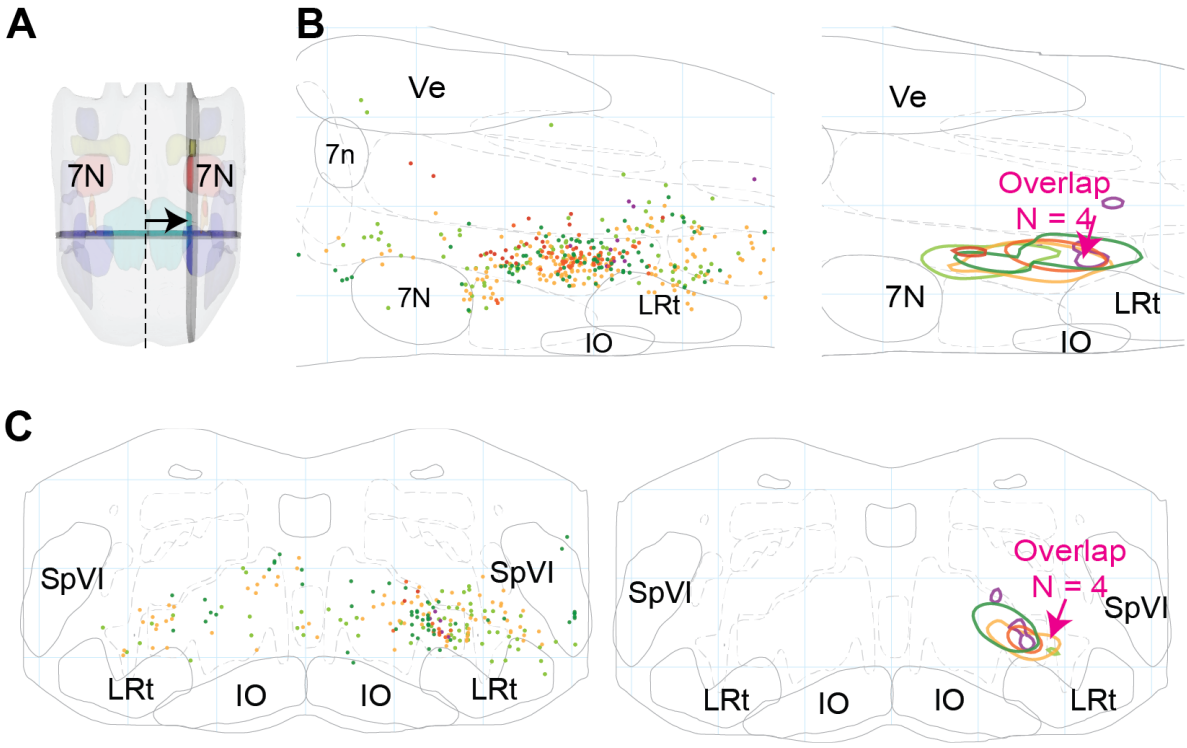

Figure 4.7: Premotor labeling in the nIRT area (D) A top view of a 3D diagram shows the locations of selected slices through the reconstruction for the nIRT area. (E) 200 μm thick sagittal slices through reconstructions of premotor labeling in the nIRT area in six rats at secondary-labeled timepoints. Reconstructions of labeled cells (left) and 10% maximum density contours (right) are shown. (F) 200 μm thick coronal slices through reconstructions of premotor labeling in the retrofacial area in six rats at secondary-labeled timepoints. Reconstructions of labeled cells (left) and 10% maximum density contours (right) are shown.

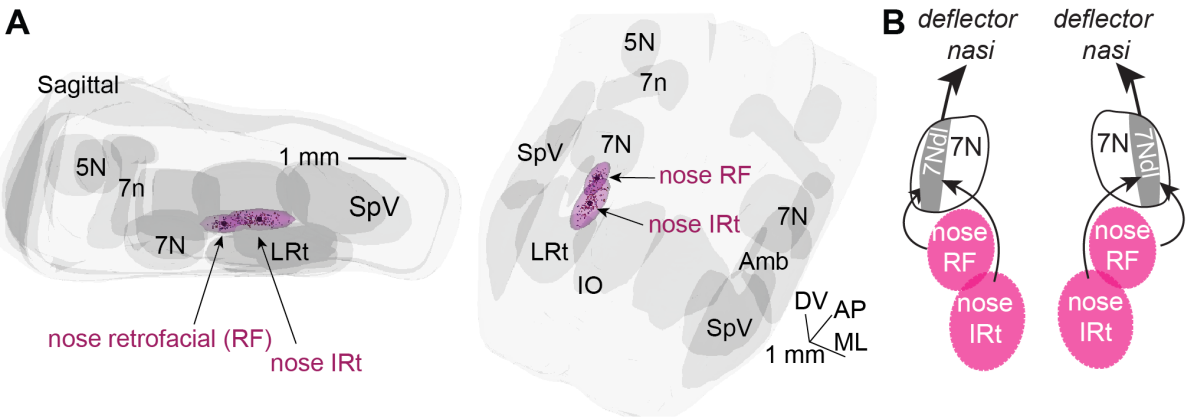

Figure 4.8: Quantitative identification of putative nose premotor areas (A) 3D display of a 2-component gaussian mixture model fit to the high density labeled area in six rats. Reconstructed cells are shown as small spheres. Centroids of the two labeled areas are shown as large black spheres. 3-sigma radius ellipsoids are shown in magenta. Two areas emerge from the fit: a more rostral area which we call the nose retrofacial (RF) area and a more caudal nose area on the border of Gi and IRT which we call the nose IRT area. 45 degree (left) and sagittal (right) projections of the data are displayed. (B) Diagram of proposed nose motion circuit based on the results of premotor labeling from the *deflector nasi* muscle. Motoneurons located in the dorsolateral facial motor nucleus (7Ndl) send projections to the ipsilateral *deflector nasi* muscle, and receive input from the ipsilateral RF and nIRT premotor areas.

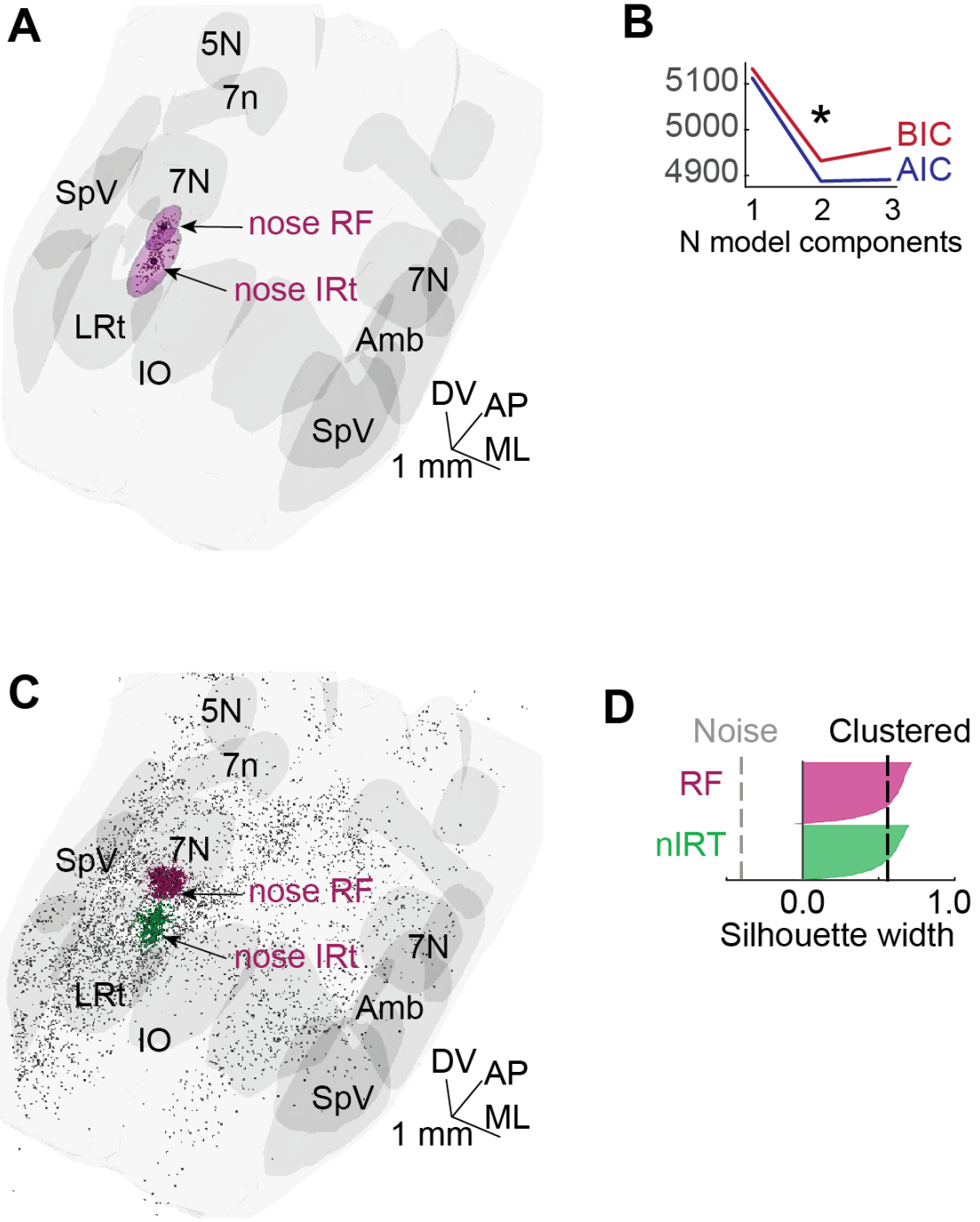

Figure 4.9: Comparison of quantitative identification of putative nose premotor areas (A) 3D display of a 2-component gaussian mixture model fit to the high density labeled area in six rats. Reconstructed cells are shown as small spheres. Centroids of the two labeled areas are shown as large black spheres. 3-sigma radius ellipsoids are shown in magenta. Two areas emerge from the fit: a more rostral area which we call the nose retrofacial (RF) area and a more caudal nose area on the border of Gi and IRT which we call the nose IRT area. Centroids are located at (-10.7 mm RC; 1.7 mm ML, 7.8 mm DV) for the retrofacial area and at (-11.5 mm RC; 1.5 mm ML, 7.7 mm DV) for the nIRT. 45 degree projections of the data are displayed. (B) Bayesian information criterion (blue) and aikake information criterion (red) analysis for model selection. Both metrics have a minimum value at 2 components. (C) 3D display of a DBSCAN clustering of the labeled cells in six rats. Parameters for the clustering are N = 50, and = 200 μm. Reconstructed cells

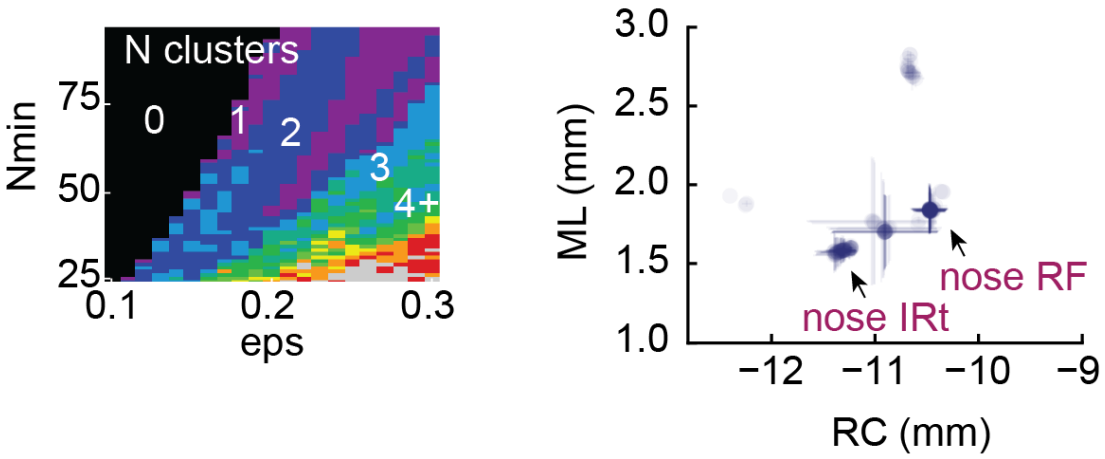

Figure 4.10: Parameter selection for DBSCAN clustering. (right) number of clusters by values in parameter space. (left) location of cluster centroids for clustering with 2 components. For a a two cluster pattern, the retrofacial and nIRT are the dominant clustering pattern centroids.

Thus we conclude that the labeled premotor areas can best be described as two loci of high density labeling, corresponding to a two component model. The two overlapping areas are entered on the coordinates: (-10.7 mm, 1.7 mm, -7.8 mm) for the nose retrofacial area (RF) and (-11.5 mm, 1.5 mm, -7.7 mm) for the nIRT. When scaled to mice, these coordinates are (-6.9 mm, 1.0 mm, -5.4 mm) nose retrofacial area and (-7.3 mm, 0.9 mm, -5.1 mm) for the nIRT. To confirm the labeling centroids, we repeated the clustering analysis using a point-by-point density based clustering - dbscan [27]. We find that a broad region of parameter space yields 2 clusters in the labeling (Figure 4.10). At the biologically plausible parameters eps = 200 um and 50 points we obtain clusters centered at (-10.5 mm, 1.8 mm, 7.9 mm) and (-11.4 mm 7.7mm 1.6 mm (Figure 4.10, 4.9), close to the clustering obtained by the gaussian mixture model.

While not all traced animals had labeling in each of the two key areas, the emergence of the labeling is not a matter of later timepoints. Critically, of the two earliest timepoints in which labeling was very sparse, the 53 hr timepoint showed labeling in the nose - retrofacial area, while the 51 hr timepoint showed labeling in the nose IRt. We conclude that both of the nose retrofacial

and nose IRt are likely to be premotor areas, although it is possible that they project to disparate subsets of motoneurons in the facial motor nucleus (Figure 4.8B).

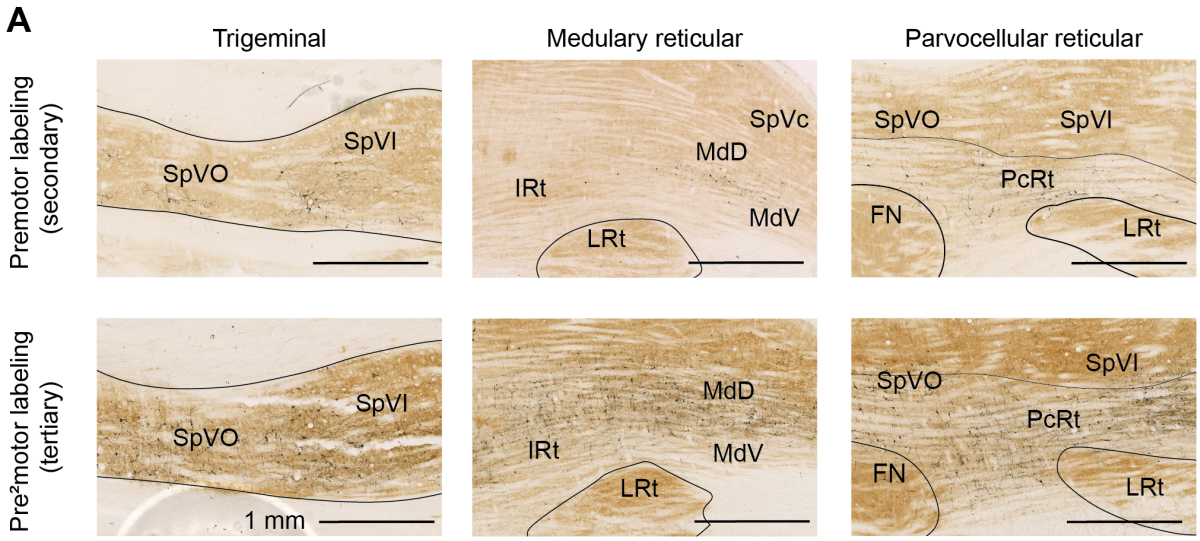

Figure 4.11: Examples of labeled putative premotor areas at secondary (upper row) and putative preÂšmotor areas at tertiary (lower row) timepoints. Left: labeling in the ipsilateral trigeminal nuclei is most dense in the dorsal part of SpVO and SpVI. Center: Labelling in the parvocellular reticular nucleus. Right: Labeling in the medullary reticular nuclei. Labeling density increases at the tertiary timepoints, suggesting additional circuits involved in pre^{2}motor control. Structures outlined from CO stain, rabies labeled cells revealed in dark product. Center and right panels are misplaced with respect to the text.

4.4.3 Retrograde labeling in the hindbrain

Labeling from the *deflector nasi* was found in multiple areas of the medulla at both secondary and tertiary timepoints. At secondary timepoints brainstem reticular formation had dense ipsilateral labeling in the parvocellular (PCRt), gigantocellular (Gi), intermediate (IRt), and dorsal (MdD) and ventral (MdV) medullary subdivisions, as well as weaker contralateral labeling in all these areas. At tertiary timepoints, both ipsilateral and contralateral labeling increased dramatically ((Figure 4.11), Figure 4.12A). The trigeminal nuclei also had ipsilateral labelling at secondary timepoints, most noteably in the ventral parts of spinal trigeminal nuclei interpolaris (SpVI) and oralis (SpVO). Some animals at the secondary timepoints also showed labelling in

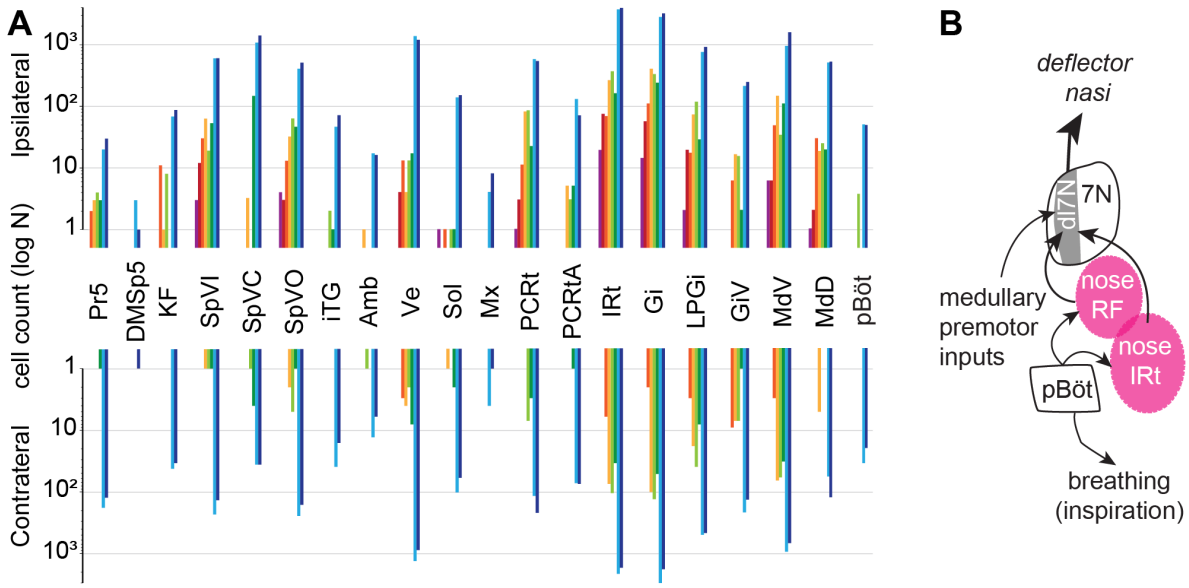

Figure 4.12: Medullary labling from the *deflector nasi* (A) Bar chart of labeled cell count (log scale) in the medulla. Ipsilateral (top) and contralateral (bottom) are shown. No labeling outside of the facial motor nucleus is observed at the primary timepoints. Labeling across all areas inclreases dramatically at the tertiary timepoints (77 hrs) (B) Proposed circuit for control of nose motion. Motoneurons in the dorso-lateral facial nucleus (7Ndl) send input to the *deflector nasi*, and receive input from premotor areas. We hypothesize that premotor areas nose-RF and nose-IRt receive respiratory input from the PreBötzinger complex.

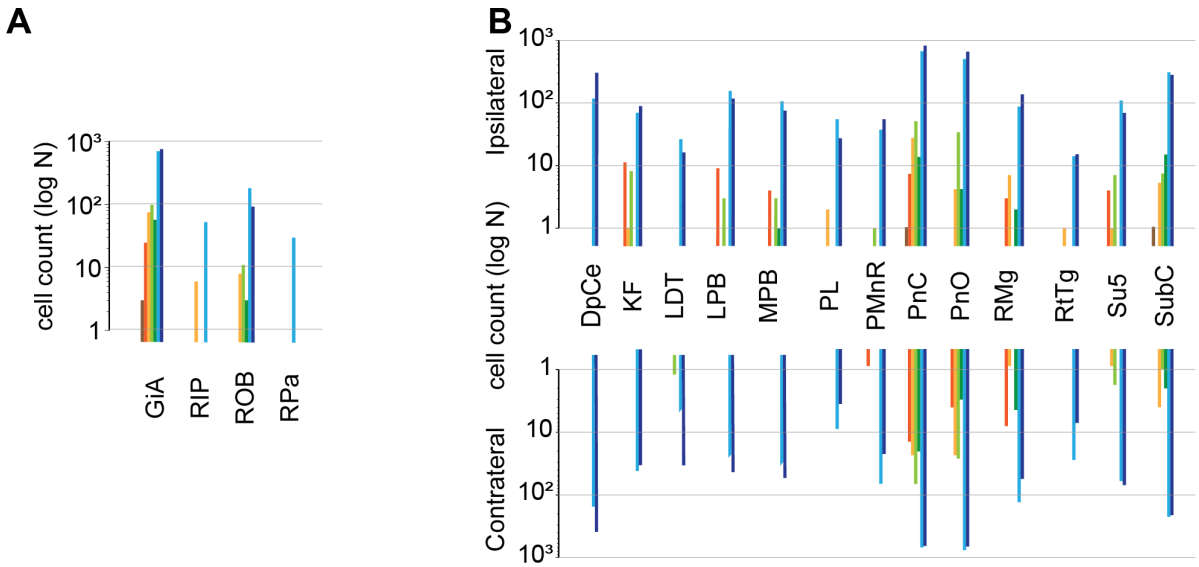

Figure 4.13: Cell counts in the hindbrain (A) Cell count of all labeled cell bodies in singular structures in the medulla. (B) Cell counts in ipsilateral (top) and contralateral (bottom) in the hindbrain. by timepoint. Number of labeled cells increases dramatically at the tertiary timepoints. Data obtained from all datasets aligned to the atlas as defined in Figure 4.5. Figure 4.4 provides an example of cells in a single section assigned to atlas areas.

caudalis (SpVC) as well as sparse labelling in Kölliker-Fuse and the supratrigeminal nucleus (Su5). At tertiary timepoints, the trigeminal nuclei were densely labeled both ipsilaterally and contralaterally (Figure 4.11).

In the metencephalon, we observe sparse premotor labelling bilaterally in the pontine reticular formation oralis (PnO) and caudalis (PnC), as well as subcoeruleus nucleus (SubC), and sparse labelling in the Kölliker-Fuse nucleus (KF). At tertiary timepoints, labelling density increased throughout the PnO, PnC, SubC and KF. In addition, dense labelling was observed bilaterally in the deep cerebellar nuclei, the lateral and medial parabrachial nuclei, the pedunculo-pontine tegmental nucleus and intertrigeminal nucleus (iTG) (Figure 4.15, Figure 4.16).

In the PreBötzinger complex we observe no labeling at the secondary timepoints, and dense labeling at tertiary timepoint (Figure 4.14). This pattern of labeling is consistent with the circuit hypothesis that the PreBötzinger complex provides inputs to a variety of premotor areas to

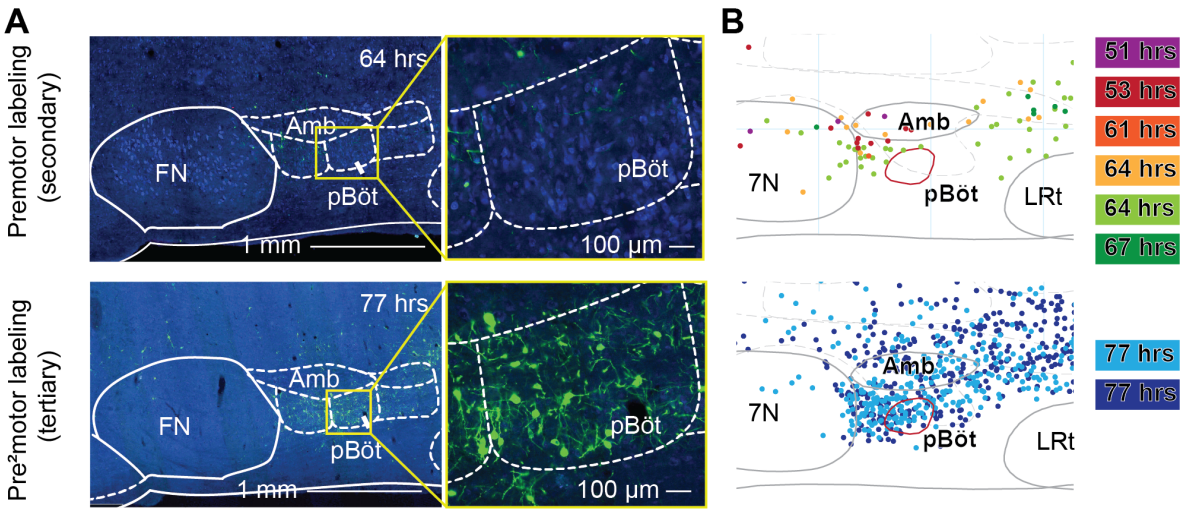

Figure 4.14: Pre^{2}motor, not premotor labeling in PreBötzinger complex (A) Example sections showing no labeling in PreBötzinger complex at secondary timepoint (64 hours), and dense labeling at tertiary timepoint (77 hours). Cells are stained with Neurotrace Blue, and rabies labeled cells are revealed in green. Structures are annotated from Paxinos atlas. (B) 200 um thick sections from reconstructions of premotor (secondary) and pre^{2}motor (tertiary) labelling in the PreBötzinger complex (red). Location of PreBötzinger complex identified from somatostatin stain. No labeling is observed at secondary timepoints, while dense labeling is seen at tertiary timepoints.

drive orofacial motion coordination to breathing. Based on their locations, both the retrofacial and caudal IRt are likely candidates to receive input from the PreBötzinger complex [99].

Figure 4.12B summarizes this hypothesis of the circuit for nose motion control. We propose that the nose retrofacial and nose IRt provide premotor input to the facial motor nucleus, and receive input from the PreBötzinger complex to produce the nose synchronization to breathing.

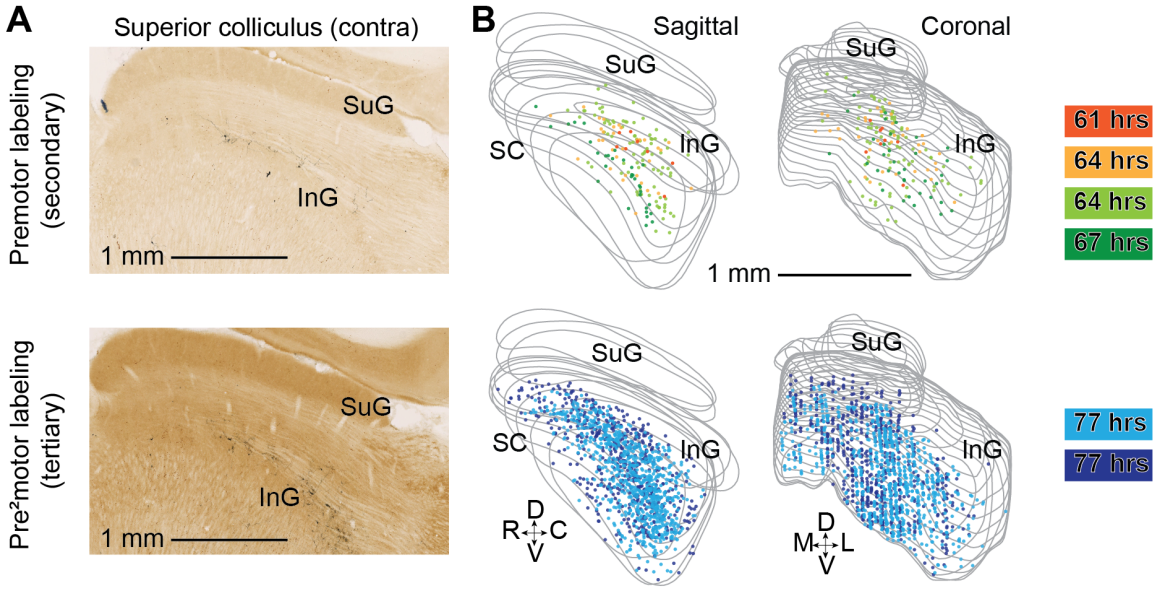

Figure 4.15: Labeling in the superior colliculus (A) Example labeling in the superior colliculus at secondary (top) and tertiary (bottom) timepoints. (B) Reconstructions of superior colliculus labeling at secondary (upper row) and tertiary (lower row) timepoints in sagittal and coronal views.

4.4.4 Retrograde labeling in the midbrain

We find premotor labelling in the contralateral superior colliculus, red nucleus, as well as in the midbrain reticular formation (mRT), and periaqueductal grey (PAG) (Figure 4.17, Figure 4.15, Figure 4.16). We also find premotor labelling bilaterally in the interstitial nucleus of the medial lemniscus (IMLF) and ipsilaterally in nucleus of Darkschewitz (Dk) (Figure 4.16). This labelling pattern is similar to previously reported tracing results from the facial motor nucleus (Hattox-Keller 2002, Issokawa-Akkeson 1987), which labeled inputs to the vibrissa

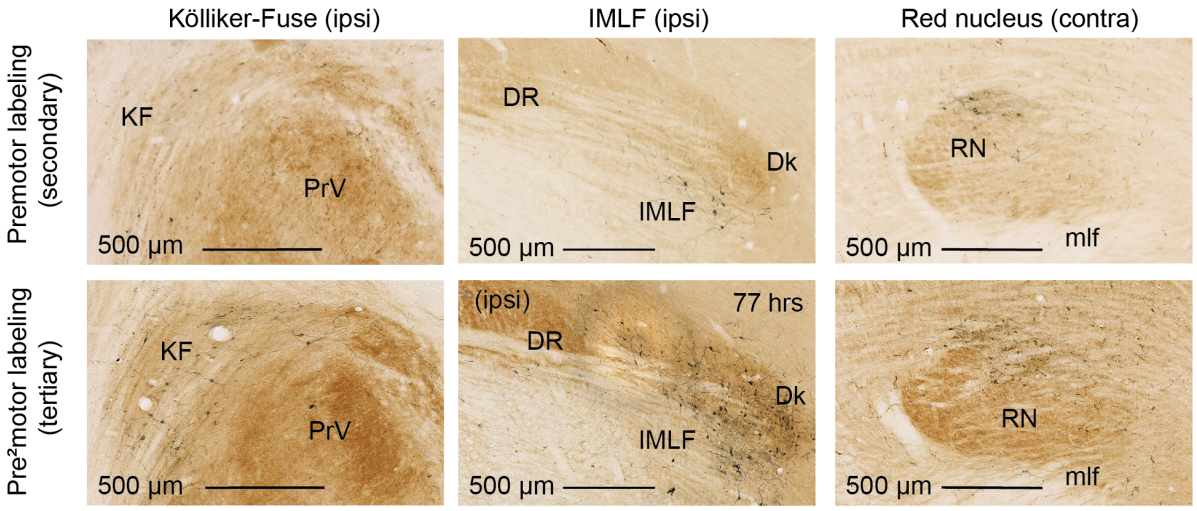

Figure 4.16: Example labeling in midbrain structures and at secondary (upper row) and tertiary (lower row) timepoints. Left: labeling in the ipsilateral Kolliker-Fuse is sparse at 64 hours and dense at 77 hrs. Center: Labeling in the IMLF. Right: Labeling in the red nucleus. Structures outlined from CO stain, rabies labeled cells revealed in dark product.

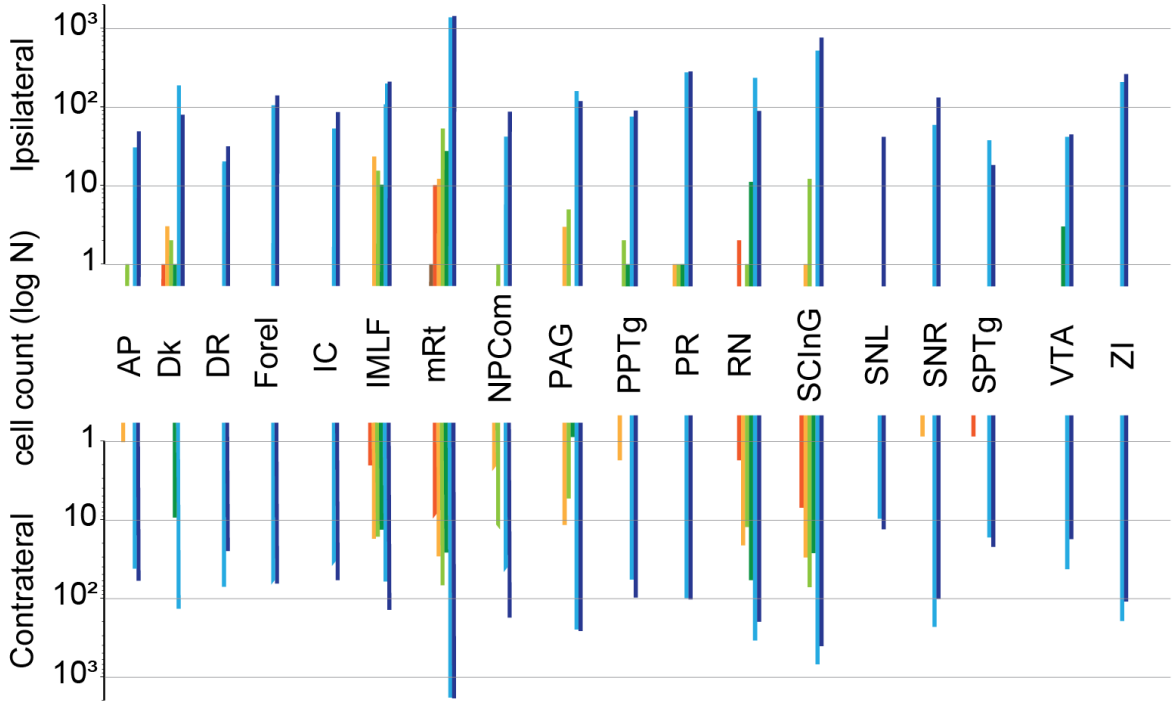

Figure 4.17: Cell counts in the midbrain. Cell counts in ipsilateral (top) and contralateral (bottom) in the midbrain

system, suggesting that a similar circuit structure for control of whisking and nose motion. At tertiary timepoints, we observe increased labeling across the midbrain, including bilaterally in superior colliculus, midbrain reticular formation, raphe magnus nucleus, paralemniscal nucleus, periaqueductal gray. We also observed the appearance of labeled cells in the substantia nigra reticular part (Snr) and lateral part (SNl), zona incerta (ZI), fields of Forel, prerubral fields(PR), nuclei of the posterior commissure (NPCom), and ventral tegmental area (VTA) Figure 4.17. Tertiary midbrain labeling was denser contralaterally, but present on both sides.

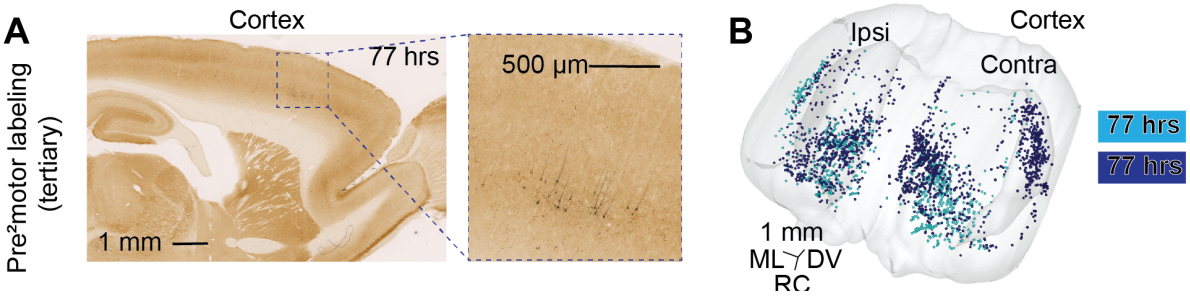

Figure 4.18: Cortical labeling. (A) Cortical labeling example at a tertiary timepoint. (B) Reconstructions of cortical labelling reveal dense projections from motor and sensorimotor areas.

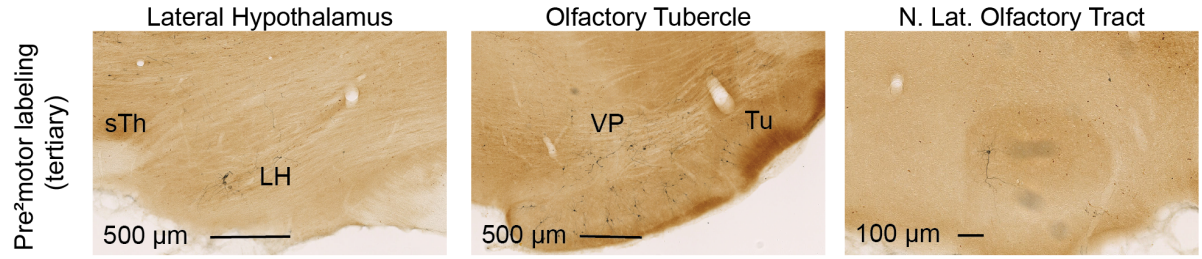

Figure 4.19: Example labeling in forebrain structures and at tertiary timepoints. Left: labeling in the ipsilateral Lateral Hypothalamus. Center: Labeling in the Olfactory tubercle and ventral pallidum. Right: Single labeled cell in the nucleus of the lateral olfactory tract. Structures outlined from CO stain, rabies labeled cells revealed in dark product.

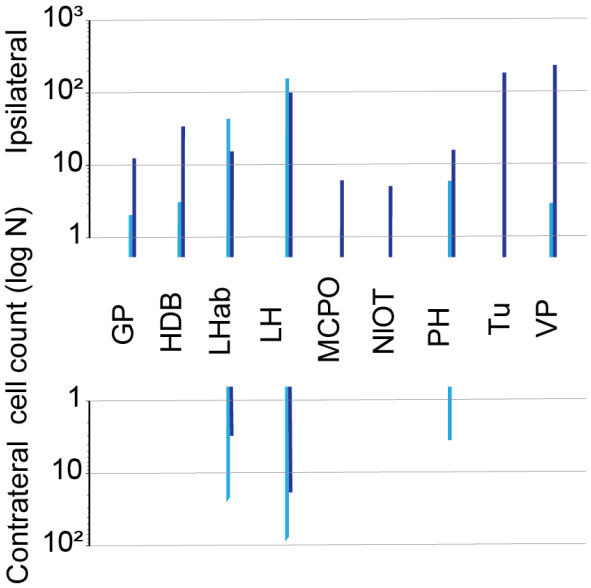

Figure 4.20: Cell counts in the forebrain: ipsilateral (top) and contralateral (bottom)

4.4.5 Retrograde labeling in the forebrain

At tertiary timepoints we observed labeling in the forebrain including bilateral labeling in the cortex (Figure 4.18), in the lateral hypothalamic area, posterior hypothalamic area, sparse labelling in the ipsilateral ventral pallidum, the ipsilateral globus pallidus, ipsilateral nucleus of the horizontal limb of the diagonal band and in the ipsilateral lateral habenula (Figure 4.20, Figure 4.19). In one example we observed sparse labelling in the ipsilateral nucleus of the lateral olfactory tract, in the ipsilateral magnocellular preoptic nucleus and dense labeling in the ipsilateral olfactory tubercle (Figure 4.16). These putative pre-premotor projections are candidate areas for descending motor pathways from the olfactory system and motor cortex. Due to the timepoint approach to labeling with replication competent rabies virus, some of these long range projections may be in fact premotor areas. Anterograde tracing could be used to determine specific pathways by which these areas send inputs to the nose motion control.

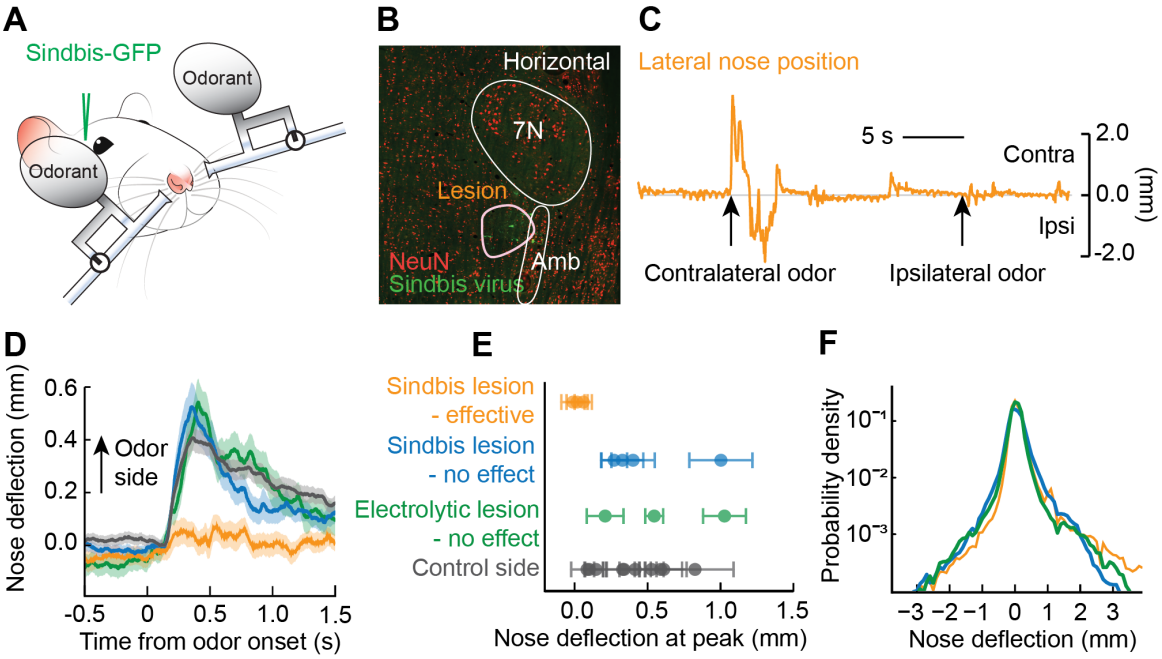

Figure 4.21: Lesions in retrofacial area disrupt nose odor response. (A) Diagram of the rat testing setup. Bedding odor presented on alternate sides and nose position monitored using high speed video in a head-restrained rat. Rats were tested 5 days after Sindbis virus injection or electrolytic lesion. (B) Example histological section to confirm location of Sindbis virus injection (green). NeuN stain (red) used to establish region of cell death. (C) Example trace of lateral nose position response to odor presentation in a rat lesioned with sindbis virus in the retrofacial area. The nose deflects towards the non-lesioned side when an odor is presented on the non-lesioned side, but does not deflect towards the lesioned side when an odor is presented on that side. (D) Average trace of lateral nose position towards presented bedding odor. Averages are shown for four conditions: contralateral side from all lesions (grey), ipsilateral side for non-effective electrolytic lesion (green), ipsilateral side for non-effective Sindbis lesion (blue) and ipsilateral side for effective Sindbis lesion (gold). Error bars are s.e.m. (E) Average peak nose position of ipsilateral (rectified) nose motion averaged between 350-450 ms post odor stimulus presentation. Average values for individual rats shown for four conditions: contralateral side from all lesions (grey), ipsilateral side for non-effective electrolytic lesion (green), ipsilateral side for non-effective Sindbis lesion (blue) and ipsilateral side for effective Sindbis lesion (gold). (F) Average histograms of the lateral nose positions, for non-effective electrolytic lesion (green), non-effective Sindbis lesion (blue) and effective Sindbis lesion (gold).

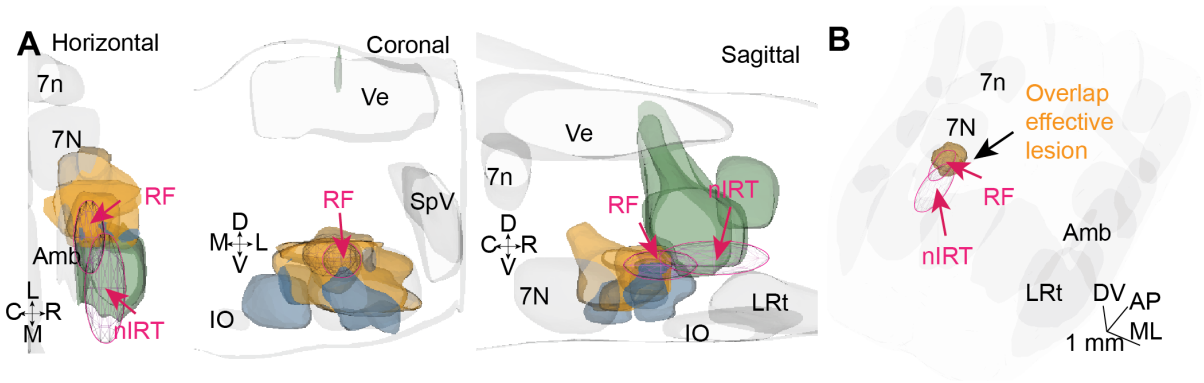

Figure 4.22: Reconstructions of rat lesions that disrupt nose odor response. (A) 3D reconstructions of lesion locations. 400 μm slices shown in the sagittal, coronal and horizontal directions. Locations of the RF and nIRT are outlined in magenta. Effective lesion sites overlap with the RF region and not the nIRT region. (B) 3D reconstruction of the location of the overlap of all effective lesions (gold). Locations of the RF and nIRT are outlined in magenta. All effective lesions overlap in the retrofacial area.

4.4.6 Retrofacial area lesion in rats affects nose odor response

To establish the functional significance of the identified areas, we aimed to test whether ablating the retrofacial area can affect the nose movement response to odor presentation. As the retrofacial area is dense with fiber tracts, we chose sindbis virus as a lesioning method to kill cells without damaging the passing fibers. We also include analysis from electrolytic lesions in the nose-IRT region. We find that three of the sindbis virus lesioned rats had a reduced average peak nose deflection compared to the control averages (Figure 4.21). 3D reconstructions of effective lesion positions showed that all effective lesions were in the retrofacial area, while non-effective lesions flanked the region (Figure 4.22). The average traces for each condition showed that there is no change in the shape of the nose response for the non-effective lesions, while the nose motion response for retrofacial-lesioned animals was greatly reduced. Finally, we considered the distribution of all nose positions for the lesioned vs control animals. We find that on a longer timescale, the lesioned animals are still able to move their nose both to the control side and lesioned side (Figure 4.21). As a note, it is possible that lesions with a larger extent would cause an asymmetry of motion of the nose, however we cannot increase the size of the sindbis virus

lesions without risk of damaging the facial motor nucleus. Our data here show that lesions of the retrofacial area can disrupt nose movement response to odor without completely removing the ability of the rat to move the nose to the affected side.

4.4.7 Retrofacial area glutamatergic lesion in mice affects nose odor response

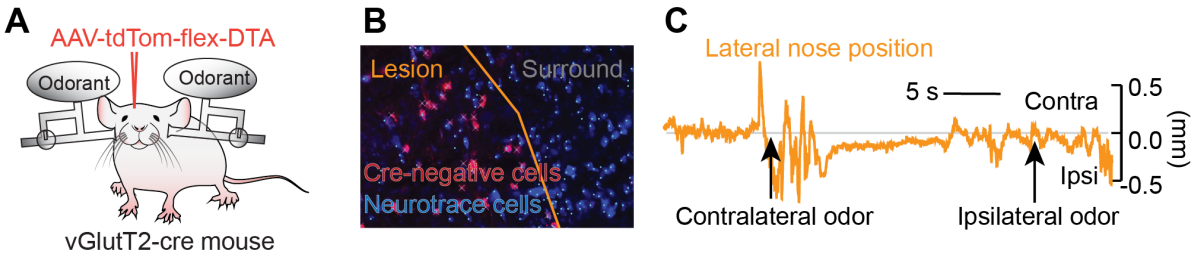

Figure 4.23: Glutamatergic cell lesions in retrofacial area disrupt nose odor response - example (A) Diagram of the mouse testing setup. Bedding odor presented on alternate sides and nose position monitored using high speed video in a head-restrained mouse. Mice were tested 5-6 weeks after AAV-tdTom-flex-DTA injection. (B) Example histological section to confirm location of virus injection based on the locations of cre-negative cells (red). To confirm cell death in a region of interest in the RF area, neurotrace blue stained (blue) cells were counted using an automated algorithm (cyan). (C) Example trace of lateral nose position response to odor presentation in a mouse lesioned with DTA in the retrofacial area. The nose deflects towards the non-lesioned side when an odor is presented on the non-lesioned side, but does not deflect towards the lesioned side when an odor is presented on that side. (D) Average histograms of the lateral nose positions, for non-effective electrolytic lesion (green), non-effective Sindbis lesion (blue) and effective Sindbis lesion (gold).

Cells in the retrofacial area send primarily glutamatergic projections to the facial motor nucleus, while motoneurons themselves do not express vGluT2 [23]. Thus we aimed to confirm that ablating the glutamatergic cells in the retrofacial area can affect the nose movement response to odor presentation. We use a cre-dependent diphtheria toxin subunit a (DTA) virus to ablate vGluT2 expressing cells in adult mice (Figure 4.23A), and find a reduced nose motion response to odor presentation in five of the nine lesioned mice (Figure 4.23). All effective injections were centered in the retrofacial area (Figure 4.25). In addition, we find that the cell count is reduced in

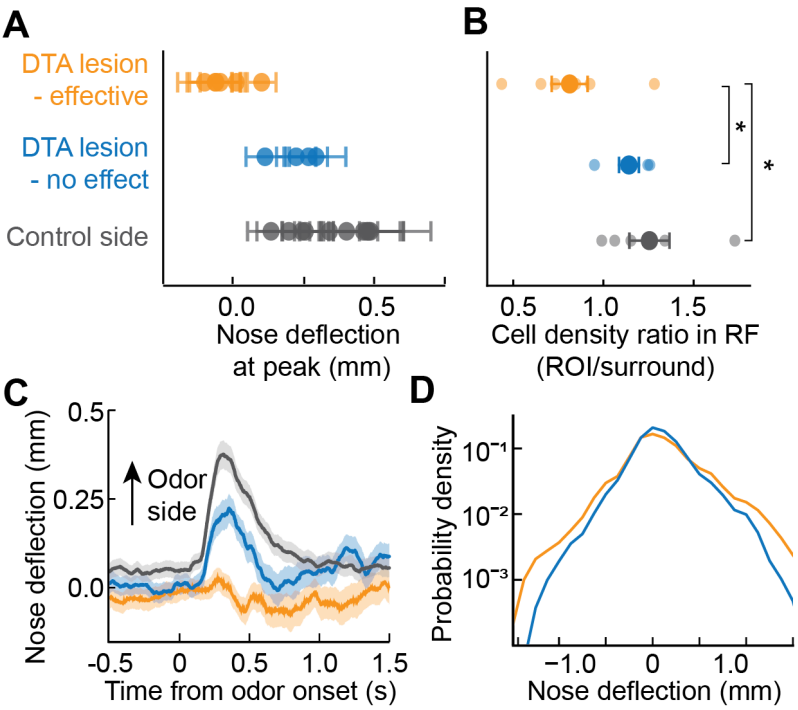

Figure 4.24: Glutamatergic cell lesions in retrofacial area disrupt nose odor response - example (A) Average peak nose position of ipsilateral (rectified) nose motion averaged between 250-300 ms post odor stimulus presentation. Effective lesions (gold) were defined as mice in which the average peak position was less than all control side (black) averages. Non-effective DTA lesions (blue) had an average peak position similar to control side averages. (B) Ratio of cell density in the ROI in the retrofacial area vs the cell density in the surrounding area (grey). Mice with a behavioral reduction in nose response (gold) showed a reduced cell count compared to the control side (black) (T-statistic=-2.5, pvalue=0.035) and compared to non-effective lesions (blue) (T-statistic=-2.4, pvalue=0.044). While non effective lesions showed no change compared to the control side (T-statistic=-0.8, pvalue=0.47) (C) Average trace of lateral nose position towards presented bedding odor. Averages are shown for three conditions: contralateral side from all lesions (grey), ipsilateral side for non-effective lesion (blue) and ipsilateral side for effective lesion (gold). (D) Average histograms of the lateral nose positions, for non-effective electrolytic lesion (green), non-effective Sindbis lesion (blue) and effective Sindbis lesion (gold).

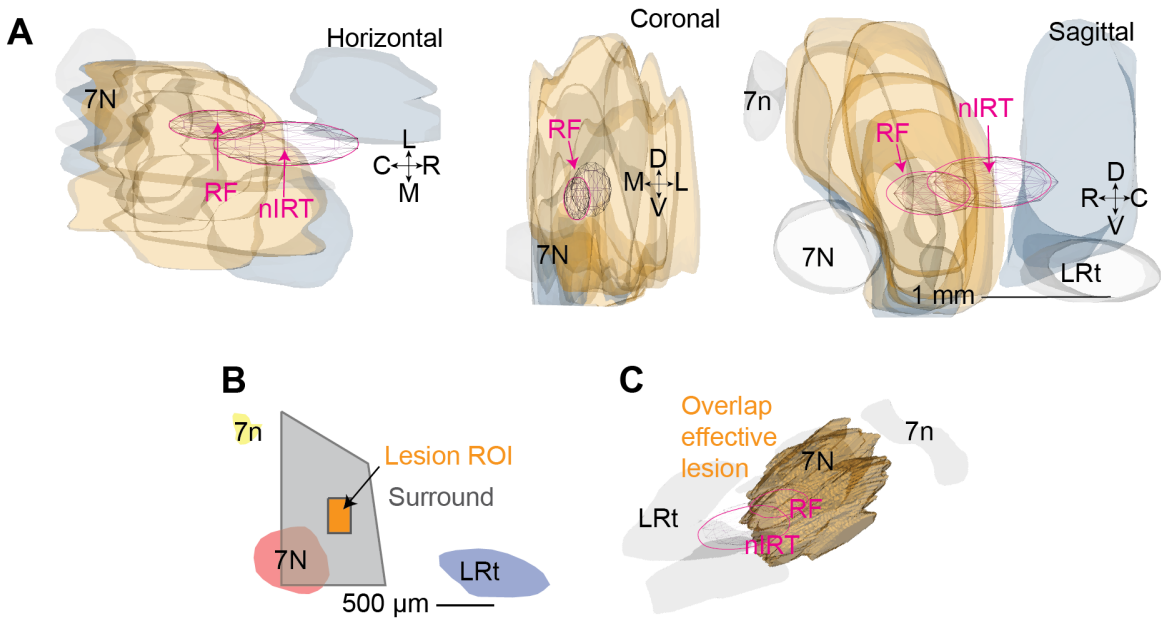

Figure 4.25: Reconstructions of mouse vGluT2 lesions that disrupt nose odor response. (A) Definition of region of interest for cell count in RF and surround region displayed in a slice reconstruction 1.0mm lateral of midline. (B) 3D reconstruction of the location of the overlap of all effective lesions (gold). Locations of the RF and nIRT are outlined in magenta. All effective lesions overlap in the retrofacial area. (C) 3D reconstructions of lesion locations. 400 μm slices shown in the sagittal, coronal and horizontal directions. Locations of the RF and nIRT are outlined in magenta.

an region of interest in the retrofacial area compared to the control side, and compared to animals with no change in nose movement (Figure 4.24,Figure 4.25).

4.4.8 Optogenetic stimulation evokes nose movement independent of changes in breathing rate.

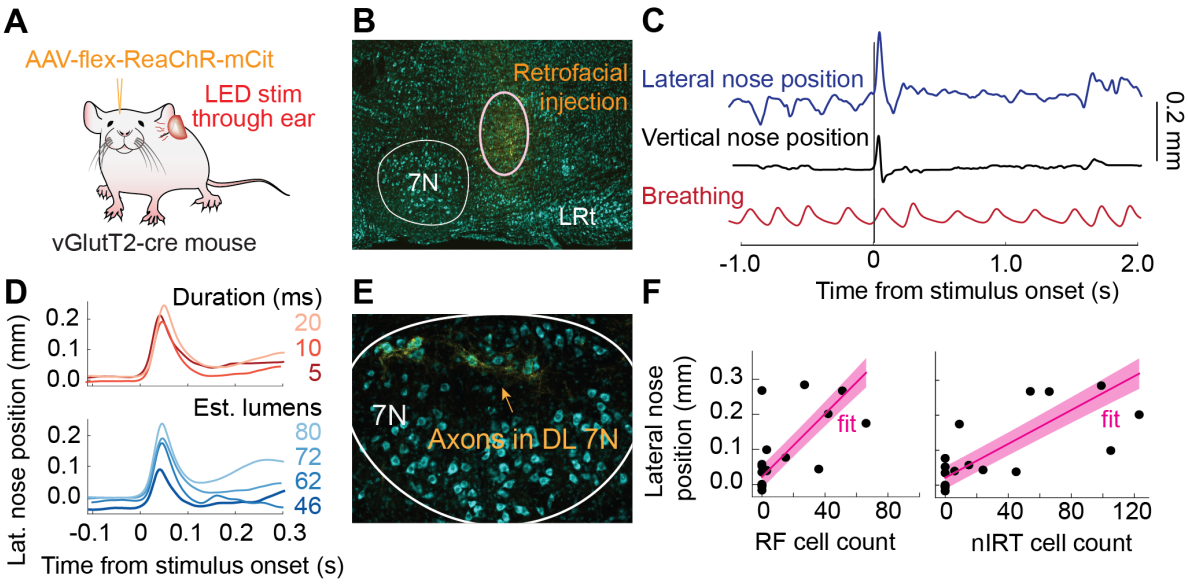

Figure 4.26: Optogenetic stimulation can evoke nose movement. (A) Diagram of the experimental setup. Transgenic mice were injected with an AAV virus to drive expression of red shifted channelrhodopsin (ReaChR) in glutamatergic cells at the injection site. Nose movement was monitored by high video in head fixed mice, while breathing was monitored with a thermistor implanted in the nasal cavity. Stimulation was done by ReaChR stimulation with an LED through the ear canal. (B) Example histological identification of an injection site in the retrofacial area. Cell bodies stained with neurotrace stain (cyan) mCit labeled cells in yellow. (C) Example trace of lateral nose motion (blue), vertical nose motion (black), and breathing (red). The nose deflects laterally and upward after stimulation with a 10 ms led pulse. Injection site shown in panel (B) (D) Example average lateral nose motion response to stimulation at 5ms (dark red) 10 ms (red) and 20 ms (light red), with current adjusted such that the power remains constant across parameters (top). Example average lateral nose motion response to stimulation with 10 ms pulses 46 mA (dark blue) 62 mA (medium blue) 72 mA (blue) and 80 mA (light blue) (bottom). (E) Axons (yellow) labelled in the dorsolateral facial motor nucleus after AAV-flex-ReaChR-citrine injection into the retrofacial area. Cell bodies stained with neurotrace stain (cyan) Injection site shown in panel (B) (F) Average lateral nose peak position after stimulation with a 10 ms pulse as a function of cell counts in the RF and nIRT areas. Each point is the average from a single mouse. Linear fits shown in magenta.

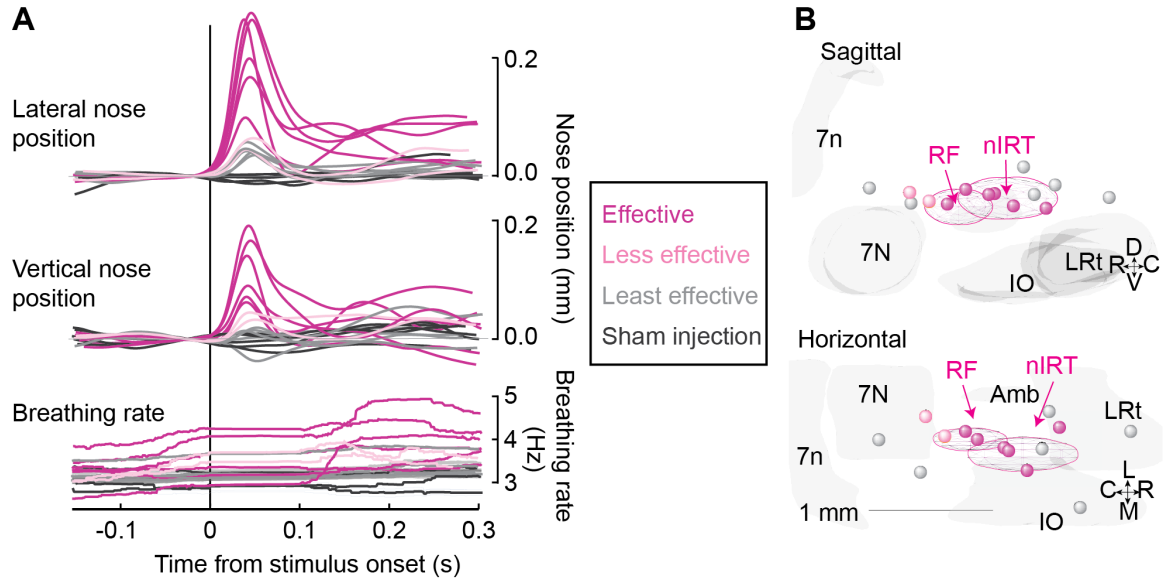

Figure 4.27: Optogenetic stimulation in RF and nIRT areas evoke nose movement. (A) Average traces of lateral nose movement, vertical nose movement, and breathing rate after stimulus onset. Trials selected by movement variance prior to stimulation onset, and <0.5 Hz breathing rate change as compared before and 100 ms after stimulation onset. Effective stimulation sites (magenta), less effective stimulation sites (orange) and least effective stimulation sites (grey) are defined from the functional data. Sham injections (black) were done in cre-negative mice. (B) 3D reconstructions of ReaChR injection centroids. Sagittal (top) and horizontal (bottom) views are shown. Colors drawn from the functional results in G. Centroids of effective stimulation sites (magenta) tend to overlap with the RF and nIRT regions.

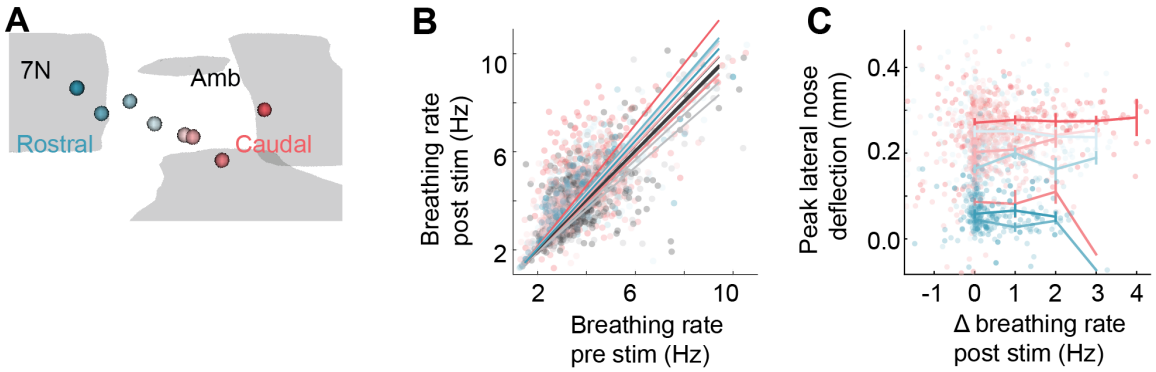

Figure 4.28: Nose movement evoked by optogenetic stimulation is independent of breathing (A) Color coding of all effective stimulation sites from rostral (blue) to caudal (red) (B) Peak lateral nose deflection as a function of change in breathing rate post stimulation. Flat profile of the graph indicates that lateral nose movement evoked by stimulation does not depend on eliciting a change in breathing rate (C) Breathing rate pre vs breathing rate post stim. Stimulation of some injection sites show a slight increase in breathing rate, but on most trials the breathing rate remains constant.

We optogenetically stimulate the glutamatergic population of cells in the retrofacial and nIRT areas to determine the effects of their stimulation on nose motion, by using AAV-flex-ReaChR, a red shifted channelrodopsin (Figure 4.26A). Lateral and upward nose movement - a signature of activity of the *deflector nasi* - was evoked after light stimulation in 8 stimulation sites (Figure 4.27). In off target injection sites, we observe a small lateral nose movement but no consistent upward nose movement, thus the movement of the nose could be an effect of pulling other muscles in the snout. We find that effective stimulation sites have centroids in the retrofacial and caudal nIRT regions (Figure 4.27B). We also consider the lateral evoked nose movement as a function of number of cells counted within the RF and nIRT regions. We find that both cell count in the RF region and cell count in the nIRT region predict lateral nose movement response (F-statistic 4.5, $p < 0.05$ F-statistic 8.3, $p < 0.02$, respectively) and the combination of the two cell counts predicts the lateral nose response well (F-statistic 13.6, $p = 0.0004$), with coefficients 0.0019 mm/cell ($p = 0.03$) in the RF 0.0014 mm/cell ($p = 0.004$) in the nIRT (Figure 4.26). Finally, we consider the relationship of breathing rate change to amplitude of evoked nose motion on individual trials. We find that although at some injection sites, an increase in breathing rate is evoked by stimulation (Figure 4.28B), the amplitude of nose movement is independent of change in breathing rate (Figure 4.28C) Thus, we conclude that optogenetic stimulation of glutamatergic cells in both the RF and in the nIRT can evoke nose movement independently of breathing rate.

4.5 Discussion

We have identified two key premotor areas for controlling nose motion - the nose retrofacial area, and nose IRt area. We have established that glutamatergic inputs from both of these areas can drive motion of the nose, however only the retrofacial nose area is involved in the nose response to odor. We have also provided evidence that the PreBötzinger complex sends

putative pre-premotor input to the nose motoneurons, presumably via one or both of the retrofacial area, and nose IRt areas. Further work could determine relative the contribution of retrofacial and caudal IRt regions to lateral motion of the nose in relation to the respiratory drive. Many possibilities exist for the broader circuit. For example both the retrofacial and other areas could be involved in generating rhythmic movement, or that another area such as the caudal IRt mediates the nose motion correlation to breathing, while the retrofacial area contributes only to the slow component. In our work we have characterized the contribution of glutamatergic inputs from the nose retrofacial area, and nose IRt areas to nose motion. However, whisking generation is known to occur via an inhibitory oscillator that is positioned similarly to the nose caudal IRt. Determining the cell types involved in control of nose movement and potential contribution of inhibitory drive to nose motion would open the possibility of comparing this medullary circuit to control of whisking. Finally since the retrofacial area seems to be necessary for responses to olfactory stimuli, studying the retrograde projections from this area could elucidate a pathway from the accessory olfactory nucleus to the medulla that is involved in responses to odors.

4.6 Methods

4.6.1 Tracing with Replication Competent Rabies Virus

We set up an isolated BSL2+ facility to perform replication competent rabies virus injections and to house injected animals. The facility and our experimental protocol follow all recommendations described in Kelly and Strick 2010 [55]. To perform the injections, rats were anesthetized using ketamine/xylazine, and placed in a stereotaxic apparatus. We exposed the *deflector nasi* muscle and checked that the correct muscle was identified by stimulating with pulses of current (up to 0.1 mA) to evoke movement of the nose [20]. Finally, we used a pressure injector (Drummond Scientific NANOJECT II) to inject a total of 2 μL of CVS-N2c strain rabies virus (Schnell Lab, Thomas Jefferson University) in 5 spots along the muscle. Rats were perfused

at select timepoints between 48 and 96 hours after the injection.

After perfusion, brains were extracted and placed in 30% sucrose solution. Brains were cut on a freezing sliding microtome at 60 μm and stained for cytochrome oxidase. Rabies labeled cells were stained using anti Rabies-L mouse antibody (Schnell lab) and revealed in dark product using a biotinylated secondary antibody, the ABC and SG kits (Vector Labs). For seven of the brains, every third section was cut at 40 μm and stained for Neurotrace Blue while rabies labeled cells were stained using anti Rabies-L mouse antibody and revealed in fluorescence with a secondary GFP antibody (Invitrogen A11029). In addition, in 3 brains, the sections were also stained for somatostatin (T-4103, Peninsula Laboratories) to identify the location of the PreBötzinger complex [98]. Nineteen rats total were injected with rabies virus. Of these, five (at timepoints of 50 hrs, 67 hrs 72hrs, 61.5hrs, and 79.5hrs) had no labeled cells and thus were excluded from analysis. Additionally, two brains with timepoints of 96 hours were excluded from analysis as labelling in the brainstem was too dense for processing. Finally a 72 hr labeled timepoint was excluded from analysis because midline sections were missing in histology. The labeling in this brain was consistent with observed labeling patterns at primary labeled timepoints.

4.6.2 Reconstruction and alignment

We used Neurolucida software (MBF) to create full 3D reconstructions of labelled cell body locations in all brains that had labelled cells. Brains were annotated by outlining key structures visible in cytochrome near identified labeled cells. In brains with alternating Neurotrace sections, nucleus ambiguus and the inferior colliculus were outlined based on the cytoarchitecture. Finally, in brains with somatostatin labelling, the PreBötzinger complex was identified as the area with higher SST cell density. One brain was fully annotated with all midbrain and hindbrain structures described in the Paxinos atlas [105]. All outlined structures are listed in Table A.1 in the appendix.

First, a reference atlas was created from by averaging six reconstructed brains [17]. Briefly,

structures to be used for alignment - the facial motor nucleus (7N), facial motor tract (7n), lateral reticular nucleus (LRt), trigeminal motor nucleus (5N), and inferior olive (IO) and used for aligning the stacks to a single 'reference' stack using an affine transform. Then, average center positions for all traced structures across stacks were calculated. A midline plane was determined as a fit to the midpoints between only the alignment structures, and structure positions for the atlas were rotated such that they are set symmetrically about the midline. Finally, structure shapes were calculated by aligning and averaging each structure individually. The final symmetrical reference atlas was constructed by placing each averaged structure at its average position on each side.

In a final step, each of the reconstructed brains was aligned to the reference atlas using the 'alignment' structures. An affine transform with a allowable scaling range between 99%-101% was used.

4.6.3 Data analysis

Retrograde tracing cell counts were calculated from the aligned reconstructions. Cell counts were done by re-slicing, the aligned data sets at a thickness of μm and assigning each marked cell to the traced and reconstructed region. To account for gaps in traced regions that come from smoothing the reconstruction, cells that did not fall within any traced boundary were assigned to the boundary to which they were nearest. If a cell was within an overlap of two boundaries, it was assigned to the boundary where it was more deeply embedded. Figure 4.4B shows an example of a single section with cells colored by assigned region. Cell count analysis was performed using custom scripts written in python. Cell density was evaluated by computing a kernel density estimate with a 200 μm bandwidth Gaussian kernel on each full volume. 10% maximum contours of labeling were defined by density areas greater than a threshold corresponding to the 10th percentile of the density individually by stack. To evaluate maximally overlapping areas across different labeled brains, volumes in which at least four stacks

had a overlap of at least 15% max density were constructed. A Gaussian mixture model with 2 components was fit to all cells within this maximum density volume, with weights assigned as the inverse of number of labeled cells per brain to ensure equal contribution of each labeled brain. AIC and BIC for the Gaussian mixture model were evaluated for models of one, two and three components to determine optimal fit. In order to compare mouse functional experiments to the tracing results from rat data, the rat atlas was aligned to mouse volumes with an affine transform and allowable scaling up to 40%. An identical transform was applied to the results of the Gaussian fit to obtain an estimate of the location of the two putative pre-motor areas.

4.6.4 Lesions in rats

Eight rats were injected with concentrated Sindbis-152-GFP virus (Patrick lab, UCSD) to drive expression virus at the injection site, and cause cell death after 4-5 days [74]. When tested in culture, the virus infected >90% of cells, thus we expect that a majority of cells at the injection site take up the virus. An additional 3 rats were electrolytically lesioned by lowering a stainless steel electrode into the caudal IRt area and passing pulses of 300 μA for 5 seconds. Rat were implanted with a headbar for head fixation, and a thermocouple (5TC-TT-K-36-36, Omega Engineering) to monitor breathing 2 days after virus injection. Rats were placed in the setup for acclimation once prior to testing, and were tested for evoked nose movement in response to odor five days after virus injection. For testing, bedding odor was presented alternately on either side of the snout as in Kurnikova et al 2017. Video data were collected via a high speed camera (Basler A602f) using custom code written in MATLAB, and standard LabChart functions. Rats were perfused and brains sectioned on a freezing microtome. For Sindbis virus lesions, 30 μm horizontal sections were stained for NeuN, and the lesion site was identified by the area of cell death as evidenced by a lack of NeuN stained cells. For electrolytic lesions, 60 μm sections were stained with Neutral Red, and the lesion site was identified as a hole or obvious damage to the tissue. 3D reconstructions of the lesion site in every 3rd section were made using Neurolucida,

and further processed using custom code in python.

4.6.5 Lesions in mice

10 mice Vglut2-ires-cre (JAX 028863) were injected with AAV8-mCherry-flex-DTA virus to drive expression of diptheria toxin subunit A in glutamatergic cells at the injection site. Mice were implanted with a headbar for head fixation, and a fast-time NTC thermistor (MEAS-G22K7MCD419, Measurement Specialties) to monitor breathing (McAfee et al 2016) three to four weeks post virus injection. Mice were placed in the setup for acclimation at least once prior to testing, and were tested for evoked nose movement five to six weeks after virus injection. For testing, bedding odor was presented alternately on either side of the snout as in Kurnikova et al 2017. Video data were collected via a high speed camera (Basler A602f) using custom code written in MATLAB, and standard LabChart functions. Mice were perfused and brains sectioned at 25 μm on a freezing microtome. Sections were stained for Neurotrace Blue (Thermo-Fischer N21479), and an over estimate of the size and location of the injection site was identified by TdTomato in non-glutamatergic cells. 3D reconstructions of labeled cells and key structures in every 3rd section were made using Neurolucida. All reconstructions were aligned to a single selected mouse brain using procedures from Chen et al 2018 [17], and displayed and compared using custom code in python.

We performed a cell count in the retrofacial area in all lesioned animals, and 5 contralateral side sections as control, using a cell counting algorithm in Neurolucida. We counted all Neurotrace Blue labeled cells in an single section 1.0 mm lateral of midline , manually adjusted counting parameters to ensure reasonable results in each instance. Cell counted regions of interest (ROI) were aligned to each other by applying translation parameters from the 3D alignment, with no rotation to prevent affecting the cell density.

4.6.6 Optogenetic stimulation in mice

13 mice Vglut2-ires-cre (JAX 028863) were injected with AAV8-flex-ReaChR-citrine (Addgene 50955, virus produced by Salk Vector Core) virus to drive expression of red shifted channelrhodopsin (ReaChR) in glutamatergic cells at the injection site. An additional 5 negative transgenic mice (negative for Cre) were injected with the same virus as a sham injection. Sham injected mice were tested as blind controls along with the positive mice, to avoid bias in LED placement when comparing results. Mice were implanted with a headbar for head fixation, and a fast-time NTC thermistor (MEAS-G22K7MCD419,Measurement Specialties) to monitor breathing (McAfee et al 2016) two weeks post virus injection. Mice were placed in the setup for acclimation at least once prior to testing, and were tested for evoked nose movement three weeks after virus injection. For optogenetic stimulation, a Mightex 2-channel LED controller (Mightex systems SLC-MA02-U) was used to drive a 617nm Luxeon LED (Lumileds LXM2-PH01-0070) placed in the ear, at 355mA for 10ms pulses. Video data were collected via a high speed camera (Basler A602f) using custom code written in MATLAB, and standard LabChart functions. Mice were perfused and brains sectioned at 30 μm on a freezing microtome. Sections were stained for Neurotrace far red (Thermo-Fischer N21483), and the injection site was identified by the citrine label in cell membranes. 3D reconstructions of labeled cells and key structures in every 3rd section were made using Neurolucida, and further processed using custom code in Python. All reconstructions were aligned to a single selected mouse brain using procedures from Chen et al 2018 [17], and displayed and compared using custom code in python.

4.7 Author contributions

The material of Chapter 4 is a manuscript that is currently under preparation for submission: A. Kurnikova, M. Deschênes and D. Kleinfeld, Functional brainstem circuits for control of nose motion. The dissertation author was the primary investigator and author of this material.

Chapter 5

Conclusion

Here, we have elaborated on known circuits in the vibrissa system, and have investigated properties of nose motion and the neural circuits that control it. The work presented in this manuscript sets the stage for a variety of potential experimental questions that will allow comparison of nose motion control to other systems.

Future work could go beyond the analysis adressed in this thesis to investigate cell types involved in nose motion control. In fact, the whisking movement generator has been found to function by inhibitory control [23]. What might be the role of inhibitory cells in the nIRT premotor area to nose motion?

In addition, the putative retrofacial and nIRT areas may be involved in control of rhythmic nose motion similar to the activity of the vIRT. A challenge in pursuing experiments similar to the ones performed in the vibrissa system is that the nose is under bilateral control of the *d. nasi* muscles. Thus, an inactivation of the oscillator on one side of the snout may not allow a behavioral measurement of a deficit in rhythmic motion. We propose lesions throughout the putative premotor areas identified in this work that be combined with a cut of the nerve on the contralateral side in order to evaluate the effect of a given lesion on rhythmic nose motion. These experiment would enable a comparison of the circuitry of rhythmic nose motion to the whisker

system.

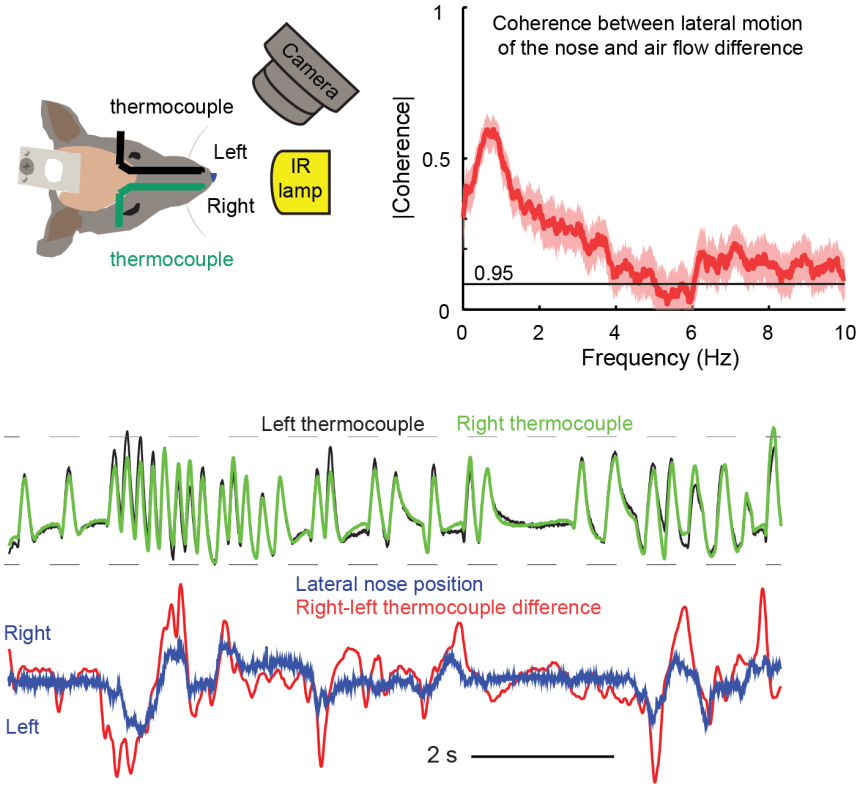

Figure 5.1: Lateral displacement of the nose is related to air flow difference between nostrils (top left) Experimental setup to measure nose motion and nasal airflow in head-restrained rats; IR, infrared light. (top right) Spectral coherence between lateral displacement of the nose and air flow difference between the left and right nostrils. Black line, 95% confidence level based on Gaussian approximation; light red area, 95% confidence interval based on boot-strap. (bottom) Upper traces show normalized respiratory signals recorded from the left and right nostrils. Lower traces show that change in lateral nose position is associated with change in airflow through the left and right nostrils as estimated from difference in the amplitude of thermocouple signals.

What might be the relevance of movement of the nose to olfactory processing? We propose that lateral nose motion might affects air flow between nostrils. In some preliminary data, we measure the difference in air flow between the two nostrils in a rat (Figure 5.1). Our findings support the hypothesis that air flow might be affected by nose motion. Future work might image at the patterns of air flow around a rodents snout whle the nose is moving in order to determine the spacial component of any chages as well.

Overall, we have established nose motion as a model system for studying orofacial motor

action. While it is a simple behavior, nose motion control can be compared both to other orofacial motor actions, and studied in the context of its connections with the olfactory circuitry.

Chapter 5 in part contains work published in: M. Deschênes, A. Kurnikova, M. Elbaz and D. Kleinfeld. "Circuits in the ventral medulla that phase lock motoneurons for coordinated sniffing and whisking", *Neural Plasticity*, 2016. This material is included with the generous consent of all coauthors.

Appendix A

List of abbreviations

Table A.1: List of neuroanatomical annotation abbreviations

5N	trigeminal motor nucleus
7N	facial motor nucleus
7n	facial tract
AP	anterior pretectal nucleus
Amb	nucleus ambiguus
DMSp5	dosomedial spinal trigeminal nucleus
Dk	nucleus Darkschewitz
DR	dorsal raphe nucleus
Forel	fields of forel
IO	inferior olive
Gi	gigantocellular reticular nucleus
GiA	gigantocellular reticular nucleus alpha part
GiV	gigantocellular reticular nucleus ventral part
Continued on next page	

Abbreviation	Structure name
GP	globus pallidus
HDB	nucleus of the horizontal limb of the diagonal band
Hipp	hippocampus
IC	inferior colliculus
IMLF	interstitial nucleus of the medio-lateral formation
iTg	intertrigeminal nucleus
IRt	intermediate reticular nucleus
KF	Kölliker-Fuse nucleus
LDT	laterodorsal tegmental nucleus
LH	lateral hypothalamic area
LPB	lateral parabrachial nucleus
LPBE	lateral parabrachial nucleus, pars externa
LPGi	lateral paragigantocellular nucleus
LRt	lateral reticular nucleus
MCPO	magnocellular preoptic nucleus
MPB	medial parabrachial nucleus
MdD	medulary reticular nucleus, dorsal part
MdV	medulary reticular nucleus, ventral part
MiTg	microcellular tegmental nucleus
Mx	matric region of the medulla
NLOT	nucleus of the lateral olfactory tract
NPCom	nucleus of the posterior commisure
PAG	periaqueductal grey

Continued on next page

Abbreviation	Structure name
PCRt	parvicellular reticular nucleus
PCRtA	parvicellular reticular nucleus, alpha part
PH	posterior hypothalamic area
PMnR	paramedian reticular nucleus
PPTg	posterior pretectal nucleus
PR	prerubral field
PR5VL	principal sensory trigeminal nucleus, dorsomedial part
PaR	pararubral area
PnC	pontine reticular nucleus, pars caudalis
PnO	pontine reticular nucleus, pars oralis
Pr5	principal sensory trigeminal nucleus
PreBötC	PreBötzinger complex
pCom	precommisural nucleus
RIP	raphe interpositus nucleus
RMg	raphe magnus nucleus
RN	red nucleus
ROB	raphe obscurus nucleus
RPa	raphe pallidus
RtTg	retuculotegmental nucleus of the pons
SC_InG	superior colliculus, inferior grey
SC_SuG	superior colliculus, superior grey
SNC	substantia nigra, pars compacta
SNL	substantia nigra, pars lateralis

Continued on next page

Abbreviation	Structure name
SNR	substantia nigra, pars reticularis
SPTg	subpeduncular tegmental nucleus
SPVmu	spinal trigeminal nucleus, pars muralis
Sol	nucleus of the solitary tract
SpVI	spinal trigeminal nucleus, pars interpolaris
SpVC	spinal trigeminal nucleus, pars caudalis
SpVO	spinal trigeminal nucleus, pars oralis
Su5	supratrigeminal nucleus
SubC	subcoeruleus nucleus
Tu	olfactory tubercle
VLL	ventral nucleus of the lateral lemniscus
VP	ventrap pallidum
VTA	ventral tegmental nucleus
Ve	vestibular nuclei
ZI	zona incerta
ac	anterior commisure
f	fornix
fr	fasciculus retroflexus
ml	medial lemniscus
mlf	medial longitudinal fasciculus
pc	posterior commissure
scp	superior cerebellar peduncle

Bibliography

[1] K. D. Alloway, J. B. Smith, and K. J. Beauchemin. Quantitative analysis of the bilateral brainstem projections from the whisker and forepaw regions in rat primary motor cortex. *J. Comp. Neurol.*, 518(22):4546–4566, Nov 2010.

[2] K. D. Alloway, J. B. Smith, K. J. Beauchemin, and M. L. Olson. Bilateral projections from rat MI whisker cortex to the neostriatum, thalamus, and claustrum: forebrain circuits for modulating whisking behavior. *J. Comp. Neurol.*, 515(5):548–564, Aug 2009.

[3] M. L. Andermann and C. I. Moore. A somatotopic map of vibrissa motion direction within a barrel column. *Nat. Neurosci.*, 9(4):543–551, Apr 2006.

[4] R. W. Berg and D. Kleinfeld. Rhythmic whisking by rat: retraction as well as protraction of the vibrissae is under active muscular control. *J. Neurophysiol.*, 89(1):104–117, Jan 2003.

[5] R. Bermejo, W. Friedman, and H. P. Zeigler. Topography of whisking II: interaction of whisker and pad. *Somatosens Mot Res*, 22(3):213–220, Sep 2005.

[6] R. Bermejo, M. Harvey, P. Gao, and H. P. Zeigler. Conditioned whisking in the rat. *Somatosens Mot Res*, 13(3-4):225–233, 1996.

[7] E. Bizzi, R. E. Kalil, and V. Tagliasco. Eye-head coordination in monkeys: evidence for centrally patterned organization. *Science*, 173(3995):452–454, Jul 1971.

[8] H. Bokil, P. Andrews, J. E. Kulkarni, S. Mehta, and P. P. Mitra. Chronux: a platform for analyzing neural signals. *J. Neurosci. Methods*, 192(1):146–151, Sep 2010.

[9] M. Brecht and W. A. Freiwald. The many facets of facial interactions in mammals. *Curr. Opin. Neurobiol.*, 22(2):259–266, Apr 2012.

[10] M. Brecht, A. Krauss, S. Muhammad, L. Sinai-Esfahani, S. Bellanca, and T. W. Margrie. Organization of rat vibrissa motor cortex and adjacent areas according to cytoarchitectonics, microstimulation, and intracellular stimulation of identified cells. *J. Comp. Neurol.*, 479(4):360–373, Nov 2004.

[11] M. Brecht, M. Schneider, B. Sakmann, and T. W. Margrie. Whisker movements evoked by stimulation of single pyramidal cells in rat motor cortex. *Nature*, 427(6976):704–710, Feb 2004.

[12] A. W. Brown and P. M. Waite. Responses in the rat thalamus to whisker movements produced by motor nerve stimulation. *J. Physiol. (Lond.)*, 238(2):387–401, Apr 1974.

[13] D. Burr and D. Alais. Combining visual and auditory information. *Prog. Brain Res.*, 155:243–258, 2006.

[14] M. Carandini. From circuits to behavior: a bridge too far? *Nat. Neurosci.*, 15(4):507–509, Mar 2012.

[15] G. E. Carvell and D. J. Simons. Task- and subject-related differences in sensorimotor behavior during active touch. *Somatosens Mot Res*, 12(1):1–9, 1995.

[16] K. C. Catania. Stereo and serial sniffing guide navigation to an odour source in a mammal. *Nat Commun*, 4:1441, 2013.

[17] Yuncong Chen. *An Active Texture-based Atlas for Automated Mapping of Structures and Markers Across Brains / by Yuncong Chen*. PhD thesis, University of California, San Diego, 2018.

[18] S. Clarke and J. A. Trowill. Sniffing and motivated behavior in the rat. *Physiol. Behav.*, 6(1):49–52, Jan 1971.

[19] C. A. Del Negro, G. D. Funk, and J. L. Feldman. Breathing matters. *Nat. Rev. Neurosci.*, 19(6):351–367, Jun 2018.

[20] M. Deschenes, S. Haidarliu, M. Demers, J. Moore, D. Kleinfeld, and E. Ahissar. Muscles involved in naris dilation and nose motion in rat. *Anat Rec (Hoboken)*, 298(3):546–553, Mar 2015.

[21] M. Deschenes, A. Kurnikova, M. Elbaz, and D. Kleinfeld. Circuits in the Ventral Medulla That Phase-Lock Motoneurons for Coordinated Sniffing and Whisking. *Neural Plast.*, 2016:7493048, 2016.

[22] M. Deschenes, J. Moore, and D. Kleinfeld. Sniffing and whisking in rodents. *Curr. Opin. Neurobiol.*, 22(2):243–250, Apr 2012.

[23] M. Deschenes, J. Takatoh, A. Kurnikova, J. D. Moore, M. Demers, M. Elbaz, T. Furuta, F. Wang, and D. Kleinfeld. Inhibition, Not Excitation, Drives Rhythmic Whisking. *Neuron*, 90(2):374–387, 04 2016.

[24] J. C. Doyle and M. Csete. Architecture, constraints, and behavior. *Proc. Natl. Acad. Sci. U.S.A.*, 108 Suppl 3:15624–15630, Sep 2011.

[25] B. J. Duistermars, D. M. Chow, and M. A. Frye. Flies require bilateral sensory input to track odor gradients in flight. *Curr. Biol.*, 19(15):1301–1307, Aug 2009.

[26] J. Esquivelzeta Rabell, K. Mutlu, J. Noutel, P. Martin Del Olmo, and S. Haesler. Spontaneous Rapid Odor Source Localization Behavior Requires Interhemispheric Communication. *Curr. Biol.*, 27(10):1542–1548, May 2017.

[27] Sander J. Xu X Ester M., Kriegel H.-P. A density- based algorithm for discovering clusters in large spatial databases with noise. *Proc. 2nd Int. Conf. on Knowledge Discovery and Data Mining, Portland, OR, AAAI Press*, pages 226–231, 1996.

[28] J. L. Feldman and C. A. Del Negro. Looking for inspiration: new perspectives on respiratory rhythm. *Nat. Rev. Neurosci.*, 7(3):232–242, Mar 2006.

[29] J. L. Feldman and K. Kam. Facing the challenge of mammalian neural microcircuits: taking a few breaths may help. *J. Physiol. (Lond.)*, 593(1):3–23, Jan 2015.

[30] E. Friauf. Morphology of motoneurons in different subdivisions of the rat facial nucleus stained intracellularly with horseradish peroxidase. *J. Comp. Neurol.*, 253(2):231–241, Nov 1986.

[31] W. A. Friedman, H. P. Zeigler, and A. Keller. Vibrissae motor cortex unit activity during whisking. *J. Neurophysiol.*, 107(2):551–563, Jan 2012.

[32] R. Furutani, T. Izawa, and S. Sugita. Distribution of facial motoneurons innervating the common facial muscles of the rabbit and rat. *Okajimas Folia Anat Jpn*, 81(5):101–108, Dec 2004.

[33] K. Ganguly and D. Kleinfeld. Goal-directed whisking increases phase-locking between vibrissa movement and electrical activity in primary sensory cortex in rat. *Proc. Natl. Acad. Sci. U.S.A.*, 101(33):12348–12353, Aug 2004.

[34] P. Gao, A. M. Hattox, L. M. Jones, A. Keller, and H. P. Zeigler. Whisker motor cortex ablation and whisker movement patterns. *Somatosens Mot Res*, 20(3-4):191–198, 2003.

[35] A. J. Garcia, S. Zanella, H. Koch, A. Doi, and J. M. Ramirez. Chapter 3–networks within networks: the neuronal control of breathing. *Prog. Brain Res.*, 188:31–50, 2011.

[36] T. V. Gerdjikov, F. Haiss, O. E. Rodriguez-Sierra, and C. Schwarz. Rhythmic whisking area (RW) in rat primary motor cortex: an internal monitor of movement-related signals? *J. Neurosci.*, 33(35):14193–14204, Aug 2013.

[37] A. Gomez-Marin, B. J. Duistermars, M. A. Frye, and M. Louis. Mechanisms of odor-tracking: multiple sensors for enhanced perception and behavior. *Front Cell Neurosci*, 4:6, 2010.

[38] A. Gomez-Marin, G. J. Stephens, and M. Louis. Active sampling and decision making in Drosophila chemotaxis. *Nat Commun*, 2:441, Aug 2011.

[39] P. A. Gray, W. A. Janczewski, N. Mellen, D. R. McCrimmon, and J. L. Feldman. Normal breathing requires preBötzinger complex neurokinin-1 receptor-expressing neurons. *Nat. Neurosci.*, 4(9):927–930, Sep 2001.

[40] S. Grillner, A. McClellan, K. Sigvardt, P. Wallen, and M. Wilen. Activation of NMDA-receptors elicits "fictive locomotion" in lamprey spinal cord in vitro. *Acta Physiol. Scand.*, 113(4):549–551, Dec 1981.

[41] J. M. Guest, M. M. Seetharama, E. S. Wendel, P. L. Strick, and M. Oberlaender. 3D reconstruction and standardization of the rat facial nucleus for precise mapping of vibrissal motor networks. *Neuroscience*, 368:171–186, Jan 2018.

[42] P. G. Guyenet and H. Wang. Pre-Bötzinger neurons with preinspiratory discharges "in vivo" express NK1 receptors in the rat. *J. Neurophysiol.*, 86(1):438–446, Jul 2001.

[43] S. Haidarliu, D. Golomb, D. Kleinfeld, and E. Ahissar. Dorsorostral snout muscles in the rat subserve coordinated movement for whisking and sniffing. *Anat Rec (Hoboken)*, 295(7):1181–1191, Jul 2012.

[44] S. Haidarliu, D. Kleinfeld, M. Deschenes, and E. Ahissar. The Musculature That Drives Active Touch by Vibrissae and Nose in Mice. *Anat Rec (Hoboken)*, 298(7):1347–1358, Jul 2015.

[45] F. Haiss and C. Schwarz. Spatial segregation of different modes of movement control in the whisker representation of rat primary motor cortex. *J. Neurosci.*, 25(6):1579–1587, Feb 2005.

[46] A. M. Hattox, C. A. Priest, and A. Keller. Functional circuitry involved in the regulation of whisker movements. *J. Comp. Neurol.*, 442(3):266–276, Jan 2002.

[47] E. Henneman. The size-principle: a deterministic output emerges from a set of probabilistic connections. *J. Exp. Biol.*, 115:105–112, Mar 1985.

[48] L. J. Herfst and M. Brecht. Whisker movements evoked by stimulation of single motor neurons in the facial nucleus of the rat. *J. Neurophysiol.*, 99(6):2821–2832, Jun 2008.

[49] V. Hernandez Bennetts, A. J. Lilienthal, P. P. Neumann, and M. Trincavelli. Mobile robots for localizing gas emission sources on landfill sites: is bio-inspiration the way to go? *Front Neuroeng*, 4:20, 2011.

[50] D. N. Hill, R. Bermejo, H. P. Zeigler, and D. Kleinfeld. Biomechanics of the vibrissa motor plant in rat: rhythmic whisking consists of triphasic neuromuscular activity. *J. Neurosci.*, 28(13):3438–3455, Mar 2008.

[51] D. N. Hill, J. C. Curtis, J. D. Moore, and D. Kleinfeld. Primary motor cortex reports efferent control of vibrissa motion on multiple timescales. *Neuron*, 72(2):344–356, Oct 2011.

[52] C. F. Hinrichsen and C. D. Watson. The facial nucleus of the rat: representation of facial muscles revealed by retrograde transport of horseradish peroxidase. *Anat. Rec.*, 209(3):407–415, Jul 1984.

[53] M. Isokawa-Akesson and B. R. Komisaruk. Difference in projections to the lateral and medial facial nucleus: anatomically separate pathways for rhythmical vibrissa movement in rats. *Exp Brain Res*, 65(2):385–398, 1987.

[54] Bill Hansson Kathrin Steck, Markus Knaden. Do desert ants smell the scenery in stereo? *Animal Behaviour*, 2010.

[55] R. M. Kelly and P. L. Strick. Rabies as a transneuronal tracer of circuits in the central nervous system. *J. Neurosci. Methods*, 103(1):63–71, Nov 2000.

[56] A. Kepecs, N. Uchida, and Z. F. Mainen. The sniff as a unit of olfactory processing. *Chem. Senses*, 31(2):167–179, Feb 2006.

[57] A. G. Khan, M. Sarangi, and U. S. Bhalla. Rats track odour trails accurately using a multi-layered strategy with near-optimal sampling. *Nat Commun*, 3:703, Feb 2012.

[58] S. Kikuta, K. Sato, H. Kashiwadani, K. Tsunoda, T. Yamasoba, and K. Mori. From the Cover: Neurons in the anterior olfactory nucleus pars externa detect right or left localization of odor sources. *Proc. Natl. Acad. Sci. U.S.A.*, 107(27):12363–12368, Jul 2010.

[59] B. G. Klein and R. W. Rhoades. Representation of whisker follicle intrinsic musculature in the facial motor nucleus of the rat. *J. Comp. Neurol.*, 232(1):55–69, Feb 1985.

[60] D. Kleinfeld, M. Deschenes, F. Wang, and J. D. Moore. More than a rhythm of life: breathing as a binder of orofacial sensation. *Nat. Neurosci.*, 17(5):647–651, May 2014.

[61] D. Kleinfeld, J. D. Moore, F. Wang, and M. Deschenes. The Brainstem Oscillator for Whisking and the Case for Breathing as the Master Clock for Orofacial Motor Actions. *Cold Spring Harb. Symp. Quant. Biol.*, 79:29–39, 2014.

[62] D. Kleinfeld and H. Sompolinsky. Associative neural network model for the generation of temporal patterns. Theory and application to central pattern generators. *Biophys. J.*, 54(6):1039–1051, Dec 1988.

[63] M. Komiyama, H. Shibata, and T. Suzuki. Somatotopic representation of facial muscles within the facial nucleus of the mouse. A study using the retrograde horseradish peroxidase and cell degeneration techniques. *Brain Behav. Evol.*, 24(2-3):144–151, 1984.

[64] A. Kurnikova, J. D. Moore, S. M. Liao, M. Deschenes, and D. Kleinfeld. Coordination of Orofacial Motor Actions into Exploratory Behavior by Rat. *Curr. Biol.*, 27(5):688–696, Mar 2017.

[65] C. Lenschow and M. Brecht. Barrel cortex membrane potential dynamics in social touch. *Neuron*, 85(4):718–725, Feb 2015.

[66] M. E. Llewellyn, K. R. Thompson, K. Deisseroth, and S. L. Delp. Orderly recruitment of motor units under optical control in vivo. *Nat. Med.*, 16(10):1161–1165, Oct 2010.

[67] M. Louis, T. Huber, R. Benton, T. P. Sakmar, and L. B. Vosshall. Bilateral olfactory sensory input enhances chemotaxis behavior. *Nat. Neurosci.*, 11(2):187–199, Feb 2008.

[68] E. Marder and R. L. Calabrese. Principles of rhythmic motor pattern generation. *Physiol. Rev.*, 76(3):687–717, Jul 1996.

[69] H. Martin. Osmotropotaxis in the honey-bee. *Nature*, 208:59Ű63, October 1965.

[70] F. Matyas, V. Sreenivasan, F. Marbach, C. Wacongne, B. Barsy, C. Mateo, R. Aronoff, and C. C. Petersen. Motor control by sensory cortex. *Science*, 330(6008):1240–1243, Nov 2010.

[71] Nicole Mercer Lindsay. *Cortex drives orofacial behaviors through distinct brainstem networks*. PhD thesis, University of California, San Diego, 2018.

[72] B. Mitchinson, C. J. Martin, R. A. Grant, and T. J. Prescott. Feedback control in active sensing: rat exploratory whisking is modulated by environmental contact. *Proc. Biol. Sci.*, 274(1613):1035–1041, Apr 2007.

[73] P. P. Mitra and B. Pesaran. Analysis of dynamic brain imaging data. *Biophys. J.*, 76(2):691–708, Feb 1999.

[74] J. D. Moore, M. Deschenes, T. Furuta, D. Huber, M. C. Smear, M. Demers, and D. Kleinfeld. Hierarchy of orofacial rhythms revealed through whisking and breathing. *Nature*, 497(7448):205–210, May 2013.

[75] J. D. Moore, M. Deschenes, A. Kurnikova, and D. Kleinfeld. Activation and measurement of free whisking in the lightly anesthetized rodent. *Nat Protoc*, 9(8):1792–1802, Aug 2014.

[76] J. Otero-Millan, X. G. Troncoso, S. L. Macknik, I. Serrano-Pedraza, and S. Martinez-Conde. Saccades and microsaccades during visual fixation, exploration, and search: foundations for a common saccadic generator. *J Vis*, 8(14):1–18, Dec 2008.

[77] L. C. Populin and T. C. Yin. Pinna movements of the cat during sound localization. *J. Neurosci.*, 18(11):4233–4243, Jun 1998.

[78] J. Porter, B. Craven, R. M. Khan, S. J. Chang, I. Kang, B. Judkewitz, B. Judkewicz, J. Volpe, G. Settles, and N. Sobel. Mechanisms of scent-tracking in humans. *Nat. Neurosci.*, 10(1):27–29, Jan 2007.

[79] D. Premack and M. E. Shanab. Rats prefer the home cage to the runway following intermittent but not consistent reinforcement. *Nature*, 217(5125):288–289, Jan 1968.

[80] T. J. Prescott, M. E. Diamond, and A. M. Wing. Active touch sensing. *Philos. Trans. R. Soc. Lond., B, Biol. Sci.*, 366(1581):2989–2995, Nov 2011.

[81] R. Rajan, J. P. Clement, and U. S. Bhalla. Rats smell in stereo. *Science*, 311(5761):666–670, Feb 2006.

[82] S. Ranade, B. Hangya, and A. Kepecs. Multiple modes of phase locking between sniffing and whisking during active exploration. *J. Neurosci.*, 33(19):8250–8256, May 2013.

[83] R. N. Sachdev, R. W. Berg, G. Champney, D. Kleinfeld, and F. F. Ebner. Unilateral vibrissa contact: changes in amplitude but not timing of rhythmic whisking. *Somatosens Mot Res*, 20(2):163–169, 2003.

[84] C. E. Schroeder, D. A. Wilson, T. Radman, H. Scharfman, and P. Lakatos. Dynamics of Active Sensing and perceptual selection. *Curr. Opin. Neurobiol.*, 20(2):172–176, Apr 2010.

[85] K. Semba and B. R. Komisaruk. Neural substrates of two different rhythmical vibrissal movements in the rat. *Neuroscience*, 12(3):761–774, Jul 1984.

[86] R. Shusterman, M. C. Smear, A. A. Koulakov, and D. Rinberg. Precise olfactory responses tile the sniff cycle. *Nat. Neurosci.*, 14(8):1039–1044, Jul 2011.

[87] Y. B. Sirotin, M. E. Costa, and D. A. Laplagne. Rodent ultrasonic vocalizations are bound to active sniffing behavior. *Front Behav Neurosci*, 8:399, 2014.

[88] M. Smear, R. Shusterman, R. O'Connor, T. Bozza, and D. Rinberg. Perception of sniff phase in mouse olfaction. *Nature*, 479(7373):397–400, Oct 2011.

[89] J. C. Smith, A. P. Abdala, A. Borgmann, I. A. Rybak, and J. F. Paton. Brainstem respiratory networks: building blocks and microcircuits. *Trends Neurosci.*, 36(3):152–162, Mar 2013.

[90] N. J. Sofroniew, J. D. Cohen, A. K. Lee, and K. Svoboda. Natural whisker-guided behavior by head-fixed mice in tactile virtual reality. *J. Neurosci.*, 34(29):9537–9550, Jul 2014.

[91] V. Sreenivasan, K. Karmakar, F. M. Rijli, and C. C. Petersen. Parallel pathways from motor and somatosensory cortex for controlling whisker movements in mice. *Eur. J. Neurosci.*, 41(3):354–367, Feb 2015.

[92] E. Stanek, S. Cheng, J. Takatoh, B. X. Han, and F. Wang. Monosynaptic premotor circuit tracing reveals neural substrates for oro-motor coordination. *Elife*, 3:e02511, Apr 2014.

[93] K. Steck, B. S. Hansson, and M. Knaden. Smells like home: Desert ants, Cataglyphis fortis, use olfactory landmarks to pinpoint the nest. *Front. Zool.*, 6:5, Feb 2009.

[94] R. L. Stornetta, D. L. Rosin, H. Wang, C. P. Sevigny, M. C. Weston, and P. G. Guyenet. A group of glutamatergic interneurons expressing high levels of both neurokinin-1 receptors and somatostatin identifies the region of the pre-Bötzinger complex. *J. Comp. Neurol.*, 455(4):499–512, Jan 2003.

[95] H. Suzuki. Antennal movements induced by odour and central projection of the antennal neurones in the honey-bee. *Journal of Insect Physiology*, 21(4):831–847, 1975.

[96] M. Szwed, K. Bagdasarian, B. Blumenfeld, O. Barak, D. Derdikman, and E. Ahissar. Responses of trigeminal ganglion neurons to the radial distance of contact during active vibrissal touch. *J. Neurophysiol.*, 95(2):791–802, Feb 2006.

[97] J. Takatoh, A. Nelson, X. Zhou, M. M. Bolton, M. D. Ehlers, B. R. Arenkiel, R. Mooney, and F. Wang. New modules are added to vibrissal premotor circuitry with the emergence of exploratory whisking. *Neuron*, 77(2):346–360, Jan 2013.

[98] W. Tan, W. A. Janczewski, P. Yang, X. M. Shao, E. M. Callaway, and J. L. Feldman. Silencing preBötzinger complex somatostatin-expressing neurons induces persistent apnea in awake rat. *Nat. Neurosci.*, 11(5):538–540, May 2008.

[99] W. Tan, S. Pagliardini, P. Yang, W. A. Janczewski, and J. L. Feldman. Projections of preBötzinger complex neurons in adult rats. *J. Comp. Neurol.*, 518(10):1862–1878, May 2010.

[100] N. Tinbergen. *The Study of Instinct*. New York: Oxford University Press, 1951.

[101] R. B. Towal and M. J. Hartmann. Right-left asymmetries in the whisking behavior of rats anticipate head movements. *J. Neurosci.*, 26(34):8838–8846, Aug 2006.

[102] N. Uchida and Z. F. Mainen. Speed and accuracy of olfactory discrimination in the rat. *Nat. Neurosci.*, 6(11):1224–1229, Nov 2003.

[103] M. Wachowiak. All in a sniff: olfaction as a model for active sensing. *Neuron*, 71(6):962–973, Sep 2011.

[104] C. R. Watson, S. Sakai, and W. Armstrong. Organization of the facial nucleus in the rat. *Brain Behav. Evol.*, 20(1-2):19–28, 1982.

[105] George Paxinos Charles Watson. *The Rat Brain in Stereotaxic Coordinates 7 th Edition*. Academic Press, 2013.

[106] W.I. Welker. Analysis of sniffing of the albino rat. *Behaviour*, 12:223Ű244, 1964.

[107] D. A. Wilson and R. M. Sullivan. Respiratory airflow pattern at the rat's snout and an hypothesis regarding its role in olfaction. *Physiol. Behav.*, 66(1):41–44, Mar 1999.

[108] J. Wolfe, C. Mende, and M. Brecht. Social facial touch in rats. *Behav. Neurosci.*, 125(6):900–910, Dec 2011.

[109] D. M. Wolpert. Computational approaches to motor control. *Trends Cogn. Sci. (Regul. Ed.)*, 1(6):209–216, Sep 1997.

[110] Y. S. Yu, M. M. Graff, C. S. Bresee, Y. B. Man, and M. J. Hartmann. Whiskers aid anemotaxis in rats. *Sci Adv*, 2(8):e1600716, 08 2016.

[111] E. Zucker and W. I. Welker. Coding of somatic sensory input by vibrissae neurons in the rat's trigeminal ganglion. *Brain Res.*, 12(1):138–156, Jan 1969.